Seismic Analysis of Spatio-Temporal Fracture Generation During EGS Resource Development

Final Report

Performance Period: October 1, 2014 through June 30, 2018

Sponsored by
Golden Field Office
U.S. Department of Energy
1617 Cole Blvd.
Golden, CO 80401

Award No. DE-EE0006766

Principal Investigator:

Dr. Roland Gritto
Roland.Gritto@arrayinfotech.com
Array Information Technology
Advanced Technology Division
2020 Cedar Street
Berkeley, California 94709

Co-Principal Investigator:

Prof. Douglas Dreger
Berkeley Seismological Laboratory
University of California, Berkeley
Berkeley, California 94720-4760

Table of Contents

I. Executive Summary

1.0 Acknowledgment

This material is based upon work supported by the Department of Energy's Office of Energy Efficiency and Renewable Energy (EERE) under Geothermal Technologies Office (GTO) under Award Number DE-EE0006766.

Seismic data for this study came from the Berkeley Geysers Seismic Network (BG), operated by Lawrence Berkeley National Laboratory with financial support from U.S. DOE Office of Geothermal Technology, and from the Berkeley Digital Seismic Network (BDSN), doi:10.7932/BDSN, operated by the UC Berkeley Seismological Laboratory, which are archived at the Northern California Earthquake Data Center (NCEDC), doi:10.7932/NCEDC.

Special thanks are extended to Calpine Corp., especially Craig Hartline and Julio Garcia, for their assistance, fruitful discussions and supplemental data to support the research and interpretation of results.

Monthly injection data were acquired from the Online Geothermal Well Data Query for State of California, Department of Conservation, Division of Oil, Gas, and Geothermal Resources.

Maps and graphics were produced using the Generic Mapping Tools version 4.5.9 (www.soest.hawaii.edu/gmt:Wessel&Smith 1998).

2.0 Disclaimer

3.0 Objectives

This DOE GTO funded project was a collaborative effort between Array Information Technology (AIT) and the University of California at Berkeley (UCB). The project goal is to improve technology to assess in-situ stress magnitude and orientation, kinematic fracture parameters, rupture size, rupture orientation as well as temporal changes and volumetric distribution of the injected fluid during Enhanced Geothermal System (EGS) resource development. The project leveraged high-frequency seismic data recorded by the LBNL 34-station permanent geophone network and seismic broadband data recorded by a temporary 33-station seismometer network that operated in The Geysers during the injection phase of the DOE GTO funded EGS demonstration project at the well Prati-32. The operation of the broadband network with high station density and good azimuthal coverage to monitor the injection phase produced an unprecedented dataset that is typically unavailable for EGS operations. The two datasets offer the advantages of studying the parameters under investigation over a broader frequency band and the higher sensitivity of the broadband seismometers resulted in a richer dataset with a lower magnitude of completeness. Moment tensor inversion will be employed to develop a catalog of earthquake source solutions including moment tensor and finite source rupture area. These parameters will be utilized to develop a scaling relationship between moment magnitude and source rupture area. The results from the moment tensor catalog will form the basis for stress analyses prior to and during injection activities to estimate stress orientation and stress changes during EGS operations. The above results will be subsequently combined to generate an empirical fracture network with fracture locations, fracture area and fracture orientation. The double-difference Wadati (DDW) technique will be applied to high-accuracy P- and S-wave differential travel times derived from waveform cross correlation to image fluid saturation in the subsurface based on Vp/Vs-ratio. The recently developed technique has been applied to estimate temporal changes of fluid distribution in fault zones and in volcanic regions but not yet in engineered geo-reservoirs. If successful, the improvement in the present study will allow to estimate both, the spatial and temporal distribution of injected fluids and the state of the injected fluid during reservoir stimulation. The improvement of the technology includes high-resolution waveform cross correlation applied to the high-quality datasets with lower magnitude of completeness resulting in a higher number of recorded events. The high number of events will allow estimation of the spatial distribution of the injected fluid in addition to the traditional temporal distribution.

4.0 Summary

4.1 Temporal Analysis of Fluid Injection

During this project, for the first time, the DDW technique is applied to a geothermal EGS system. The high-frequency seismic data were collected by the 34-station LBNL geophone network. The DDW technique is based on high-accuracy P- and S-wave differential travel times

derived from subsample waveform cross correlation to image fluid saturation in the subsurface based on Vp/Vs-ratio. The formalism of the DDW technique is presented coupled with the implementation of the L1-L2 norm fitting. L1-L2 norm fitting is required due to the specific nature of seismic travel time data, which contain statistical uncertainties and outliers in both, P- and S-wave, travel times. Application of the DDW technique to the fumarole steam field in The Geysers revealed low Vp/Vs ratios indicative of the presence of gaseous liquids in the subsurface. These values matched results obtained from 3D velocity inversions by Gritto et al. (2013) for the same area. The application of the DDW technique to the Prati-32 EGS demonstration site in the high-temperature reservoir in the northwest Geysers indicated the development of a steam plume during the first three months of water injection.

4.2 Source Parameter Determination

A semi-automated moment tensor (MT) technique has been developed to appraise deviatoric and full moment tensor solutions (DMT and FMT) for seismicity in the Prati-32 study area. This led to the developments of two MT catalogs (DMT and FMT) with 167 source mechanisms each, which spanned a magnitude range from $0.6 \leq M \leq 3.9$. The results from the moment tensor analysis indicate that seismicity in the vicinity of the Prati-32 study area evolves in space and time as water injection operations progress. Most of the events are likely the result of shear failure due to both tectonic shear stress and tensile stress induced by the injection of water. Even though the moment tensor catalogs are limited to 167 events, patterns in earthquake source parameters emerge before and during multiple stages of injection and shut-in. Moment tensors of pre-injection events have a greater per cent double couple (DC). Larger magnitude events are more frequent during periods of injection. Strike-slip events are most common prior to and during the initial injection phase with a gradual transition to more normal faulting mechanisms as injection progresses.

4.3 Seismic Broadband Data Processing

This task has generated, for the first time, a seismic catalog from continuously recorded local broadband data at The Geysers geothermal reservoir. These data were collected with financial support from the European GEISER project and have been leveraged for the current DOE project. The results include a catalog of seismic events recorded from July 2012 to July 2013 during the Prati-32 EGS project. The data include event origin time, event location and event depth, P- and S-wave phase arrivals and moment magnitudes. The DDW technique has also been applied to the broadband seismic data to corroborate the findings of the analysis of high frequency geophone data.

4.4 Scaling Relationship for Prat32 Seismicity and 3D Fracture Network

The results of finite source inversions of Prati-32 and surrounding seismicity are utilized to derive a magnitude scaling relationship for The Geysers geothermal reservoir. It was found that the magnitude scaling relationship for The Geysers is consistent with the scaling laws of both

Wells and Coppersmith (1994) and Leonard (2010). This is remarkable as those relationships were developed for events with moment magnitudes (Mw) larger than 5.5, and the great majority of events in those studies are for earthquakes larger than Mw 6.0 observed in other regions of the world. This new scaling relationship is subsequently applied to the moment magnitudes reported in the DOE EGS LBNL catalog to estimate frature area for all events in the Prati-32 study region. The fracture areas combined with the hypocenter locations of the seismicity and the in-situ stress results from section 8 are subsequently combined to generate a semi-empirical 3D fracture network. The spatial distribution of the fracture network reveals that the highest concentration of fractures is located approximately 300 m to the north and 400 m below the bottom of the injection and production wells.

4.5 Aleatory and Epistemic Uncertainty of the Double-Difference Wadati Method

A statistical analysis of aleatory and epistemic uncertainty related to the application of DDW to the seismicity recorded by the geophone- and broadband sensor networks at the Prati-32 injection demonstration project is conducted. It is found that the Vp/Vs-ratio in the two years prior to injection was close to that for typical crustal rocks, which was interpreted to indicate that the reservoir rocks in the study area are undisturbed due to the absence of injection and production activities. A drop of Vp/Vs in the three months after the start of injection indicated the development of a steam plume below the injection point of Prati-32. This is in agreement with the assumption of water flashing to steam upon contact with the rock in this high temperature reservoir. The analysis of broadband data, recorded nine months after the start of injection and for the duration of one year, indicates that the steam plume is still present in the system. Analyses of aleatory and epistemic uncertainty of the geophone- and broadband seismic networks indicated that the Vp/Vs estimates are stable with respect to randomness and lack of knowledge in the system.

4.6 Spatial Analysis of Fluid Injection

A semi-empirical representation of the 3D fracture network was generated during the EGS demonstration project at Prati-32. It is found that that the highest concentration of fractures is located approximately 300 m to the north and 400 m below the bottom of the injection and production wells. Given the uneven distribution of fractures in the study area, DDW was applied to investigate spatial variations in the fluid saturations. Our previous results indicated already that during the first three months of injection a steam plume developed in the study region below Prati-32. The current analysis revealed that the steam plume is not symmetrically distributed within the 1x2 km Prati-32 study area but appears to be more concentrated in the northern half of the study area, which spatially agrees with the location of the high fracture concentration. The analyses show that DDW can be applied to EGS systems to estimate spatio-temporal changes in subsurface fluid saturation during all phases of EGS operations to aid in the assessment of the fluid content in the subsurface.

4.7 In-Situ Stress Estimation

The goal of EGS hydraulic stimulations is to artificially induce shear slip and dilatation along pre-existing fractures by injecting fluids at low pressures to enhance formation permeability in hot but impermeable rocks. For these stimulations to be successful, the targeted formations should contain slightly permeable natural fractures that are well oriented and highly stressed for shear failure and have the appropriate mechanical properties for the generation and maintenance of shear-enhanced fracture dilatation (Hickmann and Davatzes, 2010). Therefore, the characterization of fracturing and the orientation of principal stresses and changes in stress orientation are critical factors for the planning and the development of EGS resources and for the operations of EGS systems. A catalog of 167 waveform-based seismic moment tensor solutions ranging in moment magnitude from 0.6 to 3.9 is used to invert for the stress tensor and to investigate possible temporal stress changes resulting from fluid injection. An approximate 15-degree counter-clockwise rotation of the least compressive stress σ_3 during injection is found. More remarkable is a change in orientation of the maximum compressive stress σ_1 from subhorizontal to vertical when injection operations temporarily cease. The orientation of σ_1 returns to subhorizontal when injection operations resume. It is found that there was a systematic reduction in the stress shape factor, R, as the injected water volume increases, indicating an evolution towards a more transtensional stress state.

5.0 Challenges

The double-difference Wadati method depends on a sufficient number of seismic stations with good spatial aperture to satisfy the underlying assumptions. However, The Geysers are perfectly suited for the appraisal and statistical uncertainty analysis of DDW and its application to EGS development, due to the high number of seismic stations in the LBNL network and the high seismicity rate encountered in the reservoir.

A challenge to moment tensor analysis of seismic events during EGS activities is the low magnitudes of the earthquakes requiring the simultaneous use of multiple data types to constrain the seismic moment tensor. We have developed a method that enables the simultaneous inversion of seismic waveforms and P-wave first-motion polarities in the Hudson et al. (1989) or Tape and Tape (2014) source-type space (e.g., Nayak and Dreger, 2014, 2015) that finds not only the best fitting mechanism, but also characterizes the nature of possible non-double-couple seismic radiation and its uncertainty. With this technique, we were able to lower the magnitude for full waveform MT inversion to Mw 0.6.

The development of a scaling relationship, based on finite source inversion, is challenging in that pairs of earthquakes with a difference in magnitude of one unit are located sufficiently close together. Furthermore, to obtain a reliable linear fit to the magnitude-versus-fracture-area relationship the analyzed events need to cover a sufficiently wide magnitude range of three to four units. Again, thanks to the high seismicity rate at The Geysers and the high number of seismic stations in the LBNL network, it was possible to derive such relationship for The

Geysers and show that is consistent with published scaling relationships derived with earthquakes observed in other regions of the world.

Despite these challenges, all goals and objective, as defined in the statement of project objective, have been accomplished.

6.0 Relevance to Public

The current project is beneficial to the public in that the findings improve the understanding of the physical processes in the reservoir during the development and operation of an EGS system. Knowledge of the stress tensor and temporal stress changes help to optimize the generation of a fracture system and to sustain production during operations. The ability to generate images of the 3D fracture network, including fracture orientation and activated fracture area, in conjunction with knowledge of the state of injectate (liquid or gaseous) enables the operator to target specific zones to improve production and to extend the longevity of the EGS system. In the case of the Prati-32 EGS system, this information is directly beneficial to Calpine, which can use the reported findings to optimize production at the site.

The Geysers represents a unique field scale laboratory with unparalleled seismicity rates that offer the opportunity to develop state-of-the-art seismic techniques to estimate relevant subsurface parameters for the operation of geothermal reservoirs and the development and operations of EGS systems. Therefore, data collection projects, such as the DOE funded 34-station geophone network, which is operated by the Lawrence Berkeley National Laboratory (LBNL), need to be continued.

It was demonstrated that the technology developed during this project can successfully be used to evaluate an EGS reservoir prior to and during operations. Furthermore, the tools developed and evaluated under the current project are easily portable and can be applied to study EGS systems in other geothermal settings. This would extend the knowledge gained at the Prati-32 EGS site to other geothermal systems to improve and optimize those operations.

The requirements for the developed techniques to be successfully applied to other geothermal sites include the presence of seismicity and the availability of a seismic network with sufficient aperture. The Double Difference Wadati method relies on a seismic network with a maximum station gap between 130^{o} and 150^{o} relative to the centroid of the seismicity under investigation. Considering that EGS-induced micro seismicity typically has low magnitudes, such that events are likely not recorded on all stations, the station gap can quickly grow beyond the limits of DDW if the seismic network contains too few stations resulting in large azimuthal gaps. Therefore, azimuthal gaps between seismic stations relative to the centroid of the seismicity cloud should not exceed 45^{o}.

The availability of seismic borehole stations improves the depth accuracy of the earthquake hypocenters and lower the detection threshold of the seismic network. These

borehole stations should not be deployed shallower than 15-20 % of the target depth to provide enough vertical offset relative to the surface network to improve hypocenter depth estimation.

If, sufficient background seismicity is recorded in the region of interest, temporal changes of reservoir properties before and after the start of injection can be investigated. However, if the region of interest is relatively aseismic, temporal changes will only be observable after the start of injection when sufficient induced micro-seismicity has been recorded.

In the case of The Geysers, the lowest number of earthquakes the DDW method was applied to was ~ 100. In this case the events were recorded by 15 seismic stations, which allowed for a sufficient number of co-located event pairs with similar waveforms to be found.

The stress analysis is based on software that requires a minimum of 20 events per each time-window for which the stress orientation is estimated. Successive time windows are subsequently investigated to estimate temporal changes in stress orientation. However, the time windows are partially overlapping and share seismic events to provide smoother estimates of stress changes.

The scaling relationship established for The Geysers is based on published results ($M \geq 5.5$) and extended to lower magnitudes estimating the rupture area for nine events ($2.1 \geq M \geq 5$). However, the finite source estimation, which is the basis for the scaling relationship, requires nine co-located events (relative to the analyzed nine evnts) with magnitudes that are at least one magnitude unit smaller than the nine main events.

Once the scaling relationship and the stress orientations are established, representative fracture parameters such as fracture location, activated fracture area, fracture azimuth and fracture dip can be determined for single events.

7.0 Products Developed Under Award

7.1 Publications, Conference Papers and Presentations

Boyd, O. S., D. S. Dreger, V. H. Lai, and R. Gritto, 2015, A Systematic Analysis of Seismic Moment Tensor at The Geysers Geothermal Field, California, *Bull. Seism. Soc. Am.*, 105, No. 6, doi:10.1785/0120140285.

Boyd, O. S., D. S. Dreger and R. Gritto, 2015, Analysis of seismic moment tensor and finite-source scaling during the EGS resource development at the Geysers, CA, S13B-2805, *Annual Meeting of the American Geophysical Union*.

Boyd, O. S., D. S. Dreger and R. Gritto, 2016, Analysis of Seismic Moment Tensor During EGS Development at The Geysers Geothermal Field, California, S13B-2805, *Annual Meeting of the American Geophysical Union*.

Boyd, O.S., D. S. Dreger, and R. Gritto, 2017, Analysis of in-situ stress during EGS development at the Geysers Geothermal Field, California, Annual Meeting of the Seismological Society of America, *Seism. Res. Lett.*, vol. 88 (2B), 533.

Boyd, O.S., D.S. Dreger, T. Taira, and R. Gritto, 2017, Magnitude and Rupture Area Scaling Relations of Seismicity at the NW Geysers EGS Demonstration Project, *American Geophysical Union 2017 Annual Meeting*, New Orleans, LA.

Boyd, O.S., D.S. Dreger, R. Gritto, and J. Garcia, 2018, Analysis of seismic moment tensors and in-situ stress during Enhanced Geothermal System development at The Geysers geothermal field, California, *Geophys. J. Int.*, 215, 1483–1500, doi: 10.1093/gji/ggy326.

Dreger, D.S., R. Gritto, and O.S. Boyd, 2015, Analysis of Seismic Moment Tensor, Finite-Source Scaling and Fluid Imaging During EGS Resource Development at The Geysers, CA, *GRC Transactions,* Vol.39, pp. 279-284.

Dreger, D.S., R. Gritto, and O.S. Boyd, 2017, Automatic Moment Tensor Analyses, In-Situ Stress Estimation and Temporal Stress Changes at The Geysers EGS Demonstration Project, *Proceedings, 42nd Workshop on Geothermal Reservoir Engineering*, Stanford University, Stanford, California, February 13-15, 2017, SGP-TR-212, pp. 1-10.

Dreger, D.S., R. Gritto, and O.S. Boyd, 2017, Estimating In-Situ Stress, Fracture Properties and Fluid Saturation During The Geysers EGS Demonstration Project, *GRC Transactions*, Vol.41, pp. 1-16.

Dreger, D.S., R. Gritto, O.S. Boyd, and T. Taira, 2018, Seismic Analysis of Spatio-Temporal Fracture Generation at The Geysers EGS Demonstration Project, *Proceedings, 43rd Workshop on Geothermal Reservoir Engineering*, Stanford University, Stanford, California, February 12-15, 2018, SGP-TR-213, pp. 1-13.

Dreger, D. S., O. S. Boyd, T. Taira, and R. Gritto, 2018, Stress Drop and Scaling of Earthquakes at the Geysers Geothermal Field California, Annual Meeting of the Seismological Society of America, *Seism. Res. Let.*, Vol. 89, Num. 2b, page 771.

Gritto R., D.S. Dreger, and O.S. Boyd, 2015, Seismic Analysis of Spatio-Temporal Fracture Generation During EGS Resource Development, *DOE GTP Peer Review Meeting*, 11-14 May, 2015, Denver, CO.

Gritto, R., D.S. Dreger, O.S. Boyd, and T. Taira, 2016, Fluid Imaging, Moment Tensors and Finite Source Models During the EGS Demonstration Project at The Geysers, CA, *Proceedings, Stanford Geothermal Workshop,* 2016 Stanford University.

Gritto R., D.S. Dreger, and O.S. Boyd, 2017, Seismic Analysis of Spatio-Temporal Fracture Generation During EGS Resource Development, *DOE GTP Peer Review Meeting*, 13-15 November, 2017, Denver, CO.

Nayak, A., T. Taira, D.S. Dreger, and R. Gritto, 2017, Empirical Green's tensor retrieved from ambient noise cross-correlations at The Geysers geothermal field, Northern California, *Geophys. J. Int.*, doi: 10.1093/gji/ggx534.

7.2 Special Sessions on Induced Seismicity at Professional Meetings

Special sessions on induced seismicity with varying topics were organized and convened at the AGU Annual Meetings 2014, 2015, 2016, 2017 and at the EGU Annual Meetings 2014, 2015, 2016, 2017 and 2018.

7.3 Catalogs and Models

A moment tensor catalog was developed for 167 studied earthquakes from the area surrounding the Prati-32 EGS demonstration project. Deviatoric and full moment tensor solutions are presented in the final technical report and the associated catalogs are publicly available via the Geothermal Data Repository (GDR/NGDS https://gdr.openei.org). The catalogs are also publicly available via the Northern California Earthquake Data Center (ftp://ncedc.org/outgoing/dreger/Boyd_etal_2018_SupplementaryTableS1.csv).

Spatio-temporal analyses of the injected fluid has been conducted and temporal as well as spatial variations have been presented in the final report, at Stanford Geothermal Workshops (2016, 2018) and at Geothermal Resources Council Annual Meetings (2015, 2017).

An earthquake catalog was developed using seismic broadband recorded from July 2012 to July 2013. The catalog comprises event hypocenter locations, event origin times, event magnitudes, P- and S-wave phase picks and 17 s waveforms for each event around the P- and S-phase picks. The results are presented in the final technical report and the associated catalog is publicly available via the Northern California Earthquake Data Center (http://ncedc.org/ftp/pub/assembled/geysersBB). Furthermore, the continuous broadband data records for all 33 recording stations are also publicly available via the Northern California Earthquake Data Center (http://ncedc.org/ftp/pub/assembled/geysersBB).

The stress inversion of the 167 studied events yielded stress orientation for azimuth and plunge angles for the three main stress directions σ_1, σ_2 and σ_3 at the Prati32 EGS demonstration site. The data are divided into 15 time periods spanning a range of five years, including two years prior to start of injection until three years post start of injection activities. These data are presented in the final report and are publicly available via the Geothermal Data Repository (GDR/NGDS https://gdr.openei.org). The results are also publicly available via the Northern California Earthquake Data Center (ftp://ncedc.org/outgoing/dreger/Boyd_etal_2018_SupplementaryTableS1.csv).

A magnitude vs. fracture area scaling relationship was developed for The Geysers geothermal reservoir. It was found that the scaling relationship followed the one published by Leonard (2010). The scaling relationship has been presented in the final report, at the Stanford Geothermal Workshop (Dreger et al., 2018) and at the Geothermal Resources Council Annual Meetings (Dreger et al., 2017). It is also published in Leonard, M., 2010, Earthquake Fault Scaling: Self-Consistent Relating of Rupture Length, Width, Average, Displacement, and Moment Release, *Bull. Seism. Soc. Am.*, doi: 10.1785/0120090189, 1971-1988.

A semi-empirical 3D fracture network was generated from the seismicity recorded by the LBNL Berkeley Geysers Seismic Network, the results of the stress analysis, and the magnitude-fracture area scaling relationship. The network is comprised of single fractures including fracture location, fracture area, fracture strike and fracture dip direction. The results have been presented in the final report and are publicly available via the Geothermal Data Repository (GDR/NGDS https://gdr.openei.org). The results are also publicly available via the Northern California Earthquake Data Center (ftp://ncedc.org/outgoing/dreger/Boyd_etal_2018_SupplementaryTableS1.csv).

7.4 Networks or Collaborations Fostered

This project was a collaborative effort between Array Information Technology and the University of California at Berkeley. The collaboration was complemented by Calpine Corp., which provided supplemental data and fruitful discussions to support the research and to help with interpretation of results. This collaboration was formed to take advantage of the specialization in each group to generate a strong research team capable of addressing some of the barriers that are still limiting the development of successful and sustainable EGS systems.

7.5 Technologies and Approaches

For the first time, the double difference Wadati method was applied to seismic data recorded at an EGS demonstration site. The result was an estimation of the aggregate state of the injected water (liquid or gaseous) as well as the spatial distribution and temporal variations of injected liquid into the high-temperature reservoir. The uncertainty of the DDW technique was also investigated with the results that it can generate statistically significant results, if the number of seismic events and the network coverage is sufficient, and the station gap is not greater than 150 degrees. The DDW should be a viable tool to assess the spatio-temporal variations of injected fluids in geothermal reservoirs. The results of the tomographic imaging are provided in the final technical report, in two Stanford Geothermal Workshop papers (Gritto et al., 2016; Dreger et al., 2018) and in two papers presented at Geothermal Resources Council Annual Meetings (Dreger et al., 2015; Dreger et al., 2017).

A recently developed moment tensor inversion technique was successfully extended and applied to seismic waveform data recoded by the LBNL geophone network at The Geysers geothermal reservoir. During our study, it was possible to lower the magnitude of the smallest analyzed earthquake to Mw = 0.6, which is remarkable considering the high level of cultural noise from reservoir operations at The Geysers. The applied moment tensor technique solves for the simultaneous inversion of seismic waveforms and P-wave first-motion polarities, which finds not only the best fitting mechanism, but also characterizes the nature of possible non-double-couple seismic radiation and its uncertainty. After the successful application to micro-earthquake waveform at the Prati-32 EGS demonstration site, this technology is ready to be applied to other EGS site where micro-seismicity is recorded by seismic networks. The results of the moment tensor inversions are provided in the final technical report, in two published journal articles (Boyd et al., 2015; Boyd et al., 2018), in three Stanford Geothermal Workshop papers (Gritto et al., 2016; Dreger et al., 2017; Dreger et al., 2018), in two papers presented at Geothermal Resources Council Annual Meetings (Dreger et al., 2015; Dreger et al., 2017), at three conferences of the American Geophysical Union (Boyd et al., 2015; Boyd et al., 2016; Boyd et al., 2016), at two conferences of the Seismological Society of America (Boyd et al. 2016,; Dreger et al., 2018) and at two DOE review meetings (Gritto et al., 2015; Gritto et al., 2017).

A magnitude versus fracture area scaling relationship was developed for The Geysers geothermal area. It was found that the relationship indicates self-similarity of earthquake scaling, which was not known for The Geysers prior to this project. It was also found that the scaling relationship matches that published by Leonard (2010), which is remarkable, since the latter was developed for much larger earthquakes in different region of the world. The established scaling relationship can be used in future studies to extract finite source parameters from the already established seismic catalogs. The results of the scaling relationship are provided in the final technical report and have been presented at the Stanford Geothermal Workshop 2018 (Dreger et al., 2018) and at the Geothermal Resources Council Annual Meetings 2017 (Dreger et al., 2017).

A recently developed technique STRESSINVERSE (Vavrycuk, 2014) was used to invert source mechanisms from moment tensor inversions to estimate the in-situ state of stress. The technique was applied to the strike, rake and dip from 167 solutions in our moment tensor catalog that was developed for the Prati-32 EGS demonstration site. The technique has been applied in different geothermal and tectonic regions and can be easily transferred to other EGS systems, where micro-seismicity is recorded by seismic networks.

7.6 Computer Modeling Codes, Theory and References

The moment tensor analysis conducted in current project is based on the full moment tensor model described in Minson and Dreger (2008). The software including source, examples and tutorial can be obtained from ftp://ncedc.org/outgoing/dreger/ pasi-nov282012.tar.gz. Performance criteria, mathematics and test results are provided by Minson and Dreger (2008) and Ford et al. (2008, 2009, 2010, 2012).

The model is a full moment tensor that describes the strength of force couples that can be combined to describe tectonic earthquakes (double-couple), explosions, and mining collapses, and combinations of shear and tensile force systems such as an inflating tensile crack. The method assumes that adequate descriptions of seismic wave propagation may be modeled in one-dimension at long period. Synthetic seismograms for the fundamental source types (force couples) are fit to observed long-period seismograms to determine the type and orientation of the mechanisms of seismic radiation.

The moment tensor analysis code runs on computer operating systems including Unix, Linux and Mac OSX.

The computer code STRESSINVERSE (Vavrycuk, 2014) was used to invert for the in-situ state of stress within the study region. The STRESSINVERSE code uses an iterative method to find the nodal planes most consistent with the stress field given fault frictional properties. STRESINVERSE inverts the strike, rake and dip from moment tensor solutions for the in-situ state of stress. The code iteratively solves for an optimal friction parameter in evaluating the fault instability to find optimal fault planes. Vavrycuk (2014) states that numerical tests show that inversion results are insensitive to the friction parameter, and it is sufficient to assign a reasonable value for all inversions. In this project, we elected to allow the friction parameter to change and found it to not substantially change with values of 0.7 ± 0.2, which is consistent with laboratory estimates for graywacke and other rocks at the confining pressures of the studied earthquakes (i.e., Byerlee 1978; Lockner *et al.* 1982). The software including source, examples and tutorial can be obtained from https://www.ig.cas.cz/en/stress-inverse.

The underlying development including theory, performance criteria, and test results for the software packages listed above are also provided in the following references.

Ford, S., D. Dreger and W. Walter (2008). Source Characterization of the August 6, 2007 Crandall Canyon Mine Seismic Event in Central Utah, *Seism. Res. Lett*., 79, 637-644.

Ford, S. R., D. S. Dreger and W. R. Walter (2009). Identifying isotropic events using a regional moment tensor inversion, *J. Geophys. Res*., 114, B01306, doi:10.1029/2008JB005743.

Ford, S. R., D. S. Dreger and W. R. Walter (2010). Network sensitivity solutions for regional moment tensor inversions, *Bull. Seism. Soc. Am*., 100, p. 1962-1970.

Ford, S. R., W. R. Walter, and D. S. Dreger (2012). Event discrimination using regional moment 665 tensors with teleseismic-P constraints, *Bull. Seism. Soc. Am*. 102**,** 867-872.

Minson, S. and D. Dreger (2008), Stable Inversions for Complete Moment Tensors, *Geophys. J. Int.*, 174, 585-592.

Saikia, C.K. (1994), Modified Frequency-Wavenumber Algorithm for Regional Seismograms using Filon's Quadrature: Modeling of Lg Waves in Eastern North America. *Geophys. J. Int.*, 118, 142-158.

Vavrycuk, V., 2014. Iterative joint inversion for stress and fault orientations from focal mechanisms, *Geophys. J. Int.*, 199, 69–77.

II. Technical Report

1.0 Introduction

Identifying, creating, and managing fractures and flow paths are essential tasks during EGS resource development. The successful generation of a fracture network requires a priori knowledge of in-situ stress and natural fracture orientation, fracture area and fracture spacing, among others. However, because the orientation and magnitude of in-situ stress may not be reliably available and injecting fluids at high rates and volume may disturb the natural stress state, it is advantageous to monitor in-situ stress during the injection process. Knowing the stress evolution, the location, the orientation and activated area of the fracture network, the speed of the rupture process, as well as the spatial and temporal distribution of the fluids are essential to control the generation of the fracture network. In the following, we will report on the development of an integrated technology approach to estimate the in-situ stress, stress changes, the size and orientation of the activated fracture network, and the spatial and temporal fluid distribution during reservoir stimulation at The Geysers Prati-32 EGS demonstration project. The Prati-32 injection site is in the Northwest Geysers geothermal field, within the felsite, where reservoir conditions indicate non-hydrothermal hot dry rock and temperatures rise to 400 ^{o}C (Lutz et al. 2012). The EGS demonstration area is 1×2 km and roughly centered on the EGS wells Prati-32 (injection well) and Prati 31 (production well) as shown in Figure 1.1. The EGS wells encounter the high temperature reservoir (HTR) from 3.0 to 3.5 km depth with a separation distance of 0.5 km (Garcia et al. 2012). Six Quaternary surface shear zones (Mercuryville, Alder Creek, Squaw Creek, Ridgeline, Caldwell Pines and Caldwell Ranch, Figure 1.1), have been identified and may possibly extend to depths of the HTR creating barriers to flow in adjacent regions of the reservoir (Garcia et al. 2016). One of these shear zones, known as the Caldwell Pines Fault, trends northeast (Nielson et al. 1991) and extends from the surface to the reservoir and may form a hydraulic discontinuity between the EGS wells Prati 31 and Prati-32 and those to the southeast of the Caldwell Ranch Project such as Prati 38 (Garcia et al. 2016). Interestingly, our analysis includes fewer and larger events south of the Caldwell Pines Fault as injection progresses (Boyd et al., 2018).

Comparing the monthly averaged injection rate (blue line) with monthly averaged seismicity (red asterisks) from the Northern California Earthquake Data Center, Enhanced Geothermal System (NCEDC EGS) catalog in Figure 1.2 reveals a strong correlation coefficient of 0.77 (R^2 = 0.59) and from the p-value (3.2e-16) the correlation is significantly different than zero. The low pre-injection rate of seismicity markedly increases with the initiation of injection. Later, as the injection rate stabilizes, the rate of earthquakes is seen to reach a steady level as well. In fact, short-term fluctuations in the injection rate seem to also be marked by short-term fluctuations in the rate of earthquakes (Boyd et al., 2018). Statistical tests performed between seismicity and injection rate in two nearby wells finding strong correlation in which changes in the seismicity rate lag changes in the injection rate by approximately two weeks (Leptokaropoulos et al., 2018).

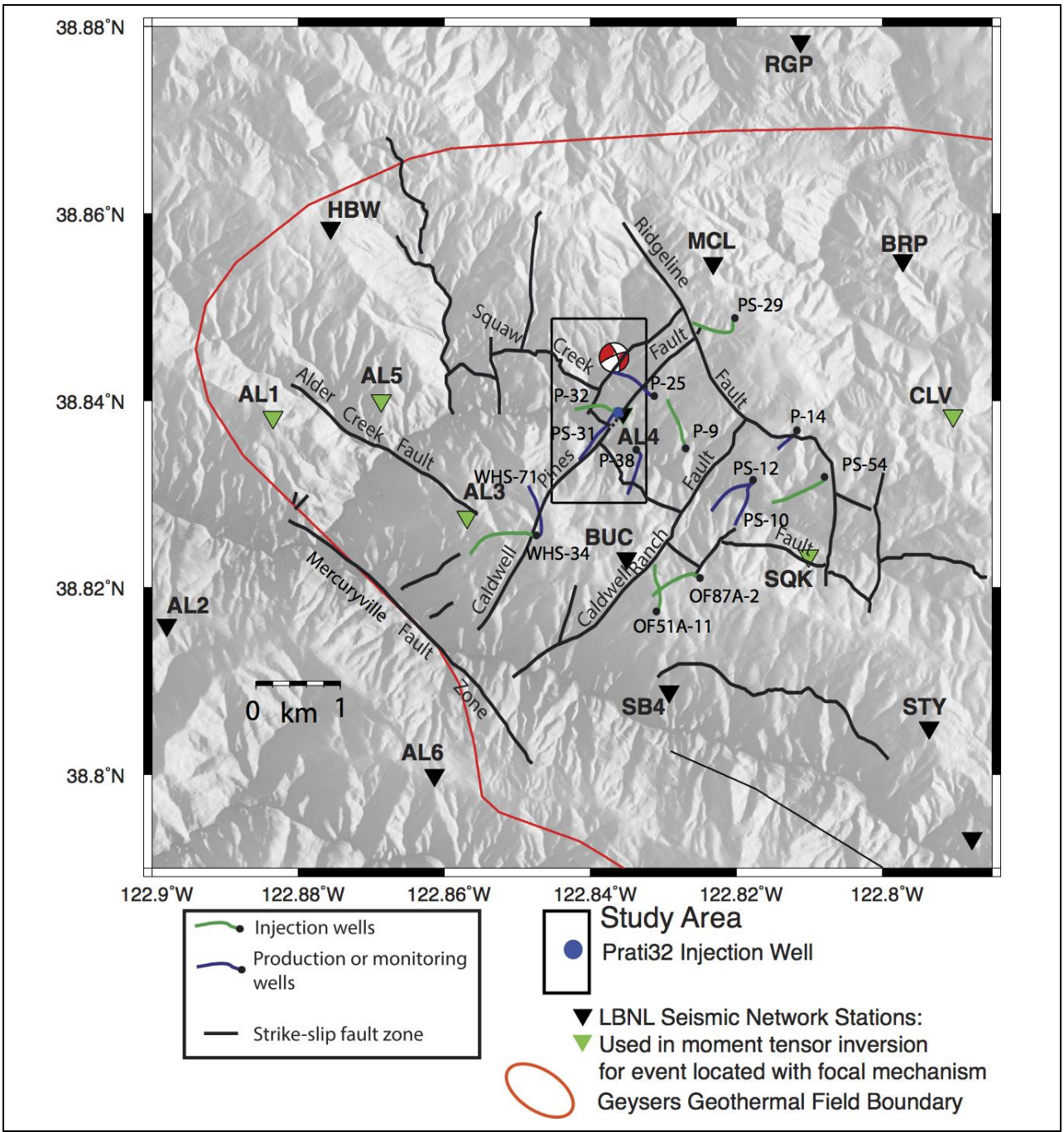

Figure 1.1: Map of the Northwest Geysers with the study area of the EGS indicted by the black rectangle. Trajectories of injection wells (green lines) and production wells (blue lines) are shown. The location of a MW 2.17 2009 November 16 pre-injection event is shown with its focal mechanism. The locations of short-period seismic stations operated by LBNL used in this study are indicated by triangles (data from stations marked by green triangles were used to invert for the moment tensor of the event located with the focal mechanism). The approximate boundary of The Geysers steam field and selected faults are delineated with red and black lines, respectively. Figure adopted from Boyd at al. (2018).

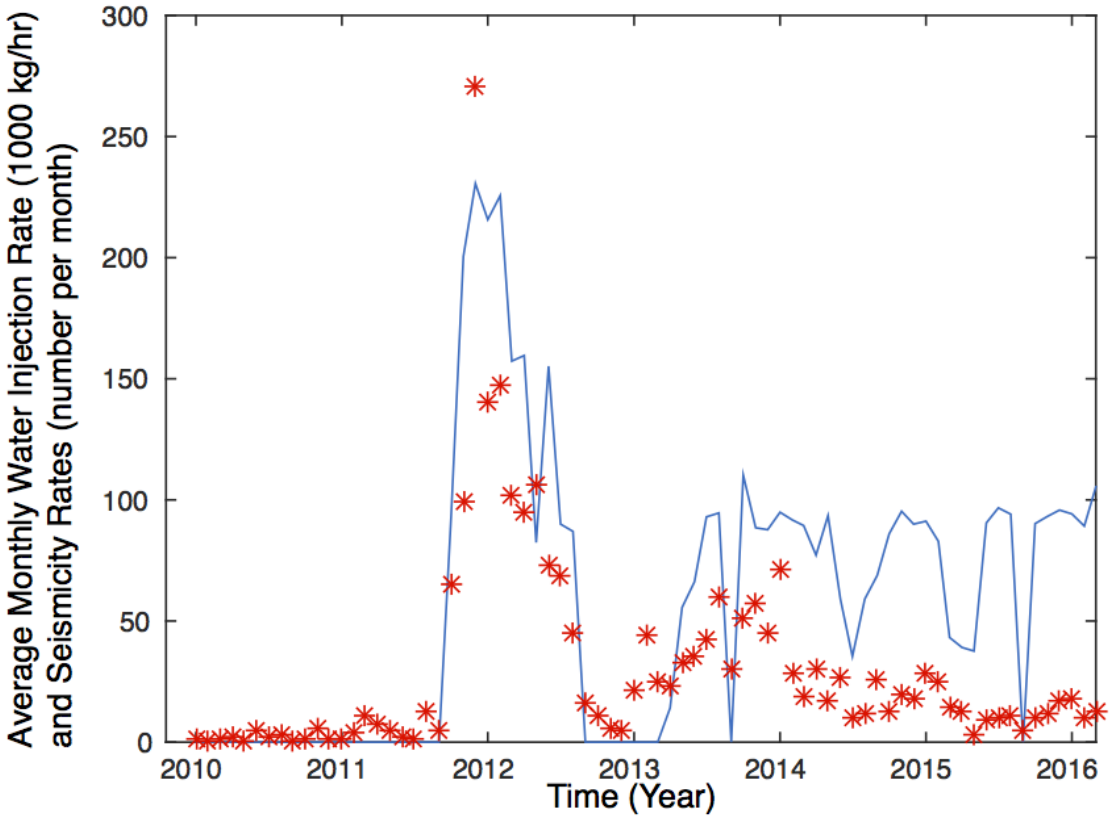

Figure 1.2: Injection rate (1000 kg/hr, blue line) and EGS Berkeley Geysers average monthly seismicity (red asterisks) as a function of time.

2.0 Temporal Analysis of Fluid Injection

The double-difference Wadati (DDW) technique has been applied to estimate temporal changes of fluid distribution in fault zones (Lin and Shearer, 2007, 2009), in volcanic regions (Dahm and Fischer, 2013) and recently engineered geo-reservoirs (Gritto et al., 2016). The application of the DDW technique is based on estimating the ratio of P- and S-wave velocity (Vp/Vs) in the subsurface. Vp/Vs has been used in seismological applications and seismic exploration to probe the subsurface for liquid and gaseous fluids. Applications in the oil and gas industry include analysis of Vp/Vs to trace fluids in reservoirs during second and tertiary oil recovery (Gritto et al., 2004a) as well as during fracking campaigns. Seismological investigations include tracing the movement of fluids during volcanic unrest (Dahm and Fischer, 2013, Lin, 2013) and to image fluids in fault zones (Lin and Shearer, 2007, 2009). In general, high Vp/Vs indicates the presence of liquid fluids in the subsurface (Moos and Zoback, 1983, Gritto et al., 2004b, Gritto and Jarpe, 2014), while low Vp/Vs indicates the presence of gaseous fluids (Julian et al., 1996).

2.1 Double Difference Wadati Method

In this study, we apply the DDW technique based on high-accuracy P- and S-wave differential travel times derived from subsample waveform cross correlation to image fluid saturation in the subsurface based on Vp/Vs-ratio. Lin and Shearer (2007) introduced the method to image fluid saturation along the San Andreas Fault zone in Southern California. The principle of the method is similar to the double-difference location method and is based on the assumption that the propagation paths of the seismic waves from two near-located earthquakes to a distant seismic station are similar, except for the source region. Differencing the observed P- and S-wave travel times at the distant station and plotting these differences on a Wadati diagram will yield estimates of the Vp/Vs ratio in the source region. Waveform cross correlation can be used to estimate the travel time differences for P- and S-waves with high accuracy and was investigated by Lin and Shearer (2007).

The principle of the method is displayed in Figure 2.1, where two events are located close to each other in a source region that is far from the seismic recording stations. Due to the geometrical constraints the ray paths outside the source region to the recording station can be considered the same, while the separation distance between the events in the source region can be defined as δl. If we consider that these two events are recorded by i stations, the differential P-wave travel time δT_P^i between the two events at the recording station i can be expressed by

$$\delta T_P^i = T_{P1}^i - T_{P2}^i = \frac{\delta l_P^i}{V_P} \quad (2.1),$$

Where T_{P1}^i and T_{P2}^i are the travel times from event 1 and event 2 to station i, respectively, $\delta l_P^i$is the difference in ray path between the two events and $V_P$the P-wave velocity in the source region. Similarly, the differential S-wave travel time δT_S^i between the two events at the recording station i can be expressed by

$$\delta T_S^i = T_{S1}^i - T_{S2}^i = \frac{\delta l_S^i}{v_S} \quad (2.2).$$

Under the assumption that the ray paths for P- and S-waves are coincident in the source region, $\delta l_P^i = \delta l_S^i$, it follows that

$$\frac{V_P}{V_S} = \frac{\delta T_S^i}{\delta T_P^i} \quad (2.3).$$

Thus, by measuring the travel time of the P-and S-waves, we can estimate the Vp/Vs ratio in the source region from the arrival times, which, given a number of stations will fall on a line defined by the Vp/Vs ratio in the source region.

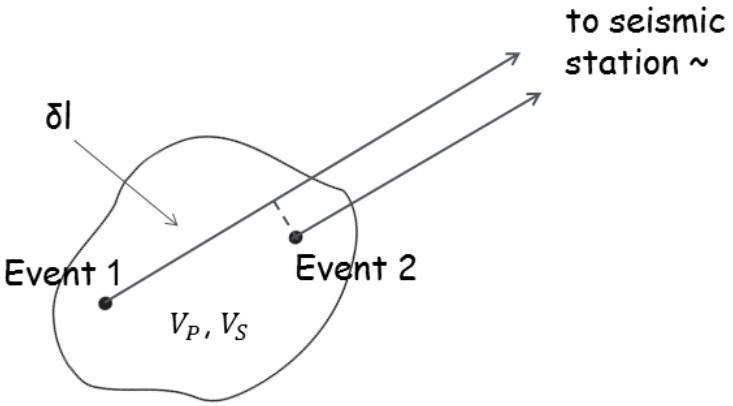

Figure 2.1: Two events located close to each other in the source region, separated by the distance *δl*. If the recording station is located at far distance from the two events, the ray paths from the source region to the seismic station can be considered common.

In typical seismological applications, however, the travel times of the waves from the event location to the stations are not known and what is instead measured is the arrival times $t_{P,S}$ of the P- and S-waves, which is the sum of the origin time of the event $t_0$and the travel times $T_{P,S}$ from the event to the station. So, for two events with origin times t_{01} andt_{02}, the arrival times observed at station *i* can be written as

$$t_{P1}^i = t_{01} + T_{P1}^i \tag{2.4}$$

and

$$t_{P2}^i = t_{02} + T_{P2}^i \tag{2.5}.$$

Differencing equations (4) and (5) yields

$$\delta t_P^i = \delta t_0 + \delta T_P^i \tag{2.6}$$

and

$$\delta T_P^i = \delta t_P^i - \delta t_0 \tag{2.7}.$$

Similarly, for the S-waves we obtain

$$\delta T_S^i = \delta t_S^i - \delta t_0 \tag{2.8}.$$

Combining equations (3), (7) ad (8) yields

$$\frac{V_P}{V_S} = \frac{\delta t_S^i - \delta t_0}{\delta t_P^i - \delta t_0} \tag{2.9}.$$

In intercept form equation (9) can be rewritten as

$$\delta t_S^i = \left(\frac{V_P}{V_S}\right) \delta t_P^i + \delta t_0 \left(1 - \frac{V_P}{V_S}\right) \quad (2.10),$$

which shows that the differential origin time δt_0 represents the intercept of the line with slope Vp/Vs.

The concept of this formalism is presented in Figure 2.2, where the differential arrival times of two events from the earthquake cluster below the EGS injection experiment at Prati-32 in the NW Geysers is shown. The black colored symbols represent the differential arrival times computed for two closely located events with different origin times, recorded by 34 stations of the LBNL geophone network. For this numerical experiment, a homogeneous Vp/Vs ratio of 1.732 is assumed for the volume of The Geysers below the geophone stations. Consequently, the symbols lie on a line with a slope of 1.732 and intercept $\delta t_0 \left(1 - \frac{V_P}{V_S}\right)$. The difference between the lines with the black and red symbols in Figure 2.2 is a shift in x- and y-direction by the differential origin time δt_0. Shifting the black symbols to the origin, i.e., transforming them into the red symbols is equal to setting the intercept term in equation (10) equal to zero. This is an important step, considering that many events pairs with varying differential origin times will be used during the analysis. Shifting each of datasets that resulted from different event pairs to the origin yields a common set of differential travel time estimates that lie on a straight line with slope Vp/Vs. The slope of the resulting set of data points can subsequently be estimated by linear fitting techniques. Shifting each set of data points to the origin can be accomplished by subtracting the mean of the data points from each individual point, as illustrated in Figure 2.2.

A more complete illustration of differential arrival times for a number of events is presented in Figure 2.3. The symbols in Figure 2.3a represent numerically calculated differential arrival times for a cluster of events located below the EGS injection project in the NW Geysers and recorded by the 34 station LBNL geophone network. Again, a homogeneous Vp/Vs ratio of 1.732 is assumed for the volume of The Geysers below the geophone stations. Therefore, the resulting differential arrival times are located on lines with a slope of 1.732 but shifted in space by the varying differential origin times of each earthquake pair. To better illustrate the parallel nature of the slopes, the time scale of the axes is increased in Figure 2.3b.

Demeaning each slope in Figure 2.3, by the mean of the differential arrival times, yields the data in Figure 2.4a. It can be seen that after demeaning all data points fall on a single line through the origin. Fitting the slope of the points with a linear least squares technique in Figure 2.4b, yields a slope of 1.732, which is the Vp/Vs ratio used to generate these data.

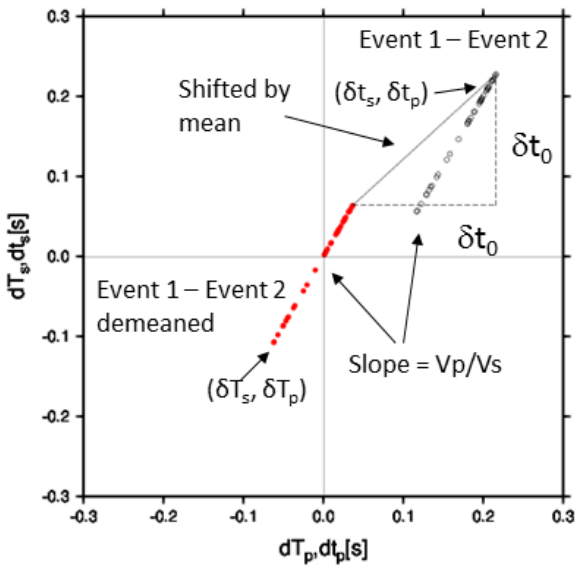

Figure 2.2: Sketch to illustrate the difference between differential arrival times (δt_S, δt_P) and demeaned differential travel times (δT_S, δT_P). The black symbols represent the differential arrival times from two events recorded by one station. The red symbols represent the differential travel times from two events recorded by one station, obtained by demeaning the black symbols.

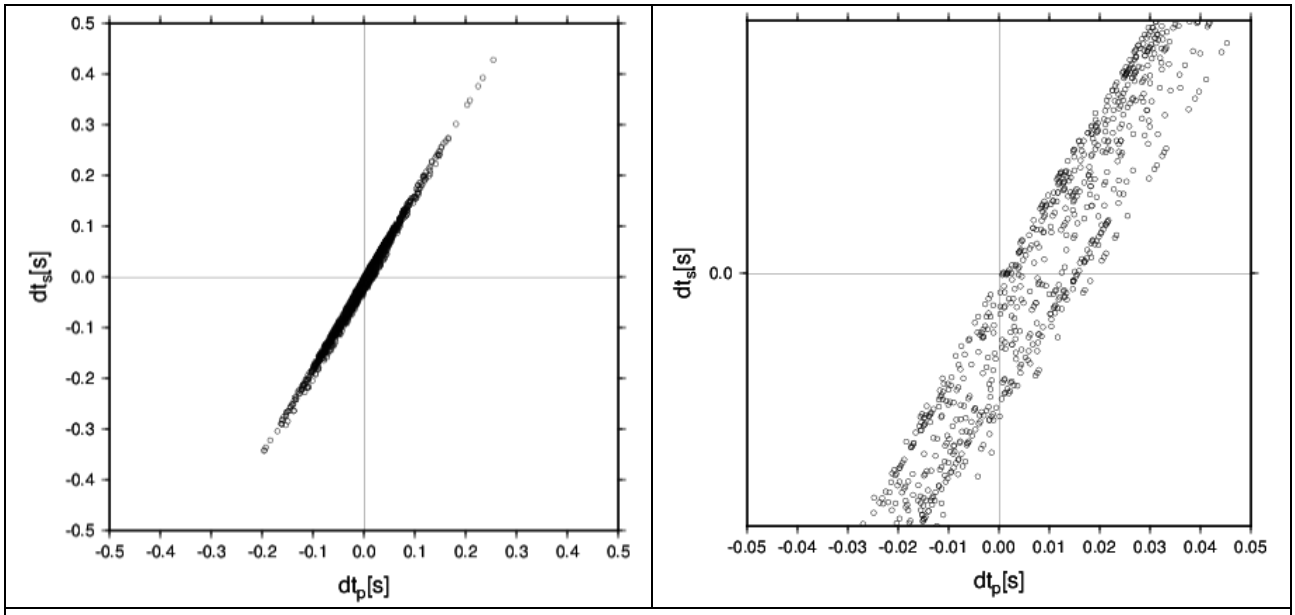

Figure 2.3: a) Differential arrival times for a cluster of events located below the EGS injection project in the NW Geysers and recorded by the 34 station LBNL geophone network. **b)** Same as a) with magnified time scale to illustrate the data points on parallel lines with the same slope each.

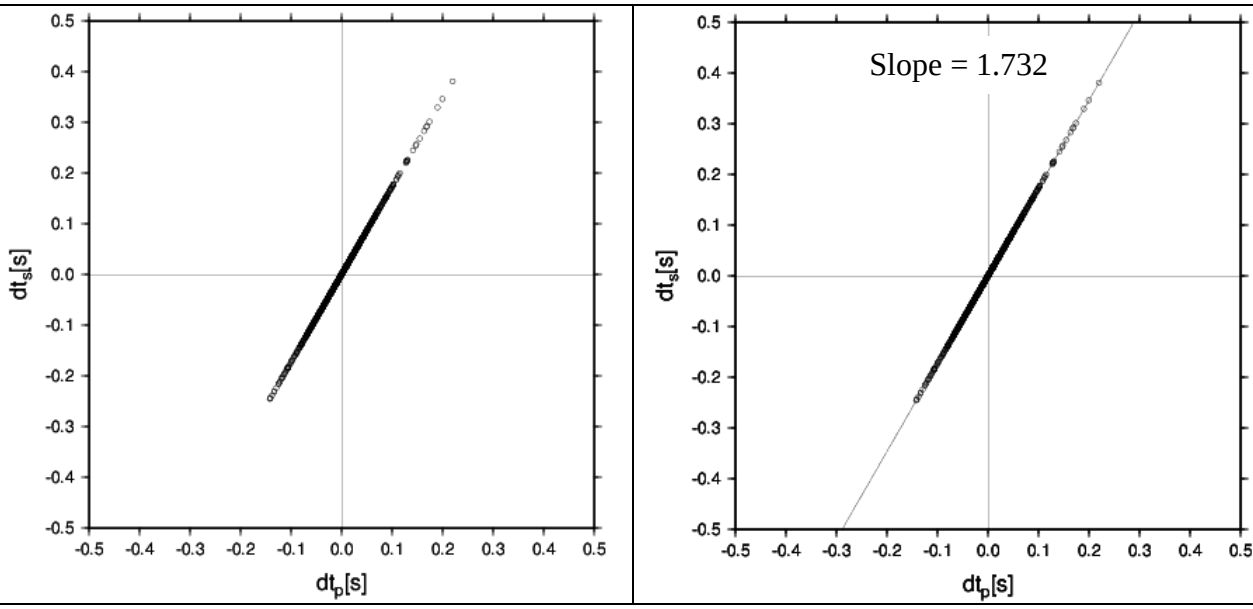

Figure 2.4: a) Demeaned differential arrival times for the data points in Figure 2.3. **b)** Same as a) with a slope fitted using linear least squares. The resulting slope of 1.732 is the same as the Vp/Vs ratio used below the seismic network at The Geysers.

2.2 Robust Fitting of Noise-Contaminated Data

The above example yielded the correct Vp/Vs ratio since the numerical data were noise free. However, real travel time data typically include noise caused by errors related to the determination of phase arrivals. In the next numerical experiment, we added Gaussian distributed noise with zero mean and 10 ms standard deviation to both P- and S-wave differential arrival times, which represents a relatively large error for seismic data recorded at The Geysers. In order to simulate outliners in real data, we added uniformly distributed noise with a standard deviation of 0.3 s to 5% of the differential P-wave travel time data. The resulting demeaned data are displayed in Figure 2.5. It can be seen how the cloud of differential travel times is spread out due to the addition of noise in the data.

When trying to employ linear least squares fitting techniques it is important to consider which data points are affected by noise. In the present case, Gaussian distributed noise was added to both differential P- and S-wave arrival time, while uniformly distributed noise was added as outliers to the differential P-wave arrival times. Often times least squares fitting of (x,y) data points is based on the assumption that only the x-data points are affected by errors, while the y-data points are assumed error free. When such assumption is made in the current example and a straight line is fitted to the data in Figure 2.5 using linear least squares, the resulting slope yields a value of 0.894, as displayed in Figure 2.6a. The problem with this example is that the fitting is greatly affected by the outliers in the differential P-wave travel times and by the errors that are present in both differential P-wave (x-values) and differential S-wave (y-values) travel time data. The estimate of the slope improves, when errors in both variables are assumed during

the least squares fitting process. However, the resulting slope with a value of 1.411 is still far off the true value of 1.732, as can be seen in Figure 2.6b. Thus, an improved fitting procedure is needed for the current example.

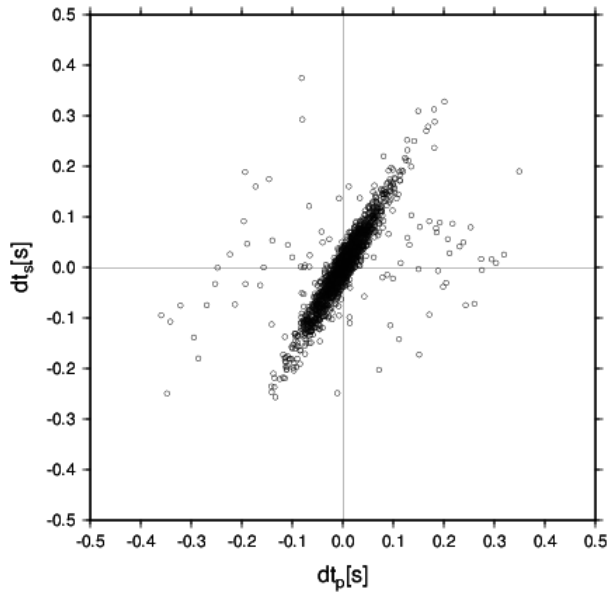

Figure 2.5: Demeaned differential arrival times for a cluster of events located below the EGS injection experiment in the NW Geysers. The data have been randomized by Gaussian and uniformly distributed noise.

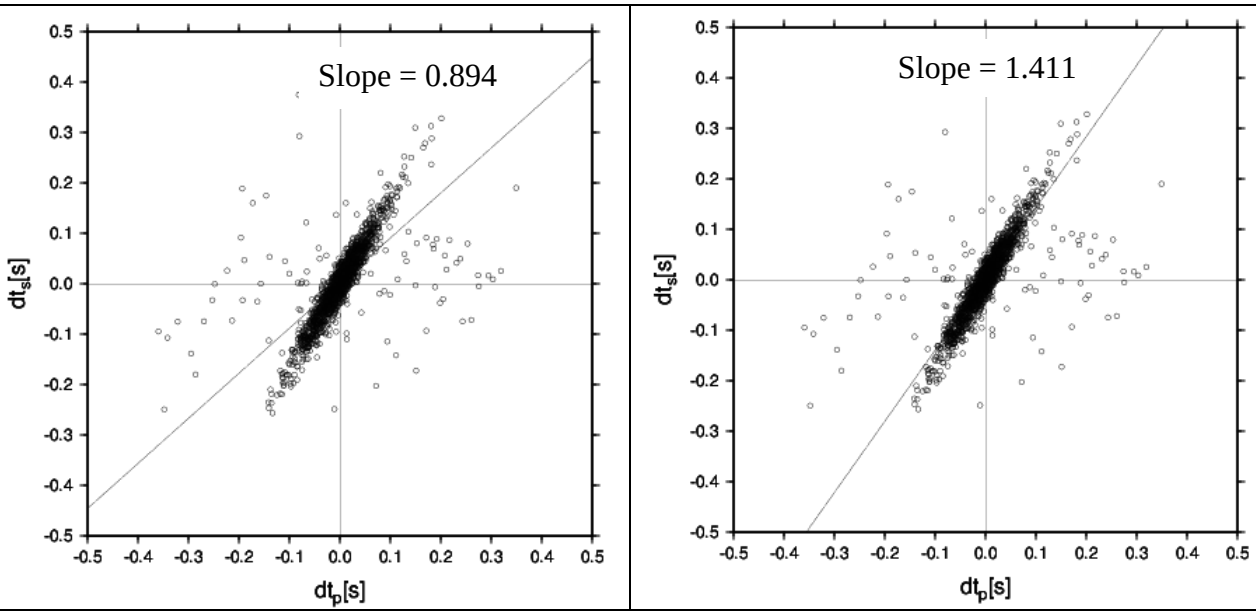

Figure 2.6: a) Data from Figure 2.5, fitted with a linear least squares technique while assuming errors in the differential P-wave arrival times only. **b)** Same as a) but with errors assumed in both differential P- and S-wave arrival times.

In cases where data points may be affected by errors in both variables in addition to large outliers, as in the example in Figure 2.5, a different fitting procedure is necessary. In these cases, the principle of least absolute deviations is employed, which minimized the sum of linear deviations, rather than its square as in least squares fitting. The technique, also referred to as median fitting, is based on the underlying principle that the median of a set of numbers is also that value which minimizes the sum of the absolute deviations. We applied a median fitting technique to the dataset in Figure 2.5, which resulted in the fit displayed in Figure 2.7. It is evident that the fit with a slope of 1.520 is better than that in Figure 2.6b, however, the estimate is still far off the underlying Vp/Vs ratio of 1.732.

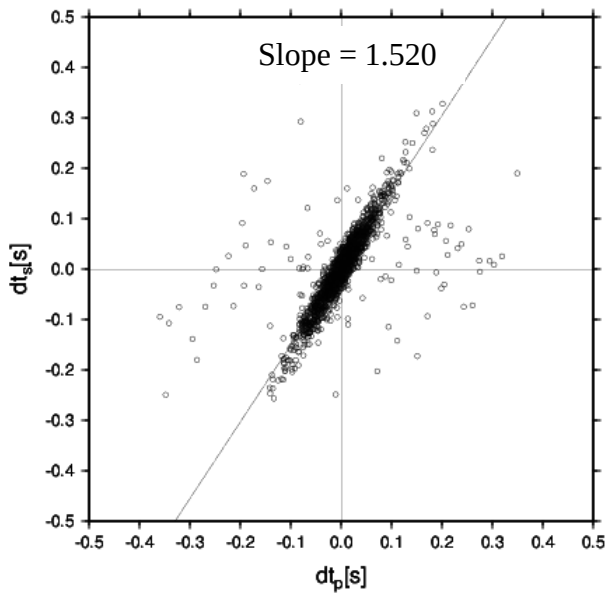

Figure 2.7: Data from Figure 2.5, fitted with a least absolute deviation technique.

The numerical experiments above reveal that in cased were errors of different magnitude are present in the data, typical fitting approaches based on minimizing either the sum of linear deviations or the sum of squared deviations is not applicable. The fitting of seismic travel time data is such a situation as shown in the example above. In this situation, a more robust fitting technique is required. Therefore, we implemented and tested the robust L1-L2 norm, which is based on different minimization depending on the error in the data (Huber, 1973). In those cases where the data misfit is less than a specified distance the L2 norm is applied, and for larger distances the L1 norm. Distance in this case is perpendicular to the fitted slope, to account for error in both, differential P- and S-wave arrival times. In the current case, we apply a grid search method to fit lines of varying slopes through the data cloud in Figure 2.5. The fitting technique is refined by eliminating 10% of the data points with the largest distance from the fitted line. In the current case, this step eliminates most of the outliers in the data. The next 30% of points with the largest distance to the fitted line will be fitted by the L1 norm, while the remaining 70% will be fitted by the L2 norm. The resulting norms will be summed for each line and slope and the minimum norm yields the best estimate for the fit through the data. Using this technique, we

obtained the result in Figure 2.8, which produces a best fit for a line with slope of 1.743. This value is only 0.6% off the true Vp/Vs ratio of 1.732.

This example shows the robustness of the L1-L2 norm in cases where data are contaminated by errors in both variables including outliers in some of the data. The uncertainty added to the data points, including Gaussian distributed noise with zero mean and 10 ms standard deviation to both P- and S-wave differential arrival times and uniformly distributed noise with a standard deviation of 0.3 s to 5% of the differential P-wave travel time data, constitutes a maximum limit to the error that can be expected in the seismic data recorded at The Geysers. Therefore, this fitting technique appears best suited to estimate Vp/Vs ratio from Wadati diagrams for earthquakes related to the EGS experiment at The Geysers geothermal reservoir. Uncertainties for the estimate of the slope are obtained by bootstrapping the data points in Figure 2.8a. The frequency distribution of 1,000 bootstrapping realization is presented by the histogram in Figure 2.8b). The resulting uncertainty amounts to $\sigma = 0.015$.

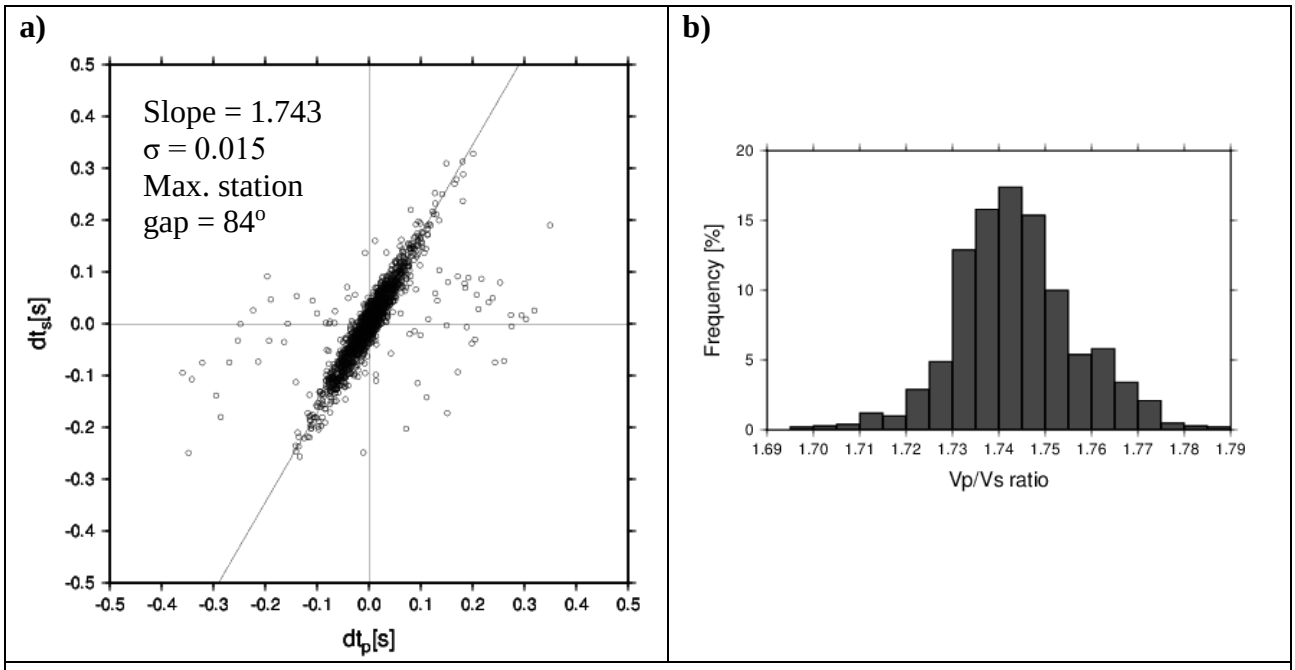

Figure 2.8: a) Data from Figure 2.5, fitted with a fitting technique based on the robust L1-L2 norm. The resulting slope of 1.743 is only 0.6 % off the exact value of 1.732. **b)** Histogram with slope estimates from bootstrapping the data in a) resulting in an uncertainty of $\sigma = 0.015$.

The distribution of stations around the earthquake cluster is important for a stable Vp/Vs estimate. The take-off angles of the P- and S-waves from the source region should sample the source volume homogeneously. Therefore, situations where the ray paths sample only one hemisphere of the source volume should be avoided. In the present numerical example, the distribution of sources in the study area, and the inclusion of all stations in the geophone network, resulted in a maximum station gap of 84°. This gap constitutes the best-case scenario for the geometry at Prati-32. However, the value is well below our threshold of 150°, which constitutes an upper limit to assure a well sampled source volume.

2.3 Alternative Waveform Correlation Techniques

In our study we apply waveform cross correlation to the seismic data recorded during the Prati-32 EGS demonstration project. However, we first investigate a method suggested by Taira and Kato (2013), which estimates travel time differences by combining waveform cross correlation with a multiple sliding window approach that promises more stable time estimates. The principle is shown in Figure 2.9, where two recorded waveforms from nearby events recorded at the same station are shown. The origin times for events 1 and 2 are t_{o1} and t_{o2}, respectively. The P- and S-wave travel times for events 1 and 2 are, T_{p1}, T_{p2}, T_{s1} and T_{s2}, respectively, while the differential travel times are denoted by δt_p and δt_s. The differential travel times for the P- and S-waves recorded at station *i* can be represented by

$$\delta t_p^i = \left(T_{p1} - t_{0_1}\right) - \left(T_{p2} - t_{0_2}\right) \tag{2.11}$$

and

$$\delta t_s^i = \left(T_{s1} - t_{0_1}\right) - \left(T_{s2} - t_{0_2}\right) \tag{2.12}.$$

Once the waveforms are correlated by the P-wave arrivals and shifted by their lag, they are displayed in Figure 2.10. It can be seen that the waveforms are lined up at their respective P-wave arrival times and that the S-wave arrivals are now separated by $t_{sp2} - t_{sp1}$, where t_{sp} is the travel time between the P- and S-arrival of the seismic wave. With the notation in equations (11) and (12), the differential times δt_p and δt_s can be expressed as

$$\begin{aligned}
\delta t_s^i &= \left(T_{s1} - t_{0_1}\right) - \left(T_{s2} - t_{0_2}\right) \\
&= \left(T_{p1} + t_{sp_1} - t_{0_1}\right) - \left(T_{p2} + t_{sp_2} - t_{0_2}\right) \\
&= \left(T_{p1} - t_{0_1}\right) - \left(T_{p2} - t_{0_2}\right) - \left(t_{sp_2} - t_{sp_1}\right) \\
&= \delta t_p^i - \left(t_{sp_2} - t_{sp_1}\right)
\end{aligned} \tag{2.13}.$$

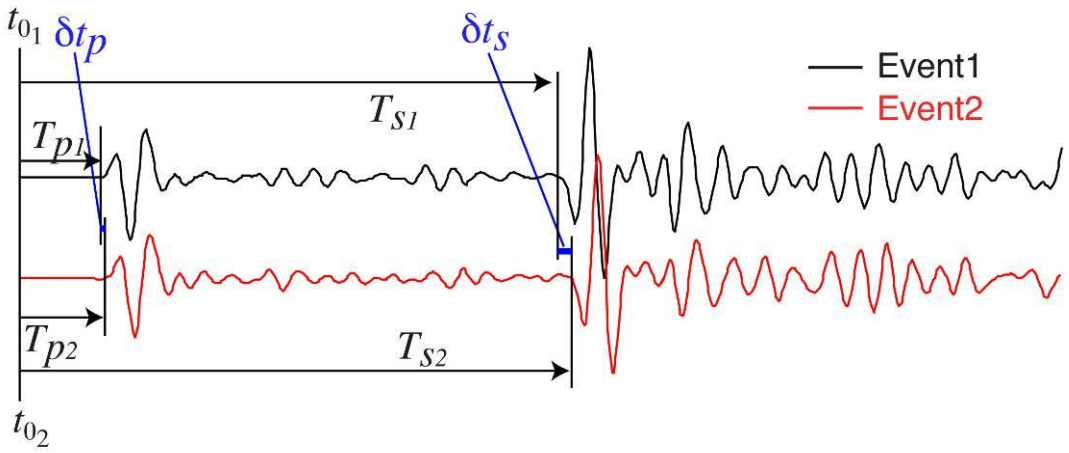

Figure 2.9: Principle of two waveforms recorded by the same station from near-located events (Taira and Kato, 2013).

After the waveforms have been lined up at their respective P-arrival times, waveform cross correlation with a sliding window can be applied to both records. The principle is presented in Figure 2.11, which reveals two vertical-component seismograms, recorded by the Geysers geophone network station MCL from two co-located events. It can be seen that the waveforms are lined up at their P-wave arrival. A moving time window (gray shaded area in Figure 2.11) is sliding along the waveforms, with a 50% overlap, computing the phase lag based on waveform cross correlation. The lag is plotted in delay time as a function of elapse time from the P-wave arrivals. Each dot in the plot denotes the phase lag computed in each time window (gray shaded area). It can be seen that after the onset of the P-wave energy, the phase lag remains close to zero for the P-wave coda. However, as soon as S-wave phases are present in the time window, the phase lag increases, as can be seen by the jump in the function denoted by *b*. Shifting the correlation window past the S-wave phase arrivals into the S-wave coda produces lags that are similar to the first encountered S-wave lag. The time dependence of the delay time can be fitted by an exponential step function as shown in equation 14.

$$f(t) = \frac{b}{1 + \exp\left[-2c\left(t - a\right)\right]} \qquad (2.14).$$

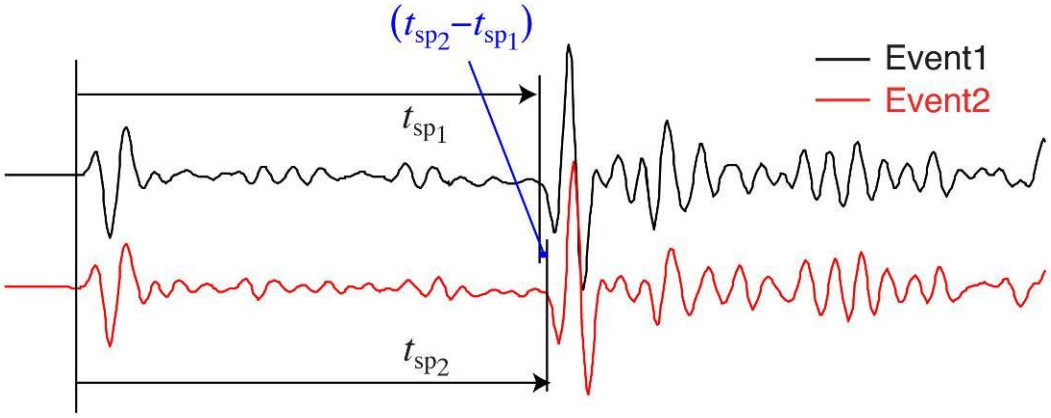

Figure 2.10: Two waveforms recorded by the same station from near-located events, shifted in time by their lag in P-wave arrival times (Taira and Kato, 2013).

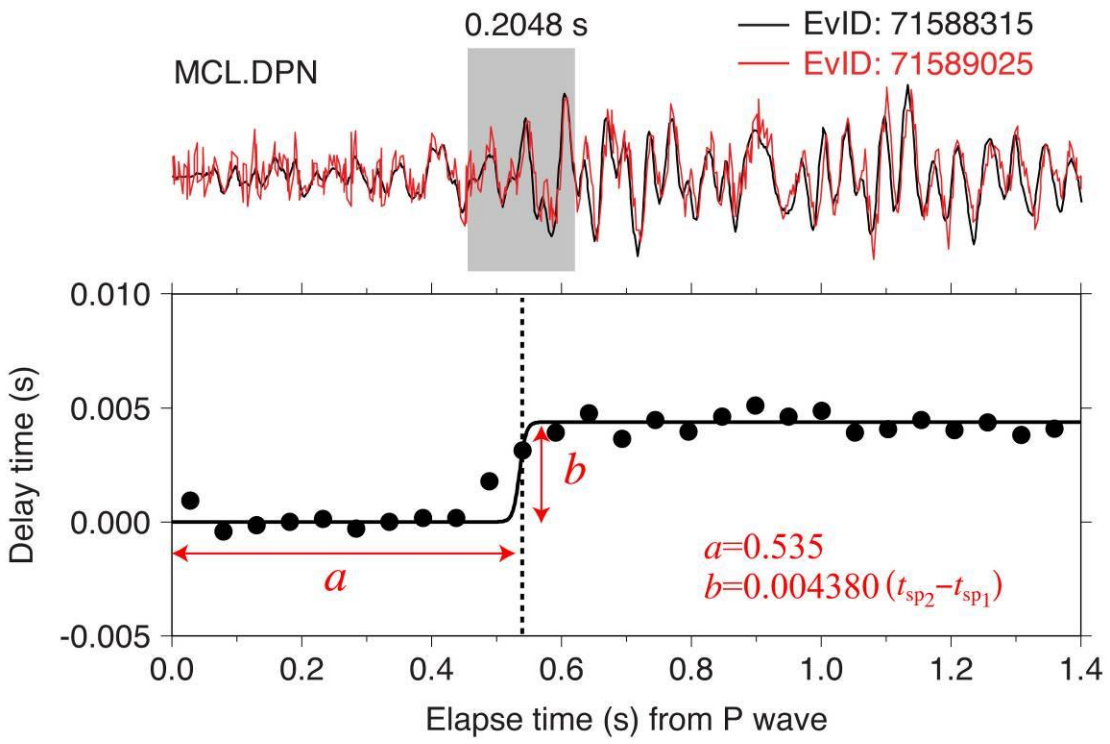

Figure 2.11: Two waveforms recorded at The Geysers by station MCL from co-located events (top). The gray-shaded area represents the time window that is shifted along the time axis and in which time lags between the seismograms are computed by waveform cross correlation. The lags are subsequently plotted as delay time as a function of elapse time from the P-wave arrival (bottom).

The unknown parameters *a* and *b*, can be estimated by minimizing the misfit in a least squares sense, while the parameter *c* can be pre-set to an assumed value, representing the steep step at the onset of the S-wave. The estimate for the parameter *b* is equal to $\left(t_{sp_2} - t_{sp_1}\right)$ and thus with the already determined P-wave differential time δt_p, the differential S-wave time δt_s can be determined as shown in equation (3).

The advantage of the method by Taira and Kato (2013) lies in more accurate differential estimates, particularly in the presence of noise. While standard cross correlation techniques yield single estimates for the differential times of P- and S-waves, the presented approach generates multiple estimates for the time lags and thus offers a means to fit the estimates in a least squares sense. The differential travel times obtained by moving-window cross correlation typically result in more accurate estimates of the Vp/Vs ratio. It is noted, however, that the correlation between the two waveforms needs to be high, to assure that the phases in the P-wave coda propagate along the same path and not violate the common path assumption.

2.4 Application of the Double-Difference Wadati Method to The South-Central Geysers

The DDW method by Taira and Kato (2013) was first applied to a cluster of seven earthquakes in the south-central Geysers. Because the seven analyzed events are practically co-located and difficult to separate in map view, the epicentral centroid location of the events is marked by the white circle in Figure 2.12. Despite the relatively low number of events, 29 stations from the LBNL seismic network recorded P- and S-waveform data, which resulted in 538 pairs of differential P- and S-wave arrival times. The demeaned differential travel times are plotted on the Wadati diagram in Figure 2.13. The red, blue, green and black lines represent, respectively the fits for LSQR fitting assuming errors in x only, LSQR fitting assuming errors in x and y, least absolute deviation fitting, and fitting using the robust L1-L2 norm (see section 2.1). The resulting slope for the robust L1-L2 norm is 1.54. Bootstrapping the differential travel time data in Figure 2.13 yields an uncertainty of $\sigma = 0.05$. The maximum station gap associated with this analysis is 86°, which is close to the optimum value of 84° as determined for the Prati-32 and LBNL network geometry (see section 2.2). This low maximum gap is due to the high number of stations that recorded the 7 events.

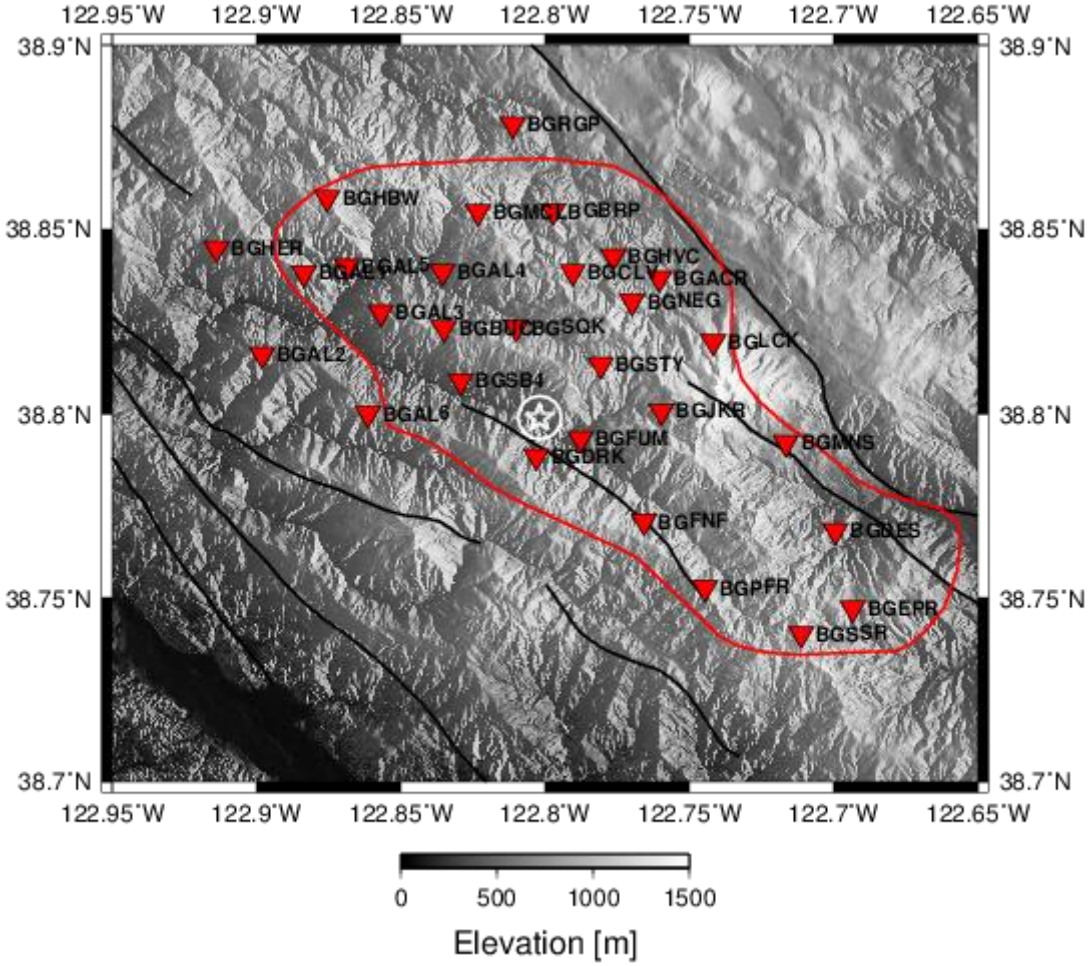

Figure 2.12: Map of The Geysers geothermal reservoir with the epicenters of the 7 co-located earthquakes denoted by the white stars inside the white circle in the south-central part of the reservoir. The red triangles denote the stations, where P- and S-waveform data were recorded for each event.

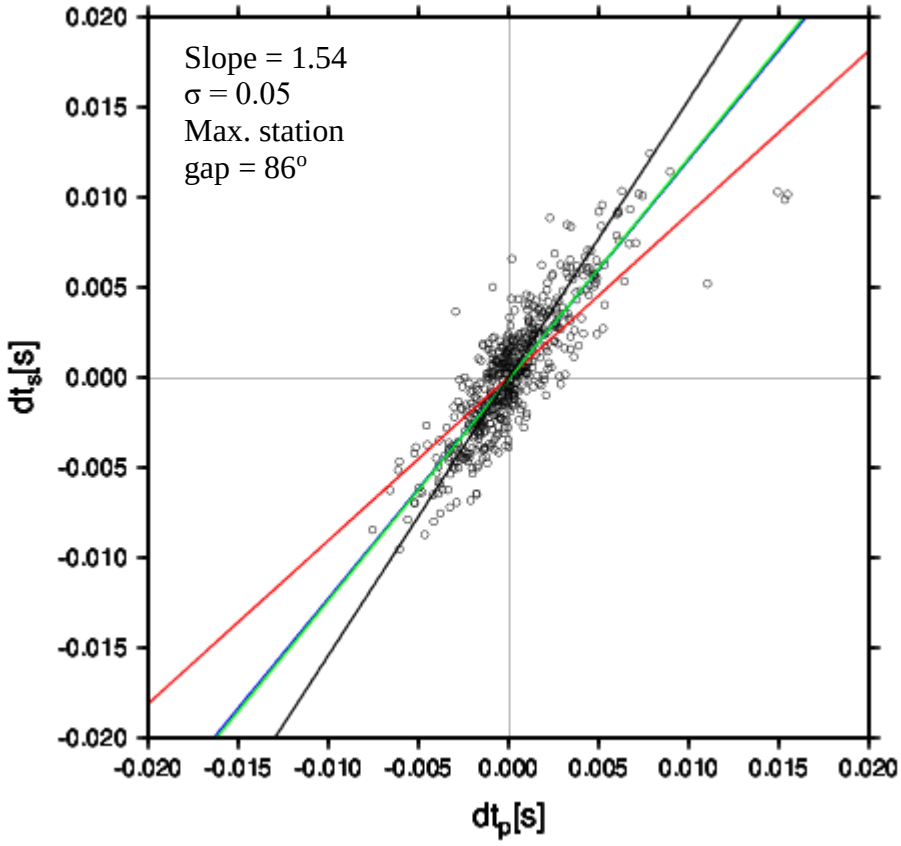

Figure 2.13: Wadati diagram with demeaned differential P- and S-wave travel times from the cluster of events located within the white circle in Figure 2.12. The red, blue, green and back lines denote, respectively, fits obtained with LSQR assuming uncertainty in x (slope: 0.90), LSQR assuming uncertainty in x and y (slope: 1.22), least absolute deviation slope: (1.23), and the robust L1-L2 norm (slope: 1.54).

A low Vp/Vs-ratio of 1.54 is typically associated with gaseous subsurface fluids. In the case of The Geysers the most likely explanation for such values is the presence of steam, which is ubiquitous in the south-central Geysers. In can be seen in Figure 2.12 that the white circle is located next to station FUM (Fumarole). The name is derived from fumaroles that are found at the surface, venting steam from the subsurface. A photograph of the area is shown in Figure 2.14a. Furthermore, the fault trace to the south of the white circle in Figure 2.12 is that of the Big Sulfur Creek Fault. The name is derived from sulfur deposits on the exposed rock faces along the fault trace. These sulfur deposits are the results of chemical reactions of the venting steam with the exposed rocks along the fault trace. Furthermore, Gritto et al. (2013), conducting a high-resolution seismic tomography study, reported Vp/Vs-ratios ranging from 1.47 to 1.64 in the vicinity of the fumarole area (Figure 2.14b). Thus, there exists multiple evidence that the region occupied by the earthquake cluster in Figure 2.12 is saturated with steam and that the results obtained by the double difference Wadati method are accurate.

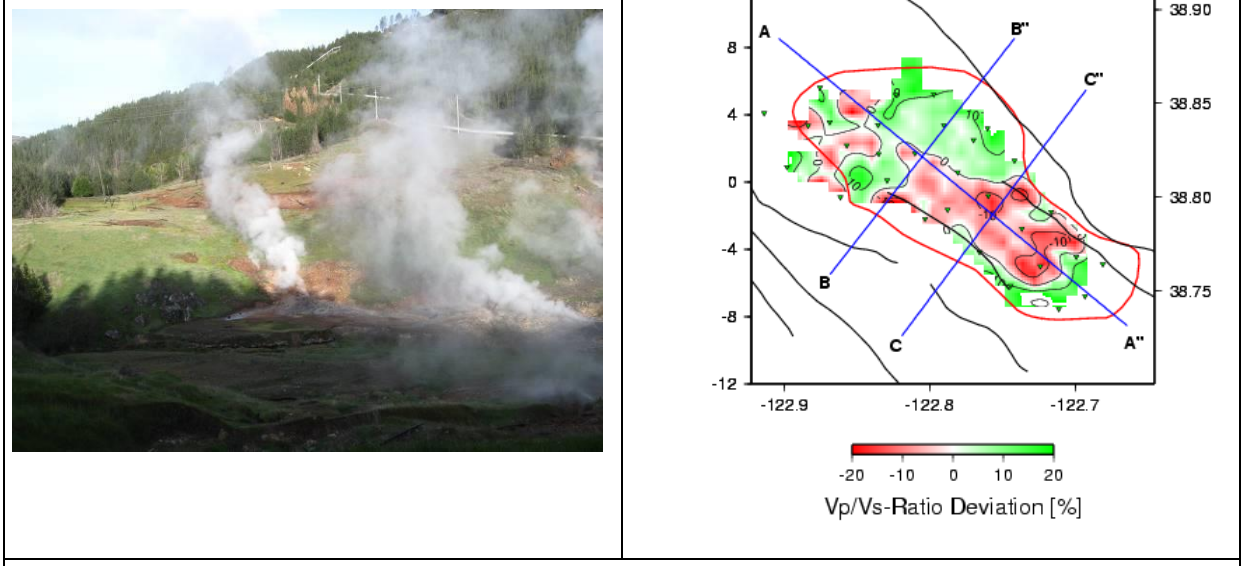

Figure 2.14: a) Photograph of the fumarole area in The Geysers geothermal reservoir. The area is in the vicinity of the cluster with events denoted by the white circle in Figure 2.12. **b)** Horizontal depth section of Vp/Vs estimates at 0.9 km reservoir depth (from Gritto et al., 2013).

2.5 Application of the Double-Difference Wadati Method to the Prati-32 Study Area

The DDW was subsequently applied to the Prati-32 study region to investigate the temporal changes in Vp/Vs associated with the EGS experiment. Since the injection occurred in a section of the reservoir that was not previously utilized for production there existed a paucity of earthquakes in the study area. Therefore, events from two years prior to injection were considered to obtain a baseline estimate for the Vp/Vs ratio. The search resulted in 179 events with differential P- and S-wave travel times. Figure 2.15a displays the pre-injection events, located within the study area of Prati-32 and the 19 seismic network stations that recorded the P- and S-wave data that were used to estimate the pre-injection Vp/Vs ratio. Traditional waveform cross correlation with windows centered on the P- and S-wave travel times was used to analyze the events within the Prati-32 study area. The reason that traditional waveform cross correlation was chosen was lower correlation coefficient for the waveforms of neighboring events than required by the method by Taira and Sato (2013). The Wadati diagram with the resulting 626 differential P- and S-wave travel times is shown in Figure 2.15b. The estimate of the slope of the line fitted by the L1-L2 norm is 1.76. This value is slightly higher than that of a perfectly elastic rock (1.732) possibility indicating a weakly fractured rock partially saturated with water. Bootstrapping the data in Figure 2.15b yields a standard deviation of σ=0.04, while the

maximum station gap is 84°. These results indicate that the methodology produced a reliable estimate of the Vp/Vs-ratio.

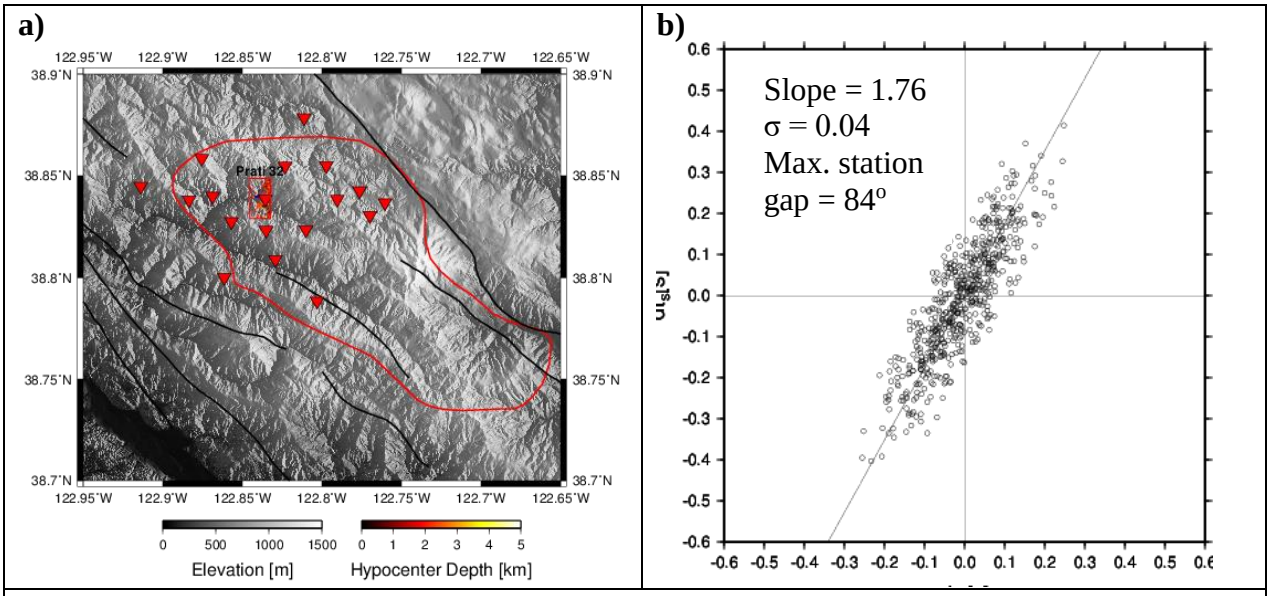

Figure 2.15: a) Map of the study area of Prati-32 with epicenters of two years post-injection seismicity. The red triangles denote the 19 seismic stations that recorded post-injection seismicity. **b)** Wadati diagram with 626 differential P- and S-wave travel time pairs determined for the events in a).

Injection at Prati-32 started on October 6th, 2011. Soon after, the study area around the injection well experienced a strong increase in seismicity. Because the number of earthquakes were much higher than during the pre-injection phase, three months of seismicity, recorded after the start of injection, was sufficient for a reliable estimate of the Vp/Vs-ratio. The post-injection seismicity and the 16 seismic stations that recorded the events are shown in Figure 2.16a, while the resulting 1,703 differential P- and S-wave travel times are presented on the Wadati diagram in Figure 2.16b. The estimate of the slope fitted with the L1-L2 norm amounted to 1.67, while the uncertainty from bootstrapping the data points yielded a value of σ=0.04. In contrast to the pre-injection events, the magnitude of the post-injection events was lower resulting in a reduced number of seismic stations recording the post-injection events (19 pre-injection vs. 16 post-injection). Consequently, the maximum station gap increased to 117°. Nevertheless, the gap is sufficiently small to produce a reliable estimate of the Vp/Vs-ratio.

The pre-injection Vp/Vs-ration of 1.76 is slightly higher than that of a perfectly elastic rock (1.732) representing a somewhat fractured rock partially saturated with water. Injecting water into the high-temperature (~300 °C) reservoir will likely result in water flashing to steam, which in turn would lower the Vp/Vs-ratio. The results of a drop from 1.76 to 1.67 for the Vp/Vs-ratio obtained in our analysis support the interpretation of the generation of steam during the early injection phase of the EGS project.

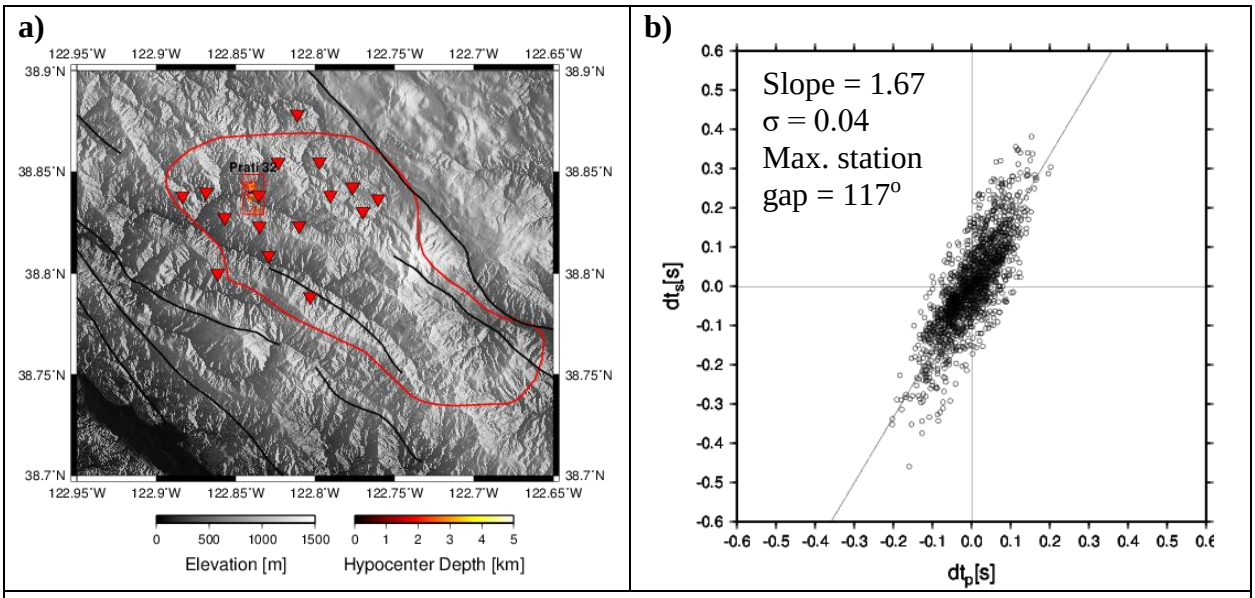

Figure 2.16: a) Map of the study area of Prati-32 with epicenters of three months post-injection seismicity. The red triangles denote the 16 seismic stations that recorded pre-injection seismicity. **b)** Wadati diagram with 1,703 differential P- and S-wave travel time pairs determined for the events in a).

3.0 Source Parameter Determination

Seismic moment tensor analysis is now routinely performed by global and regional monitoring observatories around the world. The seismic moment tensor has been used to characterize the mechanisms of earthquakes occurring in a variety of environments including tectonic faulting, geothermal and volcanic systems, glacial systems, and resulting from human activities such as nuclear explosion monitoring, mining operations and hazard forensics, and during operations involving the introduction of fluids underground. In our previous work, we have investigated M > 3.5 earthquakes at The Geysers geothermal field using regional broadband data, finding evidence of volumetric elements to the moment tensor indicating fluid involvement during the source process (e.g., Boyd et al., 2015). A challenge to moment tensor analysis of events during EGS activities is the low magnitudes of the events requiring the simultaneous use of multiple data types in order to constrain the seismic moment tensor. We have developed a method that enables the simultaneous inversion of seismic waveforms and P-wave first-motion polarities in the Hudson et al. (1989) or Tape and Tape (2014) source-type space (e.g., Nayak and Dreger, 2014, 2015) that finds not only the best fitting mechanism, but also characterizes the nature of possible non-double-couple seismic radiation and its uncertainty.

Robust catalogs of focal mechanisms are needed to track the change in in-situ stress during EGS activities, which can be used to characterize the seismically active fracture network (see section 8). Given the focal mechanisms it is then possible to use empirical Green's function

(EGF) methods to estimate the seismic moment rate function, which can be used to develop catalogs of event stress drop, and more importantly the finite extent of earthquake slip using kinematic finite-source inversion (e.g., Mori and Hartzell, 1990; Dreger, 1997; Dreger et al., 2007) as presented in section 5. In addition, focal mechanism catalogs themselves can be inverted for the in-situ principal stresses (e.g., Michael, 1987; Hardebeck and Michael, 2006) as shown in section 8.

During this task, we investigate seismicity in the vicinity of The Geysers Pratti-32 injection well for a period from two years prior to the start of EGS injection activities to three years after the start of injection. For this project we have incorporated the capability of simultaneously inverting full waveform data and body wave amplitude ratios. The basic idea is that improved estimates of the source mechanism of small events, including the strike, rake and dip of activated faults including the scalar seismic moment is achievable by combining sparse observations of waveforms, first-motions and amplitude ratios.

3,1 Semi-Automatic Moment Tensors Analysis

The LBNL seismic network currently consists of 34 three-component short-period (4.5 Hz) geophones sampled at 500 Hz (Majer and Peterson, 2007). A subset of seismic stations used for the moment tensor analysis study was shown in Figure 1.1. Earthquakes with magnitude $0.6 \geq M \geq 3.87$ (DOE Enhanced Geothermal System Earthquake Catalog) were chosen for computations of deviatoric [double-couple (DC) + compensated linear vector dipole (CLVD)] and full [DC + CLVD + isotropic (ISO)] moment tensor solutions for 167 events within the EGS study area. According to Majer and Peterson (2007), events are located to within 100 m accuracy in the SE Geysers with the LBNL seismic network. For the largest earthquake during the injection period, Mw 3.87, the moment tensor solution was determined using the Berkeley Seismological Laboratory (BSL) moment tensor interface and broadband data from the Berkeley Digital Seismic Network (BDSN). Data for the $0.6 \leq M \leq 3.2$ events are obtained from the local LBNL short-period seismic network. The seismic waveform data are processed by removing the instrument response to ground velocity followed by bandpass filtering of the waveforms with a causal 4th-order Butterworth filter with corners at 0.7 and 1.7 Hz (0.6 to 1.4 s period) for $1 \leq M < 2.8$ events and 0.2 and 1.0 Hz for $M \geq 2.8$ events. The data are subsequently resampled at 0.1 s.

Synthetic Green's functions for the inversion are computed using a 1-D velocity model, derived from a 3-D velocity model for the Northwest Geysers developed by Julian et al. (1996). This model was shown to perform well for moment tensor inversion (i.e., Guilhem et al., 2014). The synthetic Green's functions, including near-, intermediate-, and far-field terms for body and surfaces waves, are computed using Computer Programs in Seismology, Herrmann (2013). Our analysis is restrained to event depths reported in the DOE Geysers EGS catalog or when necessary the NCSS catalog.

Seismic moment tensors are computed utilizing the methods described in Minson and Dreger (2008), Ford et al. (2010) and Boyd et al., (2015). Part of this analysis requires the alignment of the observed waveforms to the computed Green's functions. With a well calibrated

velocity model it is sometimes possible to invert the waveform data without timing shifts, however in our analysis of these data time shifting is necessary and represents departures from the assumed velocity model with the actual velocity structure along the paths. Typically, the time shifts are estimated by trial and error, however due to the large numbers of events investigated we employed a grid search to find the best time alignment shifts automatically. The results of the time shift analysis are presented below.

An effort was made to have as many stations in common as possible for all of the studied events. Initially seismic data from as many as 10 stations within 6 km of the studied events were considered for preliminary moment tensor analysis. Depending on these initial fits of the observed data with the synthetic Green's functions, 5-6 stations were then selected for moment tensor processing using a grid-search algorithm to automatically find the optimal alignment of the observed data with the synthetic Green's functions. This method is applied to all studied events for automated moment tensor computation. The results are then checked and if necessary minor adjustments are applied to shift the data for optimal fit. In the final processing stage, data with poor fits are removed.

The alignment results are presented as histograms in Figure 3.1, which shows the alignment parameter, zcor, for a subset of all studied events (Figure 3.1a), for 56 events during the initial stimulation phase (Figure 3.1b) and for 26 events following the initial stimulation phase (Figure 3.1c) for all stations used in each of the inversions. In these plots zero indicates zero shift and the consistency of the data with the theoretical arrival time with respect to the velocity model that has been employed to compute the synthetic Green's functions. The results indicate a systematic shift to negative zcor values with the mean at approximately -3 samples or -0.3 seconds. This indicates that the data need to be shifted to a later time indicating that the model is slower on average than the actual Earth structure. The mean shift value does not appear to change from initial stimulation to post-stimulation periods. The plots indicate that the zcor search space in the automatic grid search approach can be tailored for better efficiency. The magnitude of the shifts on average are approximately 1/3 of the central period of the utilized passband.

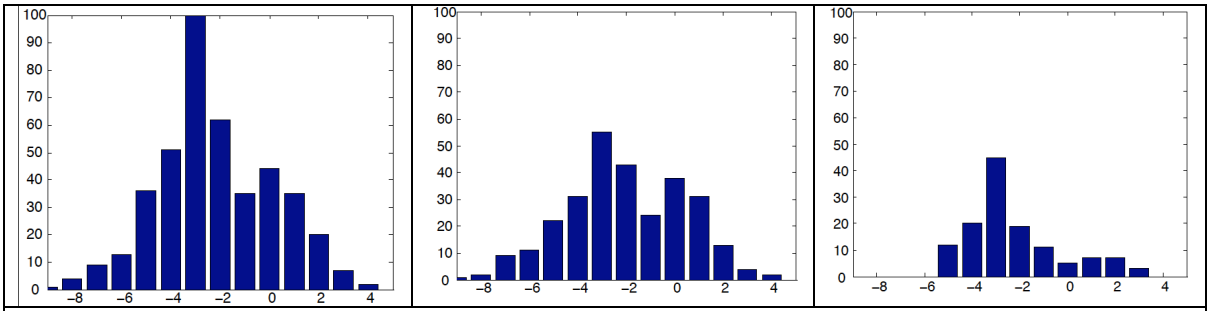

Figure 3.1: a) Distribution of alignment parameter, zcor for all studied events; **b)** 56 events during the initial injection phase; and **c)** 26 events following the initial injection phase. The units are samples. The time shift in seconds is found by multiplying by the sample interval of 0.1 seconds/sample.

3.2 Case Study of Selected Seismic Events

Selected events show examples of our moment tensor processing methodology. The first example Mw 1.91 March 27, 2012 occurs during injection with a rate of ~680 gallons per minute (gpm). The second event Mw 2.4 January 6, 2012 occurs during injection at a rate of ~1000 gpm and gives us the opportunity to compare our results with those from investigations by Guilhem et al., (2014) and Johnson (2014a). Our third example Mw 3.87 January 21, 2014 is the largest magnitude event thus far in the EGS Demonstration study area and occurs during injection at a rate of ~400 gpm.

Waveform fits and P-wave radiation patterns of the deviatoric moment tensor for event Mw 1.91 on March 27, 2012 (a) and full solution (b) are shown in Figure 3.2. The deviatoric moment tensor solution has a large 81% CLVD component and the full moment tensor solution has a somewhat large 35% isotropic component. The improvement in fit from the extra degree of freedom in the full moment tensor solution is 2% and not statistically significant as determined by the F-test. The F-test level of significance is only 74%.

In this example, we use the source-type inversion methodology of Nayak and Dreger (2015) shown in Figures 3.3a-c to explore the source-type-specific space of various datasets including first motion (Figure 3.3a), waveform (Figure 3.3b), and combined first-motion and waveform data (Figure 3.3c) and find that the best-fit region varies depending on the dataset. The first-motions are inconsistent with the large CLVD mechanisms of the deviatoric solution, and the combination of waveforms and first-motions appears to require a small volume increase component in which the best-fit solutions are essentially dipoles with a volume-increase component. The combined first-motion and waveform data full moment tensor inversion results in a decomposition of 15% DC, 59% CLVD, and 26% isotropic components. The interpretation for this normal event is that its full moment tensor mechanism is largely a CLVD with a considerable positive volumetric component. For the purpose of the subsequent stress inversion, however, the deviatoric waveform solution presented in Figure 3.2a is used. It is noted that the double-couple component, used in the stress inversion, is the same for the deviatoric, full moment tensor, and the combined waveform and first-motion moment tensor solutions.

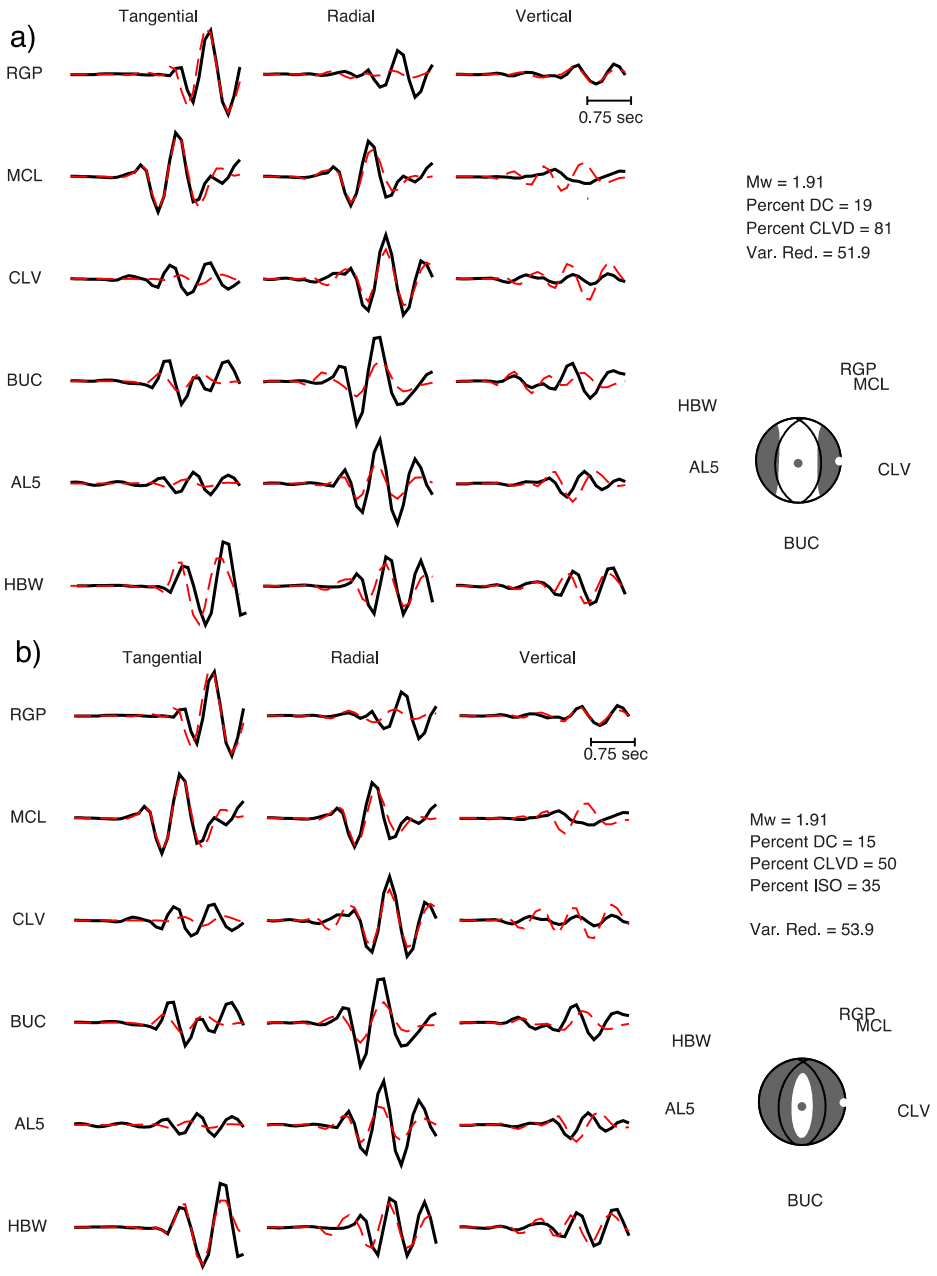

Figure 3.2: Comparison of filtered (0.7 to 1.7 Hz) observed velocity data (black) and synthetics (red) waveform fits and P-wave radiation pattern of the deviatoric moment tensor solution **a)** and full moment tensor solution **b)** for event Mw 1.91 on March 27, 2012. The improvement in fit of the full moment tensor solution is 2% and is too small to be significant.

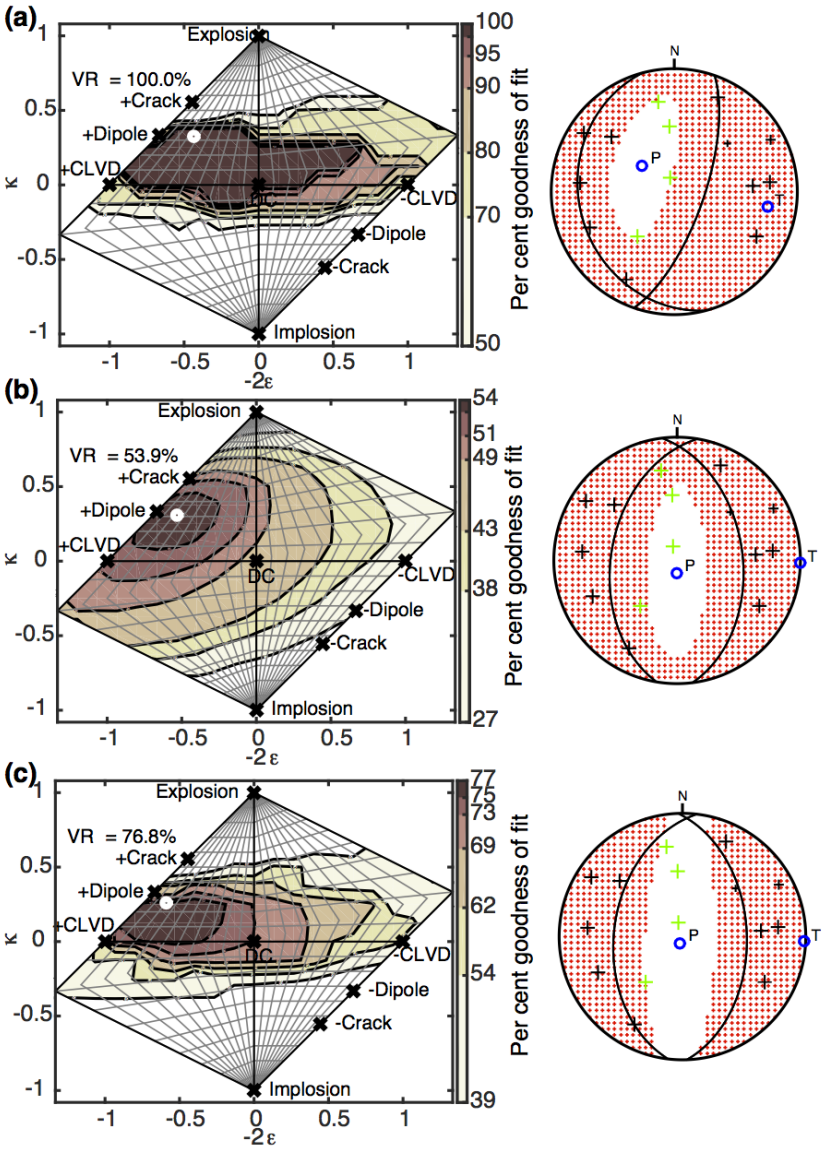

Figure 3.3: Network Sensitivity Solutions (NSS) of **a)** first motion **b)** waveform and **c)** combined first motion and waveform data using methodology of Nayak and Dreger (2015) for Mw 1.91 March 27, 2012 event. The best-fit solution for each dataset is marked with the white circle on the source-type plots. Variability in source-type is evident amongst the various datasets. Corresponding best-fit NSS focal mechanisms are shown to the right. First-motion polarity data is plotted with plus symbols, up first motions (black), down first motions (green).

The Mw 2.4 earthquake on January 6, 2012 occurs during Prati-32 injection at a rate of ~1000 gpm and is included in the catalogs of Johnson (2014a) and Guilhem et al. (2014) and provides a unique opportunity to compare moment tensor solutions using various methodologies. Waveform fits and P-wave radiation patterns of the deviatoric moment tensor are presented in Figure 3.4a while the full solution from this study is shown in Figure 3.4b. The deviatoric

moment tensor solution has a large 80% DC component and the full moment tensor solution has a somewhat large 37% isotropic component. The improvement in fit from the extra degree of freedom in the full moment tensor solution is 2% and not statistically significant as determined by the F-test. The F-test level of significance is only 74%.

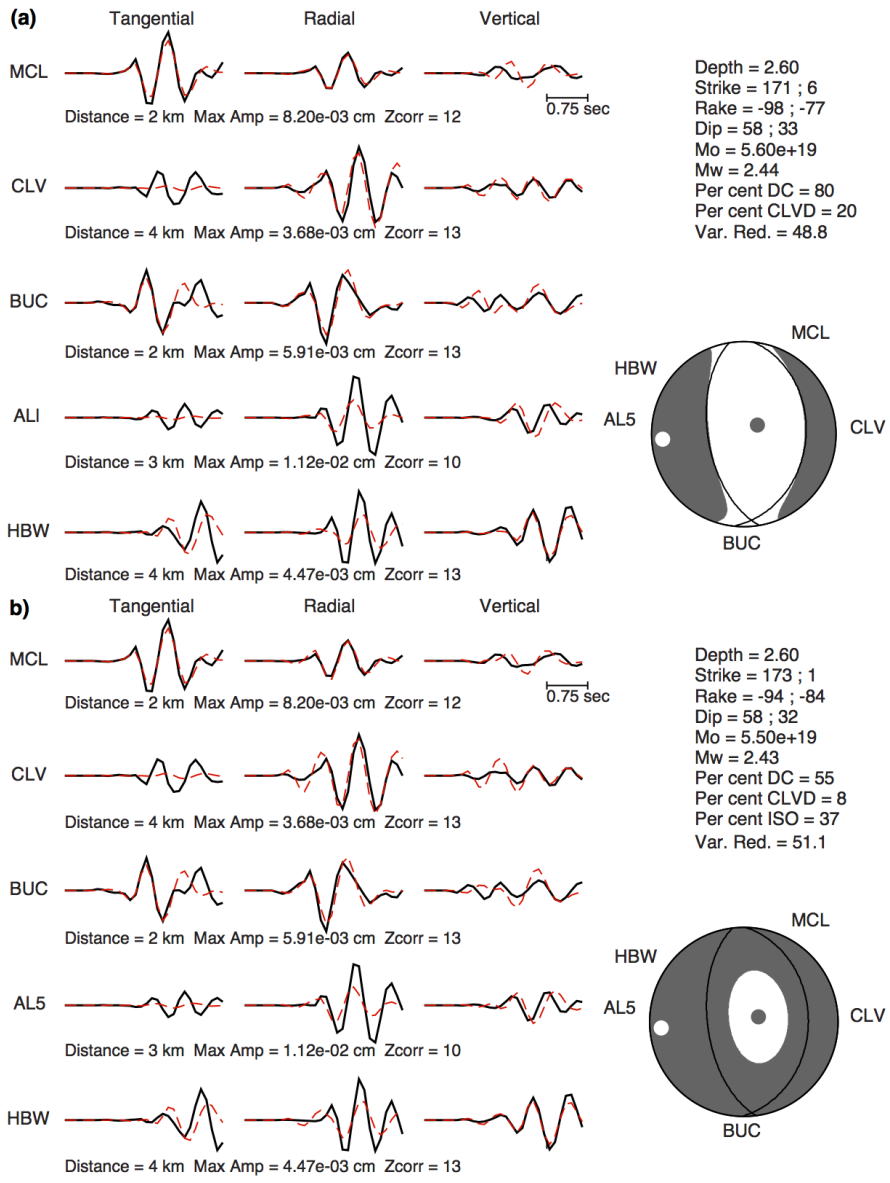

Figure 3.4: Comparison of filtered (0.7 to 1.7 Hz) observed velocity data (black) and synthetics (red) waveform fits and P-wave radiation pattern of the deviatoric moment tensor solution **a)** and full moment tensor solution **b)** for the Mw 2.4 January 6, 2012 event. The improvement in fit of the full moment tensor solution is 2.3% and is too small to be statistically significant as measured by the F-test. The F-test level of significance is only 74%.

Guilhem et al. (2014) and this study use the same time-domain moment tensor inversion TDMT_INV (Dreger, 2003) methodology and velocity model while Johnson (2014b) uses a frequency-domain approach and one-dimensional velocity model developed by O'Connell and Johnson (1991). Takeoff angles of first-motion polarity data in Guilhem et al. (2014) are calculated using yearly-updated 3D velocity models and earthquake locations obtained from inversions using SimulPS (Thurber, 1983). Consistency in the focal mechanisms is evident, however the small differences in focal mechanisms from this study and Guilhem et al. (2014), Figures 3.5c and 3.5d, respectively, may be due to differences in seismic waveform data, Green's functions, and event location used in the moment tensor inversion.

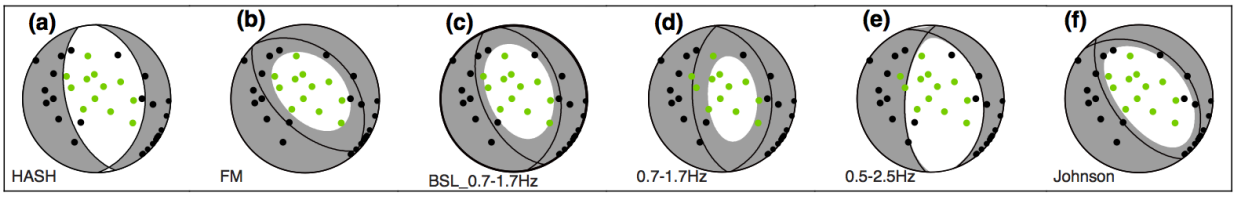

Figure 3.5: Focal mechanisms of the January 6, 2012 event from multiple studies. Figure adapted from Guilhem et al. (2014). Focal mechanisms determined from left to right as follows: **a)** Guilhem et al. (2014) using HASH (Hardebeck and Shearer (2002). **b)** Guilhem et al. (2014) NSS best-fit solution using first motion data. **c)** Full moment tensor using 0.7 – 1.7 Hz filtered data, this study. **d)** Full moment tensor solution using 0.7 – 1.7 Hz filtered data, (Guilhem et al. (2014). **e)** Full moment tensor solution using 0.5 – 2.5 Hz filtered data, (Guilhem et al. (2014). **f)** Static time domain moment tensor solution from Johnson (2014a). First-motion polarity data from Guilhem et al. (2014) plotted with dots, up first motions (black) and down first motions (green).

Figures 3.6a-c explore the source-type-specific space of various datasets including a) first motion b) waveform and c) combined first-motion and waveform data and find that the best-fit region varies depending on the dataset. The first-motions are somewhat inconsistent with the large DC mechanisms of the deviatoric solution, and the combination of waveforms and first-motions appears to require a volume increase component in which the best-fit solutions are essentially double-couples with a volume-increase component. The combined first-motion and waveform data full moment tensor inversion results in a decomposition of 75% DC, 3% CLVD, and 22% isotropic components. The interpretation for this normal event is that its full moment tensor mechanism is largely a DC with a considerable positive volumetric component. For the purpose of the subsequent stress inversion, however, the deviatoric waveform solution presented in Figure 3.4a is used. It is noted that the double-couple component, used in the stress inversion, is similar for the deviatoric, full moment tensor, and the combined waveform and first-motion moment tensor solutions.

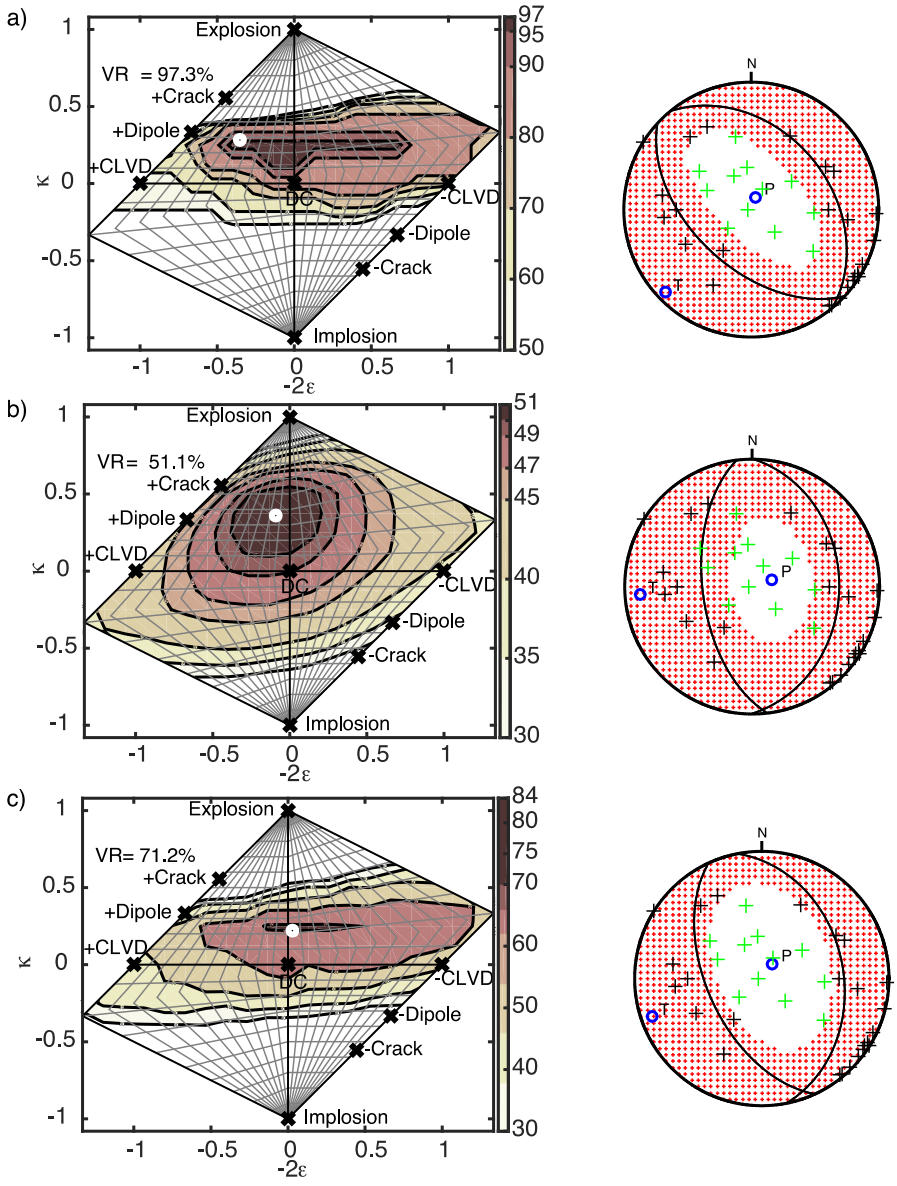

Figure 3.6: Network Sensitivity Solutions (NSS) of **a)** first motion **b)** waveform and **c)** combined first motion and waveform data using methodology of Nayak and Dreger (2015) for Mw 2.44 January 6, 2012 event. The best-fit solution for each dataset is marked with the white circle on the source-type plots. Variability in source-type is evident amongst the various datasets. Corresponding best-fit NSS focal mechanisms are shown to the right. First-motion polarity data is plotted with plus symbols, up first motions (black), down first motions (green).

More than two years after the start of injection, the maximum magnitude event thus far, Mw 3.87 January 21, 2014, occurs in the center of the study area at a catalog depth of 1.7 km following an extended shut-in period when the Prati-32 injection rate is ~400 gpm. The moment tensor solutions in Figure 3.7 are computed using broadband data from regional stations in the

Berkeley Digital Seismic Network (BDSN). The broadband velocity data from stations located at distances from 55 to 68 km are instrument corrected with reported pole-zero response functions, integrated to displacement, and filtered with an acausal, four-pole, Butterworth band-pass filter with a 0.02 - 0.10 Hz passband. Green's functions are computed using the GIL7 velocity model derived from broadband waveform modeling and routinely used by the Berkeley Seismological Laboratory (BSL) to monitor California seismicity (Stidham et al., 1999). The Green's functions are computed with FKRPROG written by Chandan Saikia (Saikia, 1994) and based on the method of Wang and Herrmann (1980). Waveform fits and P-wave radiation patterns of the deviatoric moment tensor (a) and full solution (b) computed at a depth of 3.5 km are shown in Figure 3.7. The deviatoric moment tensor solution has a large 73% DC component and the full moment tensor solution has a small 3% isotropic component. The improvement in fit from the extra degree of freedom in the full moment tensor solution is 0.1% and not statistically significant as determined by the F-test.

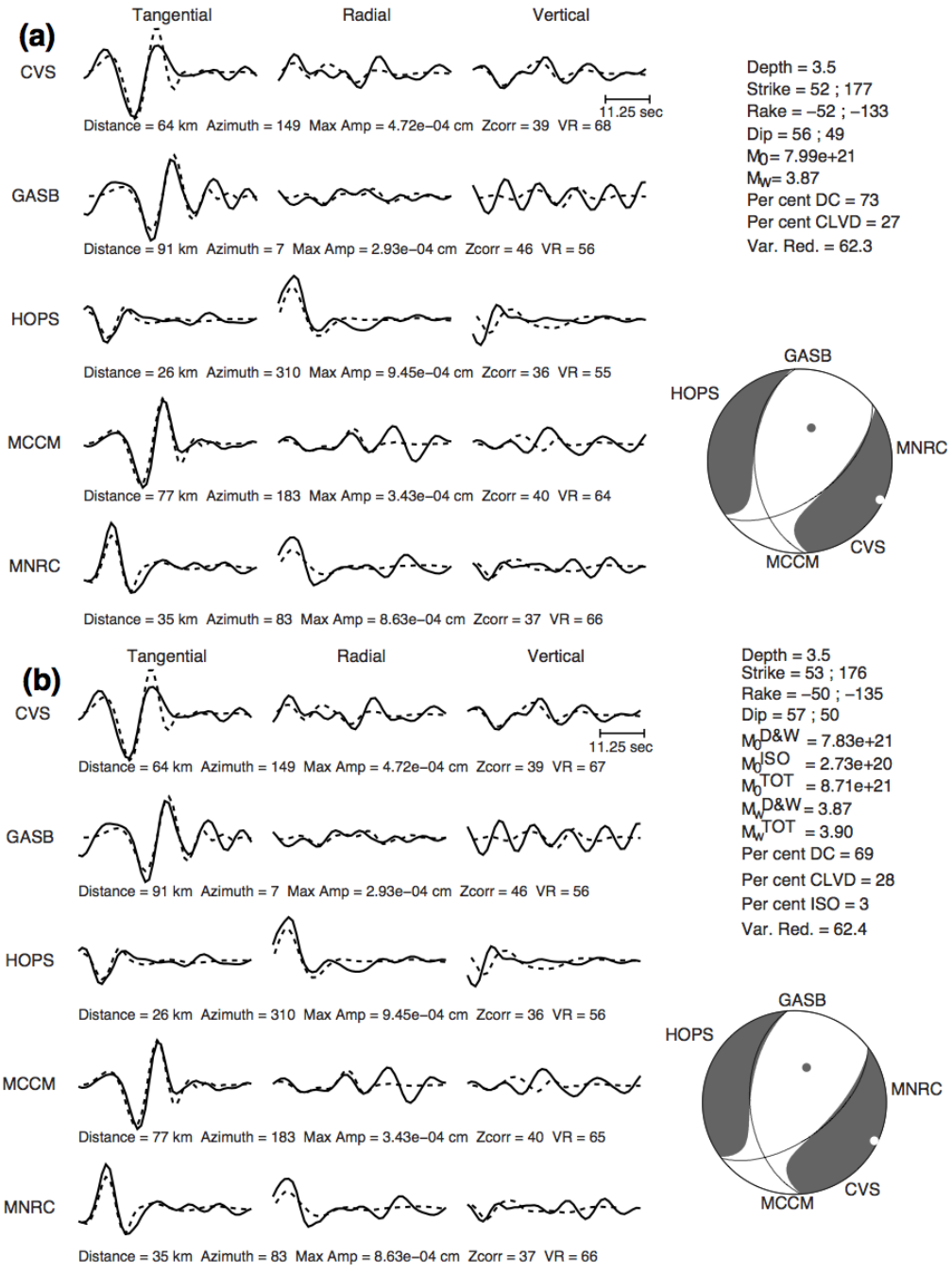

Figure 3.7: Comparison of filtered (0.02-0.10 Hz) observed displacement data (solid) and synthetics (dashed) waveform fits and P-wave radiation pattern of the deviatoric moment tensor solution **a)** and full moment tensor solution **b)** for the Mw 3.87 January 21, 2014 event. The improvement in fit of the full moment tensor solution is 0.1% and is too small to be statistically significant as measured by the F-test.

3.3 Temporal Trends of Source Physics Parameters

Figure 3.8 shows a time line of the deviatoric moment tensors plotted against the Prati-32 injection rate. Increasing percentage of the compensated linear vector dipole (CLVD) component is indicated with colors transitioning from cool (blue) to warm (red). The size of the focal mechanisms scale with computed moment magnitude. The isotropic component of the full moment tensor solutions is plotted with plus symbols to give a sense of its percentage range. The median of the percent isotropic component (thin black line) is plotted to investigate whether volume-increase or volume-decrease source processes correlate with injection rate.

While focal mechanisms are consistent with the tensile stress direction inferred from previous studies (Ross et al., 1996, 1999; Guilhem et al., 2014; Boyd et al., 2015), there are interesting patterns observed with this 167-event catalog of Mw > 0.6 events. Moment tensors of pre-injection events have a greater percent double-couple (DC) component indicated by the cooler colors. Similarly, the three largest magnitude events have a higher percentage DC component. Larger magnitude events are more frequent during injection. Strike-slip events are most common prior to and during the initial injection phase with a gradual transition to more normal faulting mechanisms as injection progresses. Bursts of increased earthquake rate occur from August 2-3, 2011 with 5 events. The most notable burst with 12 events during a three-day interval occurs from January 30 - February 1, 2013 when injection resumes after an extended shut-in period lasting 160 days. These events exhibit similar strike-slip faulting mechanisms with higher percentages ~40% CLVD component indicated by shades of green. Even though the statistical significance of the isotropic component (plus symbols) of the full moment tensor solutions is unresolved in this study, the percent isotropic median line is observed to be positive prior to injection, positive and negative during maximum injection rates, positive during lower injection rates, and negative when injection ceases. The deviatoric focal mechanisms shown in Figure 3.8 will be used in the stress analysis presented in section 8.

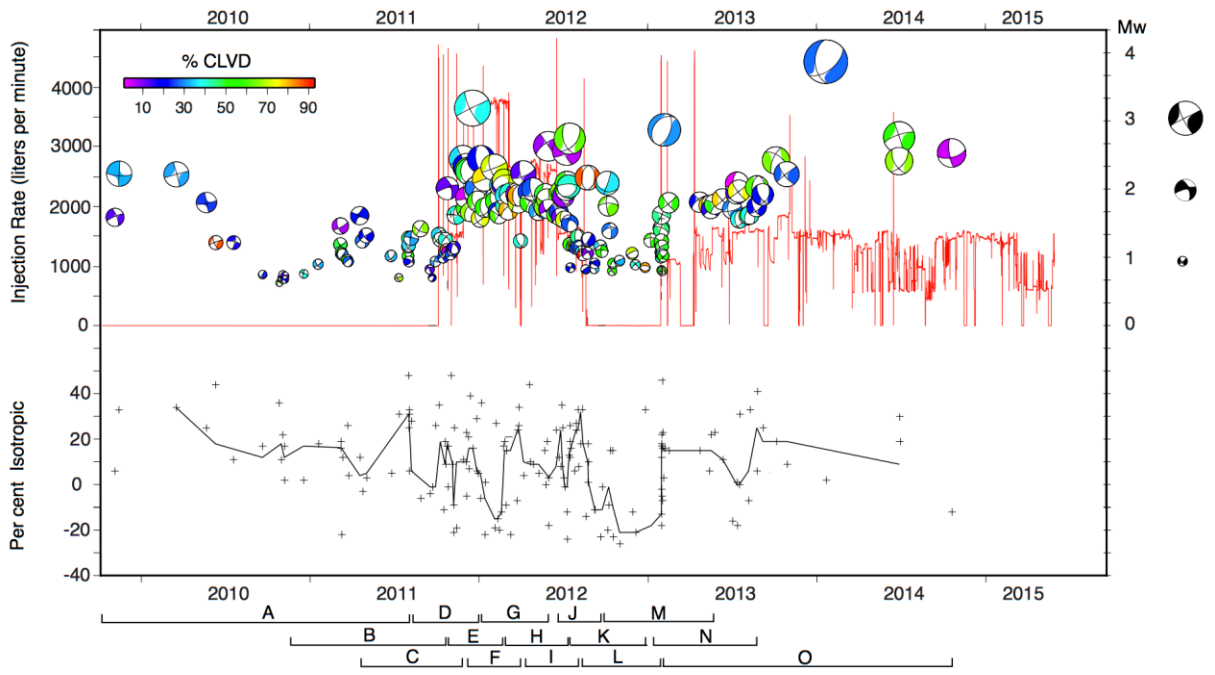

Figure 3.8: Time history of P-32 injection rate (red line) and deviatoric focal mechanisms shaded by percent compensated linear vector dipole (CLVD) component. Injection rate in gallons per minute (gpm) is shown on the left vertical axis. Focal mechanism size is scaled by computed moment magnitude, Mw. The percent isotropic component of corresponding full moment tensor solutions is marked with plus symbols. The median of the percent isotropic component is delineated with the thin black line. Moment magnitude, Mw, and percent isotropic scales are shown on the right vertical axis. Fifteen overlapping time windows for inversion of deviatoric focal mechanisms are labeled A – O below the horizontal time axis. No injection data available after May 30, 2015.

3.4 Depth Distribution of Fault Mechanisms

To distinguish the faulting mechanism, we follow the approach based on rake angle as in Yang et al. (2012). The depth range of Prati-32 injection into the high temperature reservoir is from 2.6 - 3.4 km depth. Depths of the studied events range from 0.7 - 5.5 km with most between depths of 1.5 - 3.5 km. The most common faulting style is strike-slip (69%), followed by normal (27%), with 3% thrust fault events (Figure 3.9). The strike-slip events are observed to occur at all depths, whereas the majority of normal and reverse events tend to occur above and within the reservoir. There is an increase in normal fault mechanisms from 2.4 - 2.7 km while most strike-slip mechanisms occur at depths from 2.4 - 3.3 km.

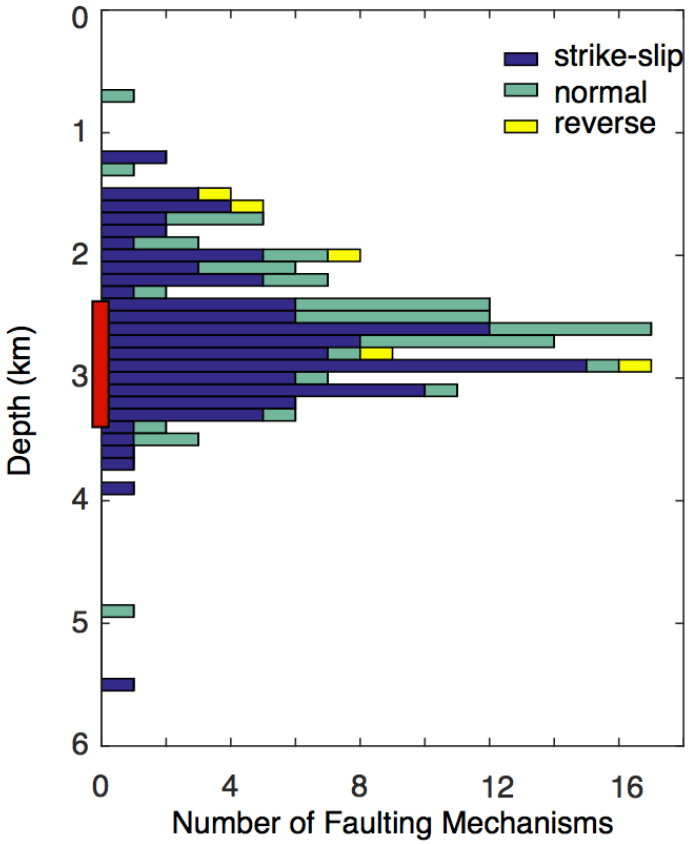

Figure 3.9: Histogram plot of faulting mechanism and depth. Strike-slip mechanisms (blue) account for 69% of the fault mechanisms, followed by 28% normal mechanisms (green), and 3% reverse mechanisms (yellow). The red bar indicates the open-hole portion of injection well Prati-32 from ~2500-3400 m. depth.

3.5 Summary

The results from the moment tensor analysis indicate that seismicity in the vicinity of The Geysers EGS demonstration area evolves in space and time as water injection operations progress. Most of the events are likely the result of shear failure due to both tectonic shear stress and tensile stress induced by the injection of water. Even though the moment tensor catalog is limited to 167 events with MW > 0.6, patterns in earthquake source parameters emerge before and during multiple stages of injection and shut-in. Moment tensors of pre-injection events have a greater per cent DC component indicated by the cooler colors in Fig. 3.8. Similarly, the three largest magnitude events have a higher percentage DC component. Larger magnitude events are more frequent during periods of injection. Strike-slip events are most common prior to and during the initial injection phase with a gradual transition to more normal faulting mechanisms as injection progresses (Boyd et al., 2018).

4.0 Seismic Broadband Data Processing

The objective of this task was to analyze the seismic broadband data throughout The Geysers geothermal reservoir and in the vicinity of the Prati-32 EGS demonstration well that have been collected from summer 2012 to summer 2013 at The Geysers with funding from the European GEISER project. These data have not been used yet and will be leveraged to enhance the outcome and results of the current DOE project. The outcome of this task will be event hypocenter locations, origin times, and moment magnitudes suitable for the analysis of source parameters, stress orientation and stress magnitude, estimation of fracture density, and estimation of Vp/Vs-ratio for fluid monitoring.

The seismic data were recorded by 33 broadband stations resulting in a total data volume of approximately 1 TB. Of the 33 stations, 27 were deployed within the boundaries of The Geysers steam field, while seven stations were located in a circle surrounding the reservoir at distances of up to 80 km (Figure 4.1).

a)

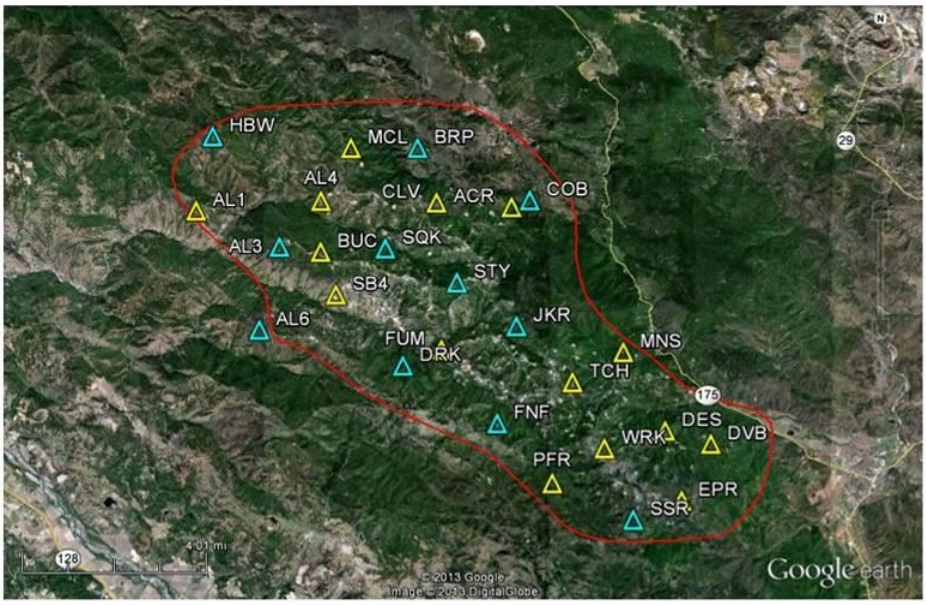

b)

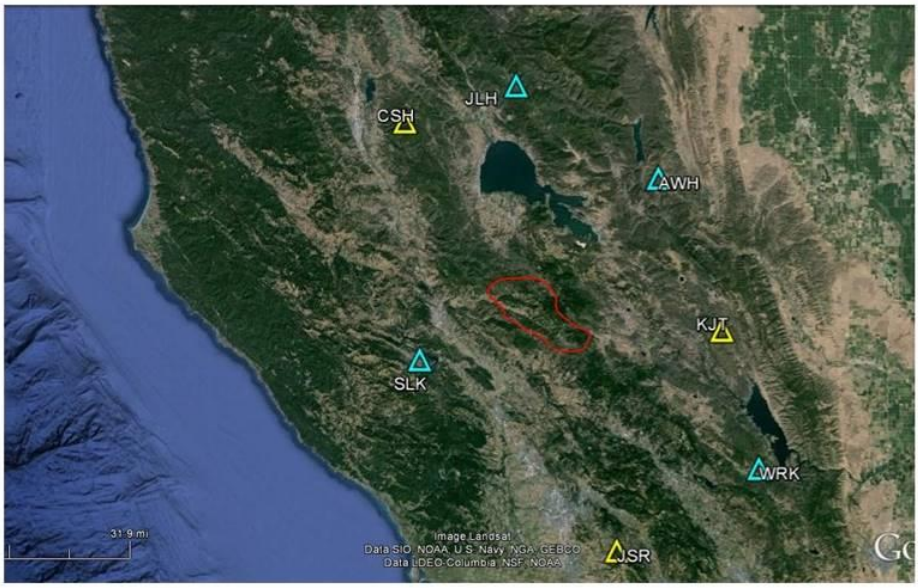

Figure 4.1: a) Location of broadband seismometers inside The Geysers geothermal reservoir (yellow triangles: Guralp CMG sensor, cyan triangles: Trillium Compact sensor). **b)** Location of Location of broadband seismometers outside The Geysers geothermal reservoir.

4.1 Data Processing

The first task was concerned with the preparation of the software programs for processing the continuous broadband data, which was based on LBNL's REMAS (Rapid Earthquake Monitoring and Assessment System) software. The continuous one-hour long Mini-SEED data files were processed through an event detector (STA/LTA) to identify possible events at each station. Upon the completion of the detection step the individual station detections were associated in time to identify possible events for multiple stations. The possible network events were then further processed to produce an earthquake catalog. This processing includes picking of P- and S-wave arrival times and preliminary location of the earthquake locations. The geometry of the earthquake and stations locations was subsequently utilized to rotate the station components and to maximize the shear wave amplitudes on the horizontal components. After rotation, a second pass of the STA/LTA event detector was performed to improve the shear (SH) wave arrival times. Once the improved phase picks were obtained, the program simulPS was utilized to obtain improved earthquake locations, while moment magnitude calculation were performed on the recorded waveforms. The final results included an earthquake catalog and the creation of input files for further analysis.

4.1.1 Initial Processing Test

Optimization of the parameters of the processing procedure is essential to generate an exhaustive earthquake catalog. An 18-day time period was processed initially to test and fine-tune the processing software. The resulting event catalog from the broadband data was compared to the catalog from the existing LBL Geysers geophone network, as shown in Figures 4.2 and 3.3. Note that at this stage in the data processing the magnitude calibration for the broadband data had not been fully determined, so the magnitudes in Figure 4.2 are larger than they should be. The initial test of the broadband data returned over 2,220 events for this 18-day period. Therefore, it was expected that processing the complete broadband data over the one-year recording period would yield approximately 46,000 events.

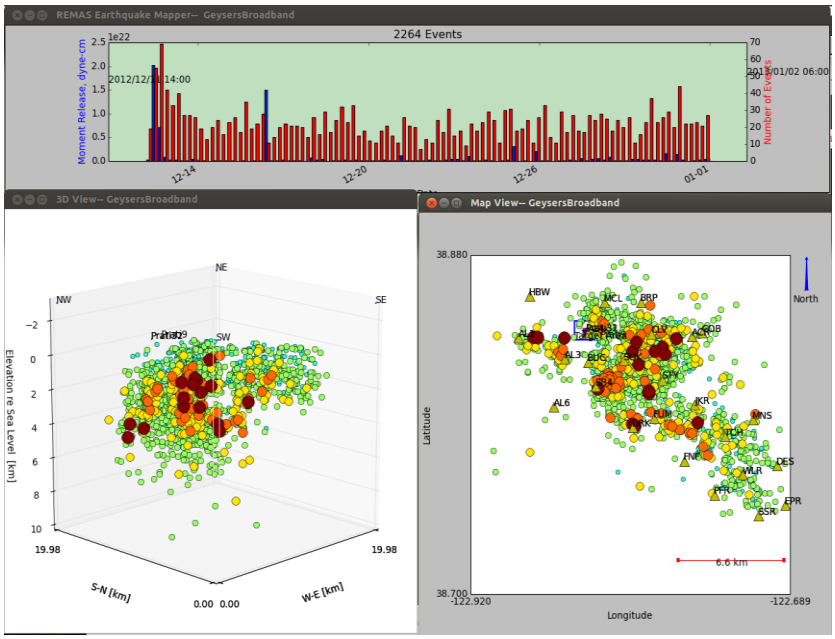

Figure 4.2: Events detected by The Geysers broadband network, Dec 13-31, 2012.

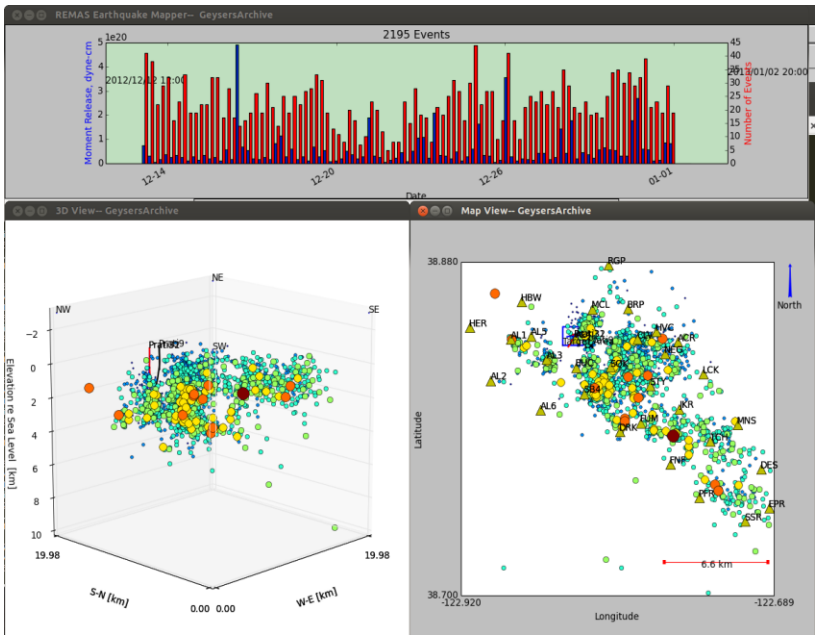

Figure 4.3: Events detected by the LBL Geysers geophone network, Dec 13-31, 2012.

4.1.2 Final Processing Results

The final processing of the continuous broadband data generated an earthquake catalog with approximately 65,000 events, which surpassed the initial estimate by 43%. A subset with high- quality event locations including maximum RMS travel time residuals of 0.2 s and a minimum of 8 phase picks per event yielded 37,300 earthquakes throughout the reservoir. This number compares to 24,300 events with the same quality standard recorded by the LBNL geophone network over the same time period. Thus, the broadband network detected about 53% more events than the geophone network, which resulted from the higher sensitivity level of the broadband seismometers compared to the geophones. The distribution of the high-quality event locations detected by the broadband and geophone network is presented, respectively, in Figures 4.4a and 4.4b. A comparison shows that the region of seismicity is the same, but there are more events recorded by the broadband network that have filled in some of the gaps that are visible in the geophone data. These events are likely lower magnitude events, as shown in the next section.

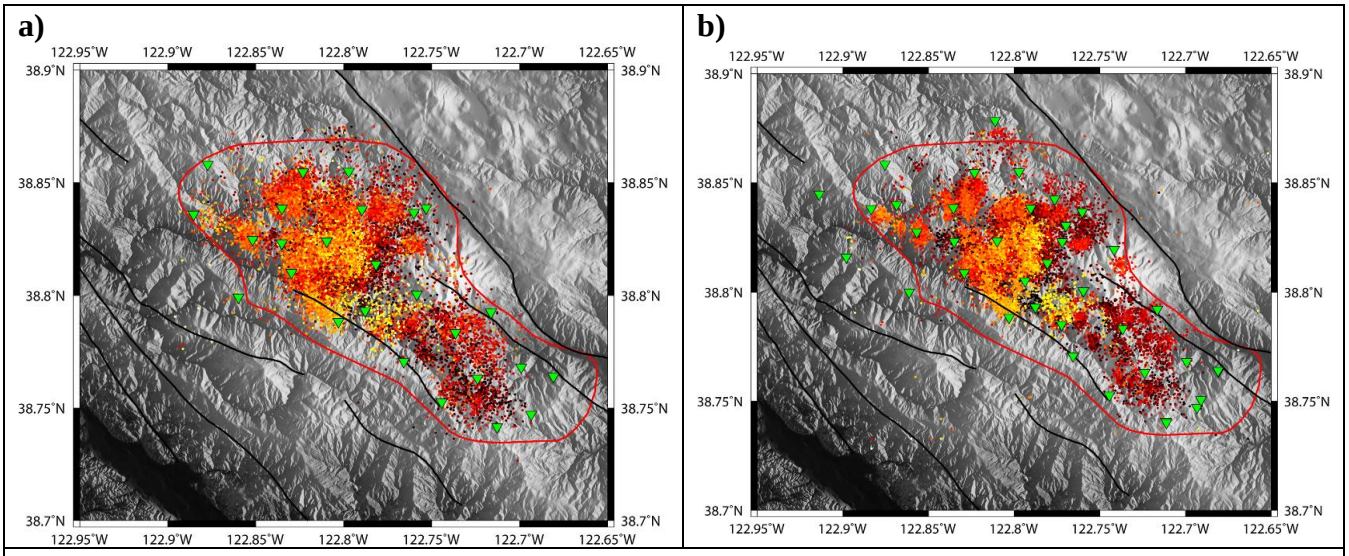

Figure 4.4: a) High-quality events detected by The Geysers broadband network July 2012 – July 2013. **b)** High-quality events detected by the LBNL Geysers geophone network July 2012 – July 2013.

The distribution of events, in the region of interest around Prati-32 recorded by the broadband network and by the LBNL geophone network, is presented in Figures 4.5a and 4.5b, respectively. Due to the hiatus of water injection from August 20, 2012 – January 29, 2013 and from March 12, 2013 to April 9, 2013 (Figure 3.8), the number of events detected in the study area is reduced relative to periods with normal water injection rates. The number of high-quality events recorded by the broadband and by the geophone networks are 648 and 449, respectively. This confirms the reservoir-wide observation that the broadband seismometers have a higher sensitivity level than the geophones and detected 44% more events in the study area.

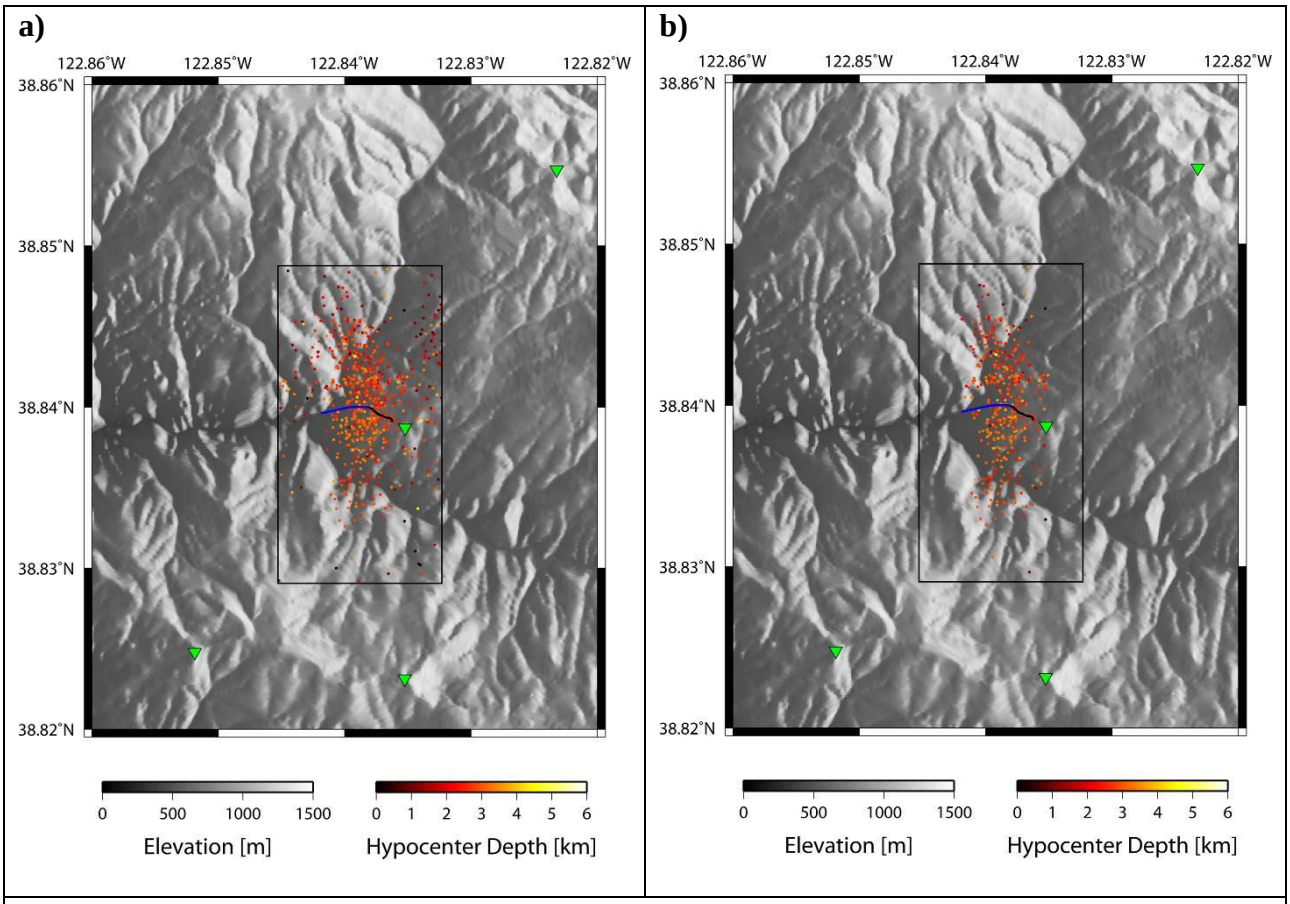

Figure 4.6: a) High-quality events detected by The Geysers broadband network July 2012 – July 2013 in the vicinity near the Prati-32 injection site. **b)** High-quality events detected by the LBNL Geysers geophone network July 2012 – July 2013 in the vicinity near the Prati-32 injection site.

The distribution of the same events in east-west cross section through the study area is presented in Figures 4.7a and 4.7b. Most of the events are located below the injection interval, which coincides with previous observations. During the early injection phase (late 2011), most seismicity was located directly above or below the injection interval of Prati-32. However, with continuing injection activities, the hypocenters of the events migrated to greater depths below the injection interval. This trend is confirmed by the event locations in Figures 4.7.

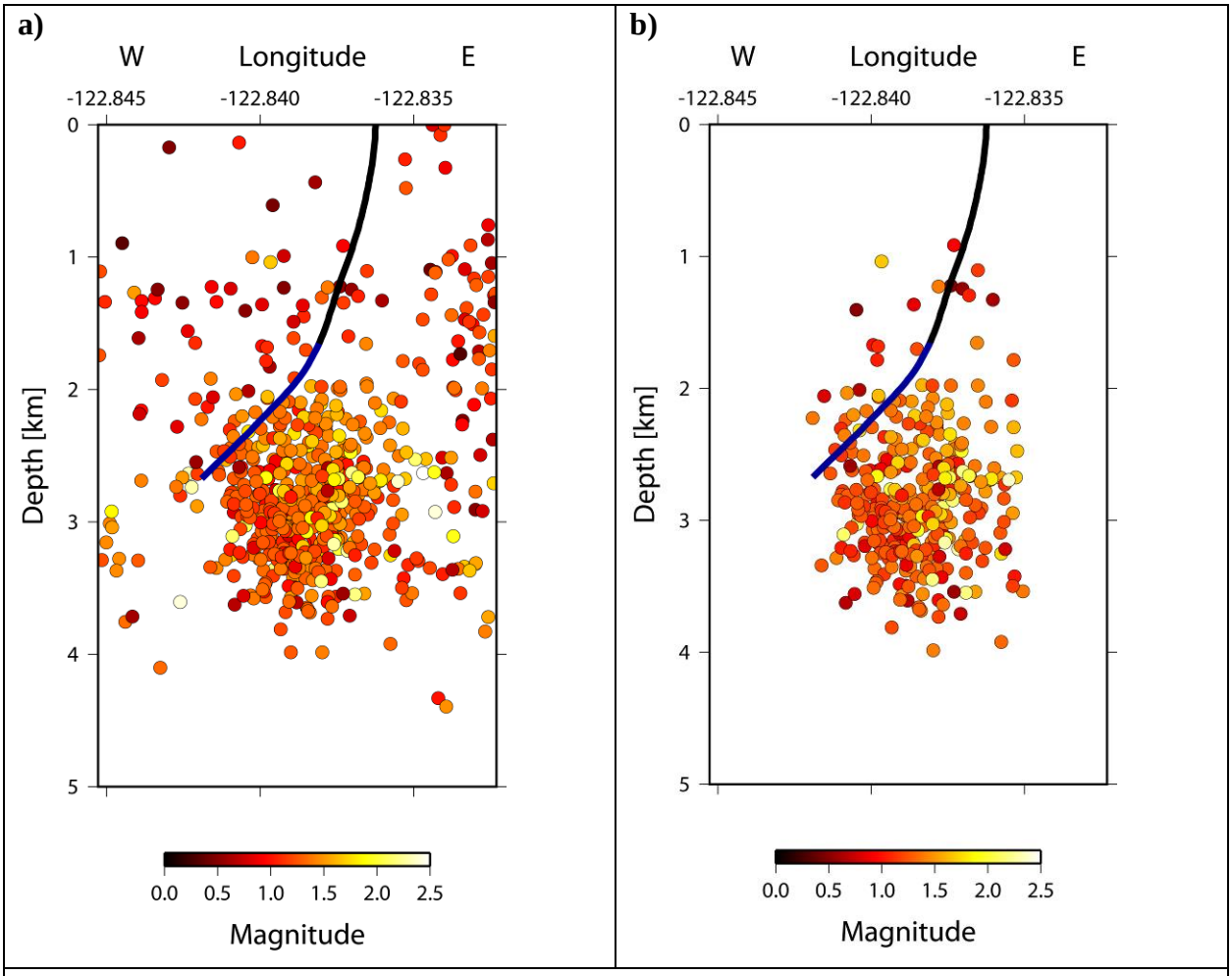

Figure 4.7: a) High-quality events detected by The Geysers broadband network July 2012 – July 2013 near the Prati-32 injection site. The well trajectory is given by the curved line. The blue section is the water injection interval. **b)** High-quality events detected by the LBNL Geysers geophone network July 2012 – July 2013 near the Prati-32 injection site. The well trajectory is given by the curved line. The blue section is the water injection interval.

4.2 Earthquake-Magnitude-Frequency Relationship (Gutenberg-Richter Law)

The Gutenberg–Richter law (Gutenberg and Richter, 1956) expresses the relationship between the magnitude and total number of earthquakes in any given region and time period of at least that magnitude. It is expressed as:

$$log_{10} N = a - b M \quad (4.1)$$

where N is the number of earthquakes of magnitude M or larger and a and b are constant. When the relationship in equation (1) is plotted, the frequency of N typically increases 10-fold for each

decrease of one magnitude unit *M*. The relationship between event magnitude and frequency of occurrence is remarkably common, although the values of *a* and *b* may vary from region to region or over time. In seismically active regions, the parameter *b*, which is referred to as the *b-value*, is commonly close to 1.0. This means that for a given frequency of a magnitude M 3.0 event there will be 10 times as many magnitude 2.0 events and 100 times as many magnitude 1.0 events. Variation of *b-values* in the approximate range of 0.5 to 2 have been observe depending on the tectonic environment of the region. In general, a high *b-value* indicates a very high proportion of small earthquakes to large ones. An example of the occurrence of high *b-values* are geothermal areas, where the injection of cold water into hot rock induces high numbers of small-magnitude events.

The Gutenberg-Richter relationship of the reservoir-wide seismicity shown in Figures 4.4 is presented in Figure 4.8. The two datasets show a slightly different distribution of observed magnitudes. While the broadband data show a more skewed distribution with the maximum number of events observed at magnitude 1.0, the geophone data reveal a more symmetric distribution with the maximum number of events observed at magnitude 1.2. Accordingly, the *b-value* for the broadband- relative to the geophone data is higher at *b*=1.14 compared to *b*=1.08, respectively. The higher *b-value* for the seismicity recorded by the broadband network is another indicator, that the broadband seismometers have a higher sensitivity than the geophone sensors, which results in the recording of more low-magnitude events.

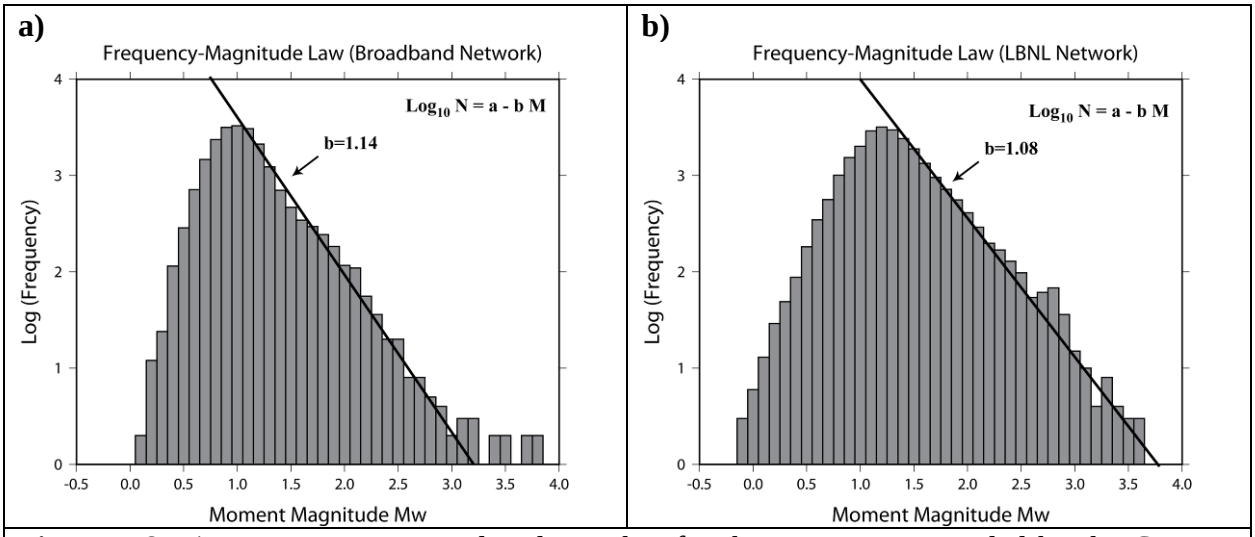

Figure 4.8: a) Frequency-magnitude relationship for the seismicity recorded by the Geysers broadband network from 2012-2013. **b)** Frequency-magnitude relationship for the seismicity recorded by the LBNL Geysers geophone network from 2012-2013.

The magnitude-frequency relationships for the broadband and geophone network data recorded in the study area near Prati-32 are presented in Figure 4.9a and 4.9b, respectively. In general, the associated magnitudes are lower than for the data displayed in Figure 4.8. The events in the study area are primarily induced by the water injection in Prati-32, which generates seismicity of lower magnitudes when compared to the reservoir-wide data that also contain

tectonic events. The manifestation of this effect is reflected in the *b-values* of both datasets recorded in the Prati-32 study areas, which are higher than those in Figure 4.8. The comparison of the datasets in the Prati-32 study area shows that the *b-value* of the events recorded by the broadband network (*b*=1.60) is higher than that of the events recorded by the geophone network (*b*=1.45), indicating once more the higher sensitivity of the broadband seismometers over the geophone sensors. Furthermore, the relatively high *b-values* in Figure 4.9 are indicative of water-injection related events when compared to the magnitude-frequency relationships of tectonic events which typically show *b-values* around 1.0.

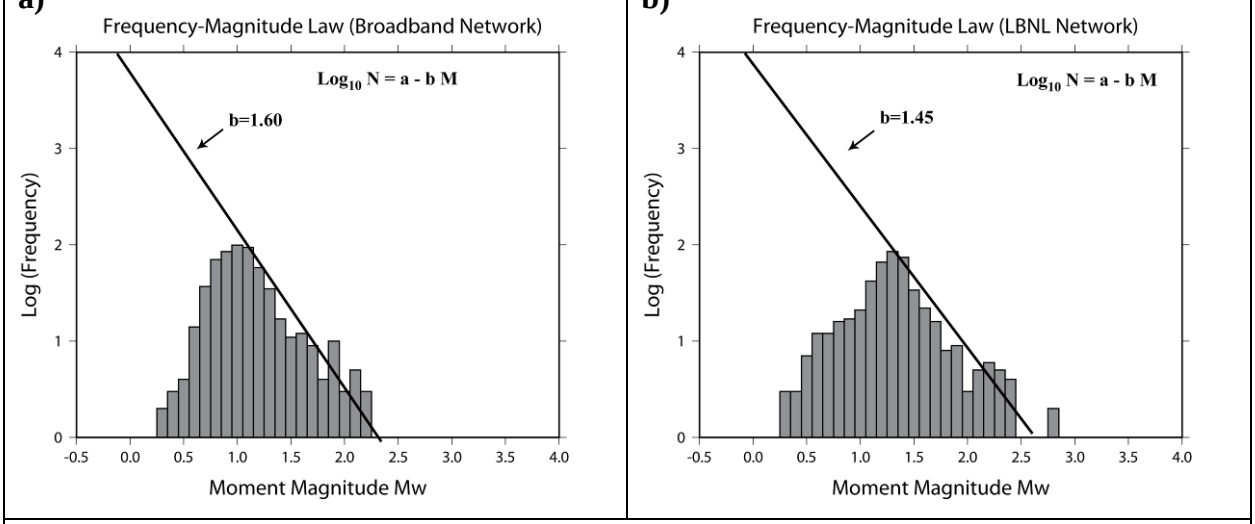

Figure 4.9: a) Frequency-magnitude relationship for the seismicity recorded by the Geysers broadband network from 2012-2013 near the Prati-32 injection site. **b)** Frequency-magnitude relationship for the seismicity recorded by the LBNL Geysers geophone network from 2012-2013 near the Prati-32 injection site.

4.3 Summary

This task has generated, for the first time, a seismic catalog from continuously recorded local broadband data at The Geysers geothermal reservoir. The results include a catalog of seismic events recorded from July 2012 to July 2013 during the Prati-32 EGS project. The data include event origin time, event location and event depth, P- and S-wave phase arrivals and moment magnitudes. These data will subsequently be used for the analysis of source parameters, stress orientation and magnitude, activated fracture-network volume, and estimation of Vp/Vs-ratio for fluid monitoring.

5.0 Scaling Relationships for Prati-32 Seismicity and 3D Fracture Network

Given a moment tensor solution, it is possible to test which of the two possible nodal (fault) planes is the causative plane. For small events related to the EGS stimulation project it is necessary to consider higher frequencies and therefore the use of theoretical Green's functions based on simple plane layered velocity models is not adequate. Therefore empirical Green's functions are derived, utilizing the waveforms of nearly collocated smaller events. Mori (1993) demonstrated that the waveform of a smaller earthquake could be spectrally deconvolved from the larger target earthquake yielding an estimate of the seismic moment rate function (MRF). Several MRF observed at different seismic stations can subsequently be inverted for fault slip, as well as to identify the causative rupture plane. Dreger et al. (2007) applied this approach at Parkfield, California, and found that it is possible to obtain finite-source parameters for micro-earthquakes exhibiting rupture complexity, and kinematic parameters that are comparable to their larger counterparts.

5.1 Seismic Moment Rate Function

For finite-source investigation it is necessary to find highly correlated pairs of events to determine the seismic moment rate function at a recording station using the method of waveform deconvolution of a small magnitude earthquake. Usually events need to be close in space on the order of 200 m and have similar faulting mechanisms to achieve sufficient correlation. Furthermore, a difference of at least one order magnitude is required to minimize the source contribution in the resulting waveform. The smaller-magnitude empirical Green's function (eGf) event is spectrally deconvolved from the larger-magnitude target event. The resulting spectrum is then inverse Fourier transformed yielding a pulse that is interpreted as the far-field source-time function (Mori, 1993). In the following, the principle of the seismic moment rate function is presented using the example of a Mw 2.47 event on August 25, 2013. Date, time, latitude, longitude, depth, and catalog magnitude of the target and selected eGf event are shown in Table 5.1.

Table 5.1: Catalog, date, time, latitude, longitude, depth and magnitude from DOE EGS LBNL catalog for selected target and eGf events.

	Catalog	**Date**	**Time**	**Latitude**	**Longitude**	**Depth**	**Magnitude**
Target	LBNL	2013/08/25	14:06:47.39	38.84297	-122.83650	2.10	Mw 2.47
eGf	LBNL	2013/09/14	11:40:40.15	38.84298	-122.83900	2.135	Mw 1.13

We investigated the moment tensor of the target event using data filtered in passband 0.7 – 1.7 Hz. Waveform data were downloaded from the NCEDC for stations in the LBNL Berkeley Geysers (BG) seismic network. We used event times and locations as specified in the DOE EGS LBNL catalog. To constrain the moment tensor, we used the source-type inversion methodology of Nayak and Dreger (2015) to explore the source-type-specific space of combined first-motion

and waveform data. The combined first-motion and waveform data full moment tensor inversion results in a decomposition of 41% double-couple (DC), 37% CLVD, and 22% ISO components, as presented in Figure 5.1, with a variance reduction (VR) of 63%. The interpretation for this oblique normal event is that its full moment tensor mechanism is composed of roughly equal parts DC-CLVD with a small negative volumetric component as shown in Table 5.2.

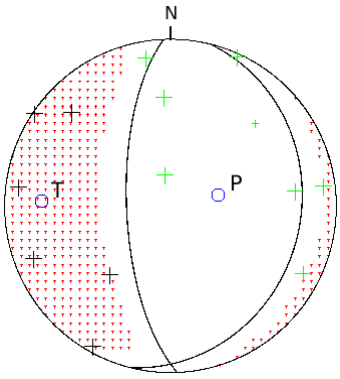

Figure 5.1: The constrained moment tensor solution uses first-motion polarity data plotted with plus symbols, up first motions (black), down first motions (green). The negative isotropic component evidenced by the lack of shading in the compressive quadrants indicates an implosive mechanism.

Table 5.2: Target event combined waveform and first motion full moment tensor parameters. Strike, rake and dip for both nodal planes.

Bowers Moment (dyne-cm)	Mw	Strike	Rake	Dip	%DC	%CLVD	%ISO
1.7E+19	2.09	14/178	-75/-96	22/68	41	37	22

The empirical Green's function approach assumes that the target and eGf pair are co-located events having a similar source mechanism with a difference in magnitude of at least one unit. Suitable eGf events horizontally located within 200 m from larger target events were found in the DOE EGS LBNL catalog. The eGf waveforms were then deconvolved from the target waveforms to identify those that produced pulse-like moment rate functions (MRF) with the highest signal to noise ratio. The pulse widths of the resulting MRFs range from 0.1075 s at station HBW in the north to a narrow width of 0.046 s at station SB4 in the south, suggestive of a north to south rupture. The MRFs for the target event are presented in Figure 5.2.

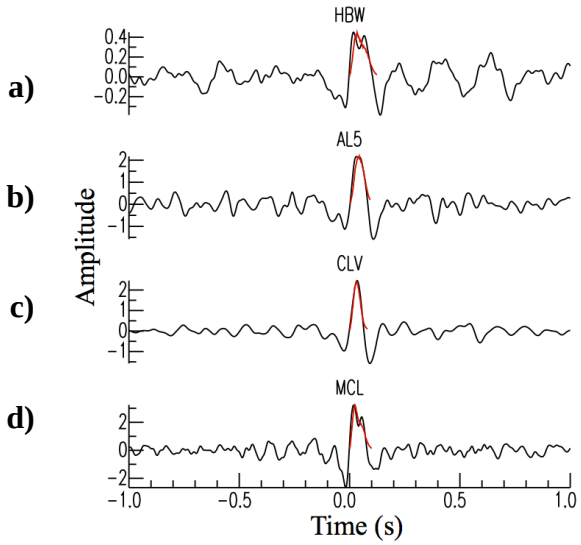

Figure 5.2: Stacked MRF pulse trains (black), cut pulses (red) for stations **(a)** HBW,**(b)** AL5, **c)** CLV, and **d)** MCL.

5.2 Finite Source Inversion

In the following, we summarize how finite-source parameters are obtained from MRFs, such as the ones shown in the last section. The method used to invert the MRF for slip distribution is based on the methods of Mori and Hartzell (1990), Mori (1993), Dreger (1997), and Dreger et al. (2007). Before inverting for finite-source dimensions the MRFs are normalized such that their area is equal to the scalar seismic moment of the target event. In this study we used a 61 x 61 gridded fault with dimensions of 1 km^2 with a corresponding subfault size of 16.4 m^2, and the DOE EGS LBNL catalog location and depth. The model assumes a constant rupture velocity of 0.8 times the shear wave speed at the source depth. The slip at each patch on the fault occurs with a slip velocity that is determined by the rise time of a 0.02 s fixed-width boxcar. The total allowable slip duration is 1 s. The subfault dimension is consistent with the 11.8 m wavelength for S waves with Vs = 2.94 km/s at 2.1 km depth and 250 Hz bandwidth. The inversion uses a slip positivity constraint and a smoothing constraint to minimize the spatial derivative of the slip. The smoothing weight is investigated by searching for the smallest value that produces a smoothed model with a fit close to the maximum fit to the data as measured by the variance reduction. The rupture area is determined by the number of subfaults with slip greater than 10% of the maximum slip and varies with smoothing parameter. This threshold is used to ignore small amplitude patches of slip that are poorly constrained by the inversion. Smoothing parameters of 2, 20, 200, and 2000 were investigated for an area ranging from 0.01 – 0.08 km^2, Table 5.3. The goodness of fit between the observed and synthetic MRFs is comparable for the strike, rake, and dip of both nodal planes yet one nodal plane with strike = 14, dip = 22, and rake = -75 has a smoothed and somewhat simpler slip distribution. The slip and stress change maps from the inversion of moment rate functions at four nearby stations for rupture velocity 80% of the local shear wave velocity are shown in the left and right columns,

respectively, in Figures 5.3a-d). The distributions vary depending on the smoothing parameter 2, 20, 200, and 2000. For this event the peak stress drop is somewhat low < 5 MPa. Based on this modeling, the preferred model has a smoothing of 200 (Figure 5.3c).

Table 5.3: Finite-source model smoothing parameter, slip area, and goodness of fit.

Smoothing	Slip Area (km^2)	Goodness of Fit %
2	0.0145	99.4
20	0.0223	99.3
200	0.0352	99.0
2000	0.0761	95.6

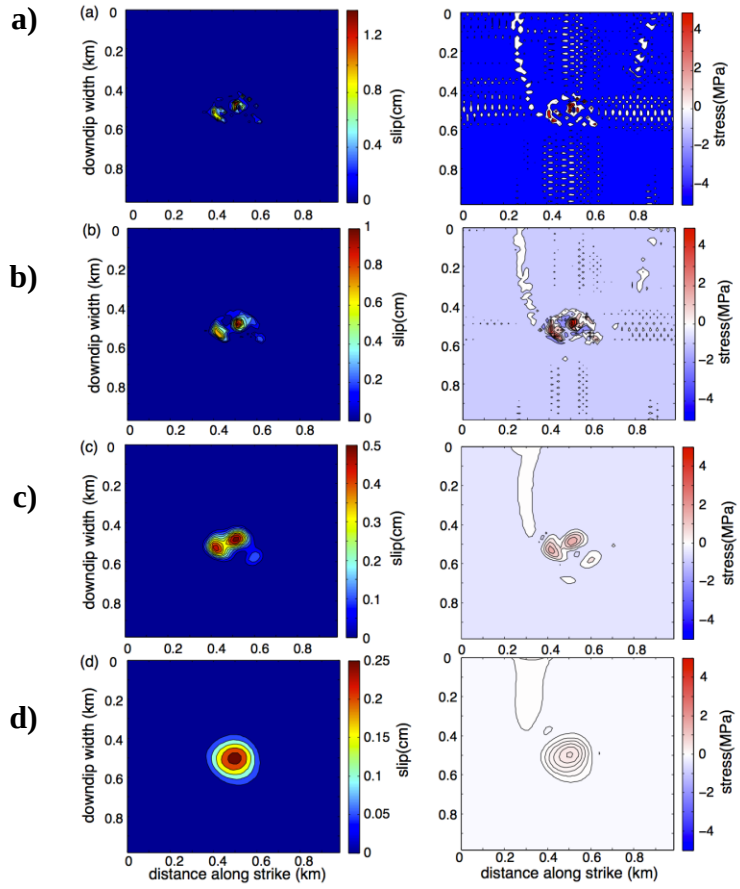

Figure 5.3: Slip (left column) and stress (right column) distributions from inversion of moment rate functions with smoothing parameters **a)** 2, **b)** 20, **c)** 200, and **d)** 2000. Stress change on the fault surface with red as stress drop and blue as stress increase.

5.2 Magnitude Scaling Relationship

We have obtained finite-source models for nine earthquakes at The Geysers spanning the magnitude range from Mw 2.1 to 5.1. As shown in Figure 5.4, the estimated area for these events is consistent with the scaling laws of both Wells and Coppersmith (1994) and Leonard (2010). This is remarkable as those relationships were developed for events with Mw larger than 5.5, and the great majority of events in those studies are for earthquakes larger than Mw 6.0 observed in other regions of the world. The results in Figure 5.4 demonstrate that The Geysers earthquakes follow the self-similar scaling law, but may be on average slightly more compact, or exhibit higher stress drop (plot below the solid lines in Figure 5.4) than the average of the events in Wells and Coppersmith (1994) and Leonard (2010). The Geysers events are found to lie within the two-sigma curves for the Leonard (2010) relationship (gray dashed lines), which represent approximately 10 (upper dashed line) and 100 bar (lower dashed line) stress drops.

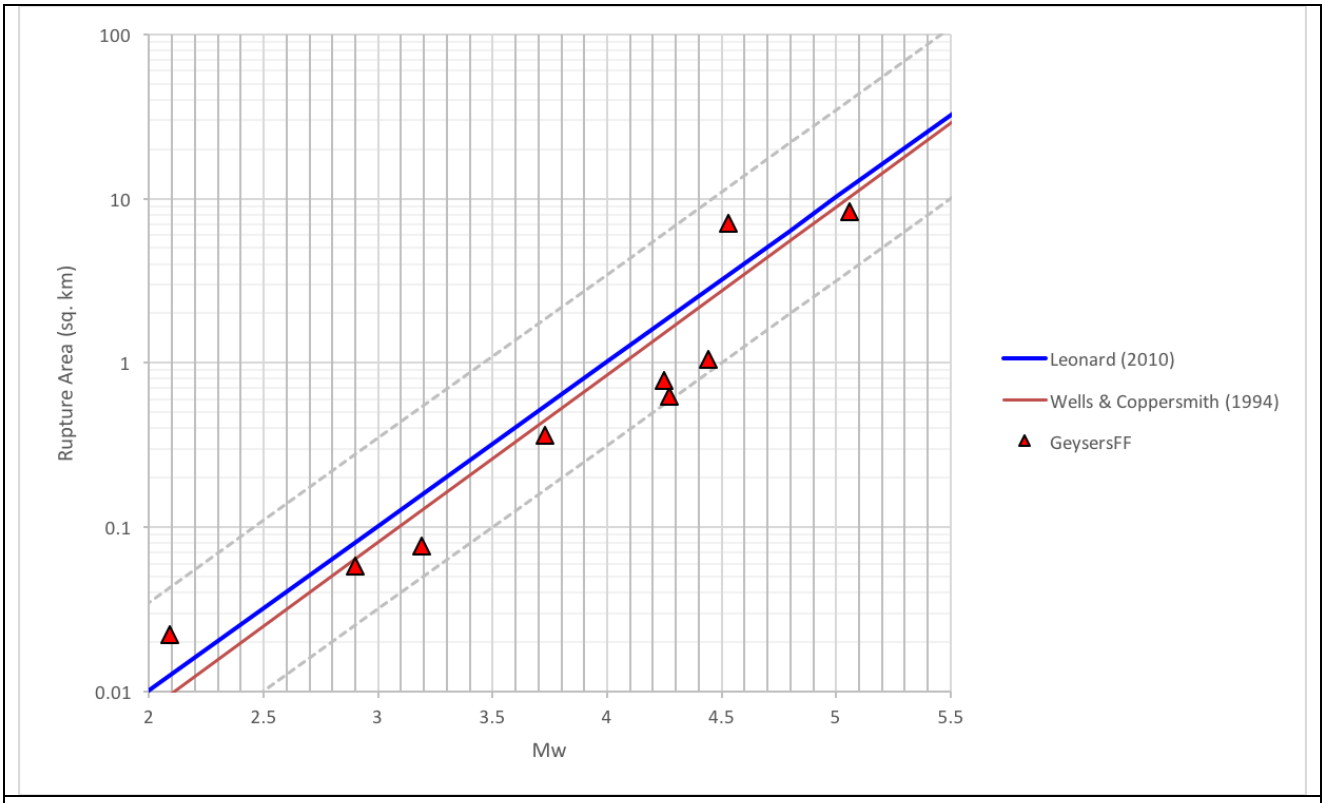

Figure 5.4: The Leonard (2010) (blue) and Wells and Coppersmith (1994) (orange) rupture area vs. Mw scaling laws are compared to area estimates for Geysers earthquakes obtained from finite-source inversion. The gray lines show the two-sigma errors for the Leonard (2010) relationship and represent approximately 10 bar (upper) and 100 bar (lower) stress drops.

The moment magnitude Mw estimates from the catalog derived for seismicity in the study area around Prati-32 were compared with those reported by LBNL, which are computed assuming a simplified spectral level method, and which are made available on the Northern

California Earthquake Data Center (NCEDC) website. It was found that the LBNL Mw magnitudes from the NCEDC-hosted catalog are approximately 0.6 magnitude units larger, due to assumptions in the spectral estimation method. Applying a correction of the catalog magnitudes based on the waveform inversion constraint will enable using the LBNL catalog Mw for thousands of earthquakes that otherwise cannot be analyzed with the more computationally intensive approach presented above, as well as for events below the magnitude limit for moment tensor analysis in order to map the coseismic fracture density in the study area. Figure 5.5 shows a comparison of waveform Mw magnitudes from moment tensor analyses with the corrected LBNL spectral Mw magnitudes indicating that the correlation after correction is very good.

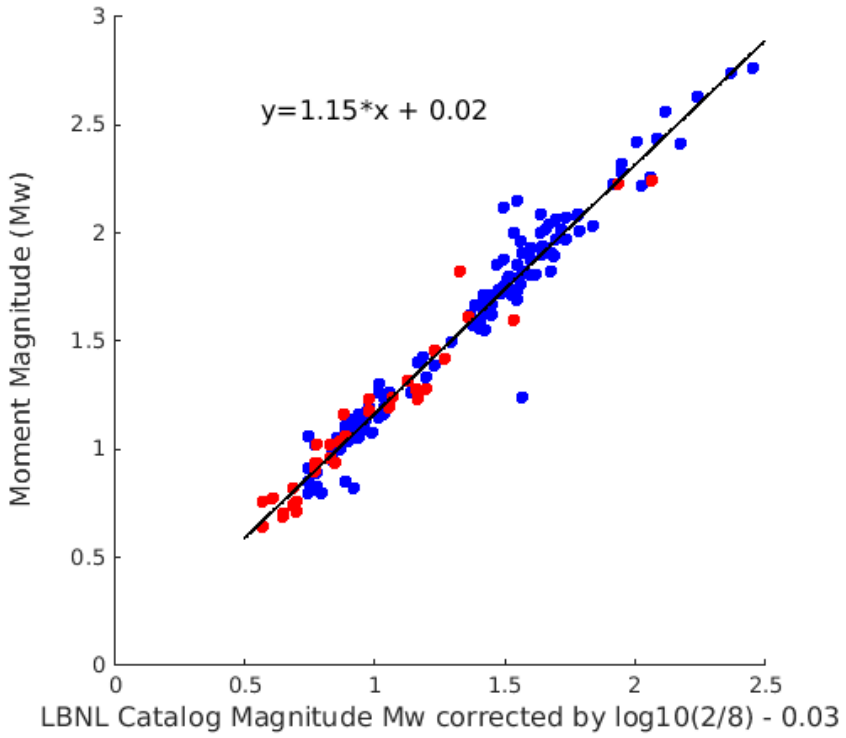

Figure 5.5: Comparison of waveform moment tensor Mw with LBNL catalog Mw. The LBNL Mw have been corrected by a factor of log10(2/8)-0.03 where the 2/8 ratio accounts for the difference between a theoretical half-space Green function and the semi-empirical half-space model. The -0.03 factor accounts for differences between the specific moment magnitude relationships used. Following correction, a regression of the Mw data recovers a nearly 1:1 slope and a zero intercept.

5.3 Fracture Network

We applied the Mw correction derived between our waveform results and those reported in the LBNL catalog to 7,416 events in the LBNL catalog spanning the period from November 16, 2009 through October 20, 2014, and subsequently applied the Leonard (2010) scaling law to convert to rupture area (Dreger et al., 2017). In Figures 5.6-5.8, we selected a subset of 752 events from October 1, 2009 to September 30, 2015 with high accuracy locations from the LBNL catalog (Mw 0.3 -2.2), to construct a 3D representative image of the discrete fracture network stimulated by the injection of fluid into the hot rock below Prati-31 and Prati-32. The high accuracy locations of the 752 events were determined by selecting a minimum of 16 travel times phase picks per event and a maximum RMS error between calculated and observed travel times of 0.05s. The rupture area associated with these events where estimated using the moment magnitudes and the Leonard (2010) scaling relationship. For a more realistic representation of the fracture network, we characterize the discreate fractures by circles with size, strike and dip orientation according to our magnitude scaling and stress inversion results (Section 8). The diameter of each fracture circle was determined by the rupture area-scaling relationship, while the strike and dip were determined using statistics with a Gaussian distribution based on the results of the stress inversions as presented in section 8, which indicated a σ_1 direction N20^{o}E with an uncertainty of 10^o (two-sigma) and a dip of 80^o with the same uncertainty. The results of the statistical representation of such a fracture network are presented in Figures 5.6-5.8. In these figures the rupture area is represented by the size of the circles, while the colored dots at the hypocenters denote the moment magnitude of the events. The shape of the circles has degenerated to ellipses, because of the compressed vertical axis (1:2) and the oblique view of the plot.

The plots reveal that the highest concentration of fractures is located approximately 300 m to the north and 400 m below the bottom of the injection and production wells. With a strike of N10^{o}E ± 10^o the fractures are subparallel to the NE-SW trend of the faulting encountered in the NW Geysers. The Caldwell Pines Fault, which intersects the Prati-32 study area, trends in NE-SW direction, while other shorter faults segments in the vicinity of the study area trend in NNE-SSW direction (see Figure 1.1). Although the dip of these faults is unknown, the results of the stress analysis (σ_3 = 80^o ± 10^o) suggest that they may be subvertical similar to the fracture network in Figures 5.6-5.8.

It is noted that the fracture network in Figures 5.6-5.8 represents a subset of all fractures in the subsurface. As mentioned above, this subset is based on 752 out of 7,416 events with high hypocenter accuracy. When the accuracy is lowered to (i.e.) a minimum of eight travel times phase picks and a maximum RMS error between calculated and observed travel times of 0.05s per event location, the number of fractures in the study area increases to 3,296. However, the spatial distribution of the fractures is not different from that seen in Figures 5.6-5.8, while the total number is increased.

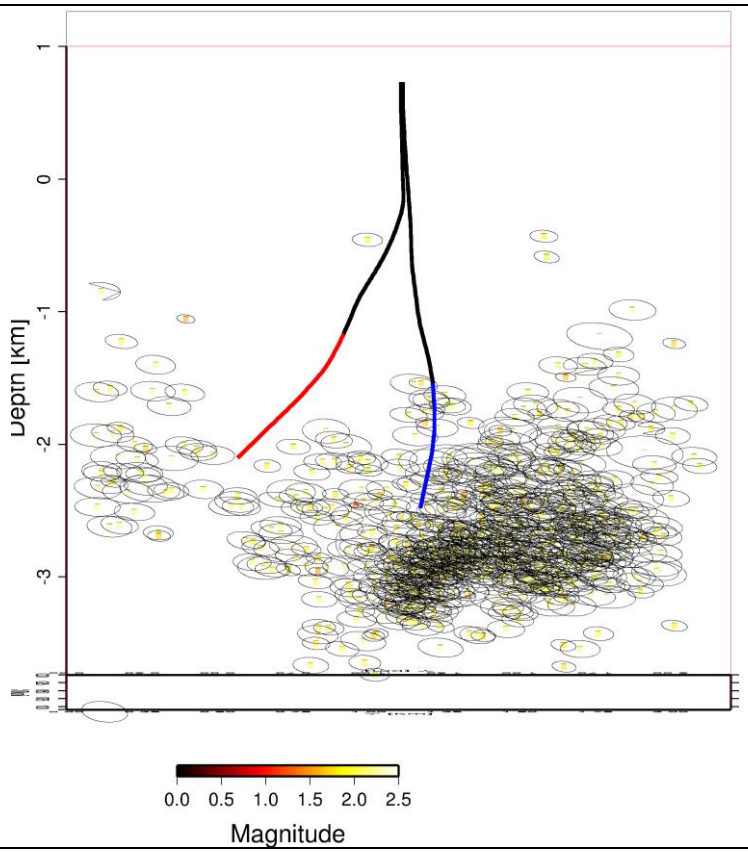

Figure 5.6: Statistical representation of the generated fracture network below production well Prati-31 (red) and injection well Prati-32 (blue). The circle diameters represent the rupture area, which the colored dots at the hypocenters denotes the moment magnitude. The shape of the circles is deformed to ellipses because the vertical axis is vertically compressed (1:2) and because of the fracture dip. View from east to west.

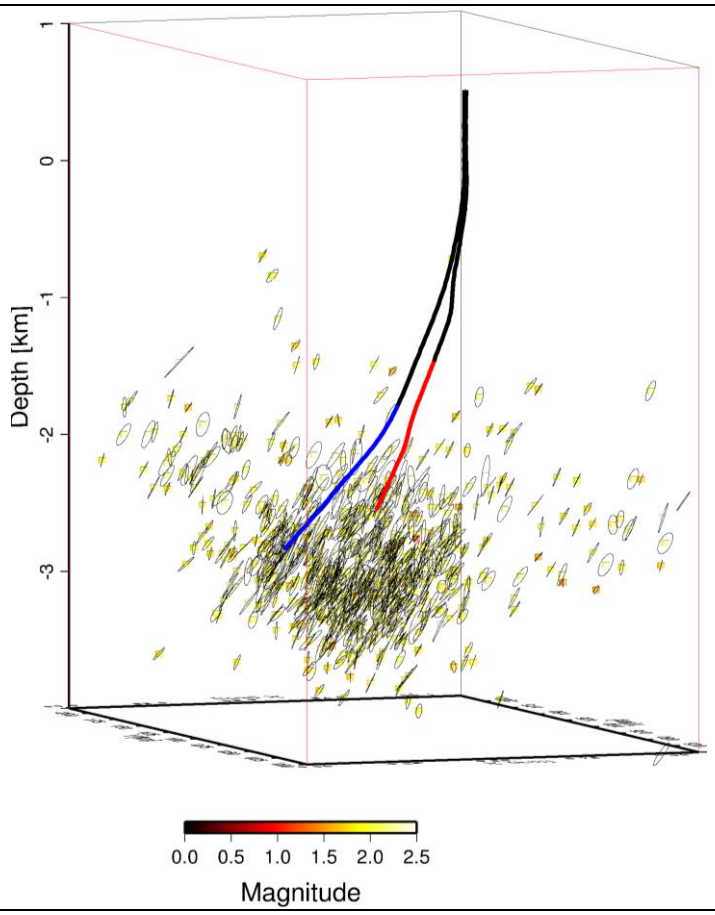

Figure 5.7: Same as Figure 5.6. View from southwest to northeast in the direction of σ_1.

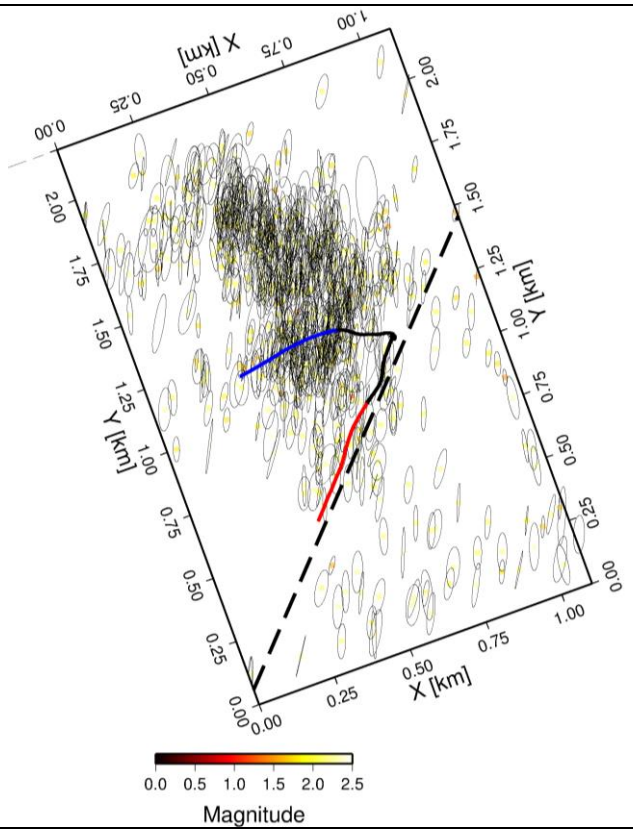

Figure 5.8: Same as Figure 5.6. View vertically down. The dashed black line approximates the trajectory of the Caldwell Pines Fault.

6.0 Aleatory and Epistemic Uncertainty of Double-Difference Wadati Method

The objective of this task is to appraise the uncertainty of the DDW method as it relates to the geometry at the Prati-32 injection site. The analysis appraises aleatory and epistemic uncertainty due to stations topology and errors in phase picks. We evaluate the available high-frequency and broadband datasets for station topology and picking error of the phase arrivals. Bootstrapping and jackknifing of data and stations, respectively, is conducted to assess the effect of outliers in the travel time picks and seismic network topology.

6.1 Aleatory and Epistemic Uncertainty

Statistical data analysis is often based on approaches to separately analyze uncertainty due to randomness of the system from uncertainty due to lack of knowledge. The former is referred to as aleatory uncertainty, while the latter is referred to as epistemic uncertainty. In the case of DDW, we will model and analyze the aleatory uncertainty by adding random Gaussian

distributed noise to the differential phase arrivals of the data, while epistemic uncertainty will be modeled by jackknifing seismic station from the original datasets. In the following, the uncertainty analysis for the results presented in section 2.5 (Figures 2.15 and 2.16) will be presented.

6.2 Aleatory Uncertainty of Seismic Geophone Data

During this task, the uncertainty due to randomness in the system was analyzed by adding Gaussian distributed noise to the differential phase estimates for each event pair at a recording station. An appropriate standard deviation for the Gaussian distribution was selected considering the central frequency of the seismic waves associated with the seismicity in the study area of Prati-32, which is approximately 25 Hz. We chose a conservative error of 1/4 wavelength for the waveform cross correlation results of the seismic waves, which translated to a standard deviation of $\sigma = 0.01$ s. Therefore, the uncertainty of the results from waveform cross correlation was modeled by adding Gaussian distributed noise with zero mean ($\mu = 0.0$ s) and a standard deviation of 0.01s to the double difference results from waveform cross correlation that were shown in Figures 2.15b and 2.16b. The distribution of Gaussian noise for the pre-injection data is presented in Figure 6.1. As expected, the histogram reveals a normal distribution around zero mean with a standard deviation of $\sigma = 0.01$ s.

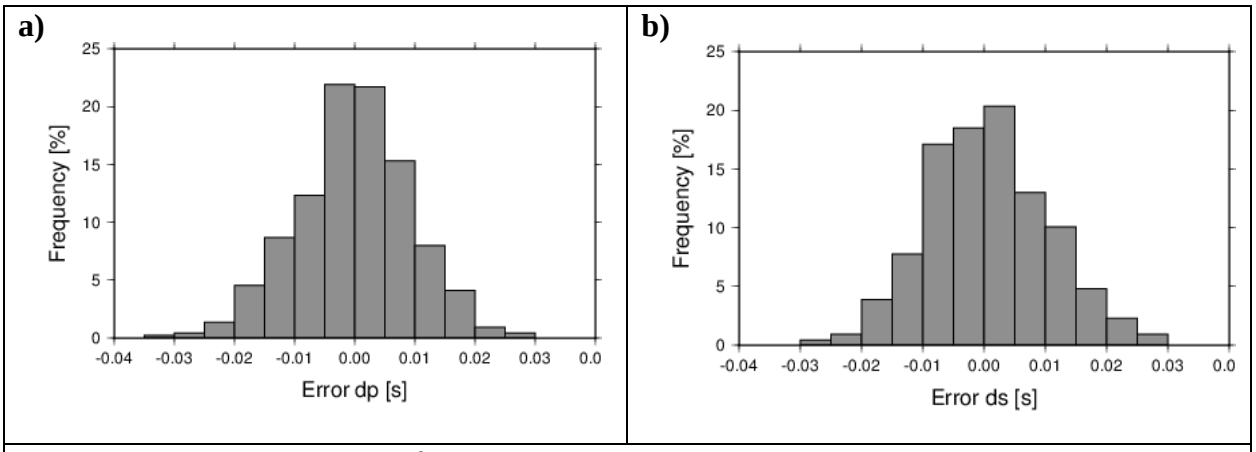

Figure 6.1: a) Histogram of Gaussian distributed errors added to pre-injection double difference P-wave times. **b)** Same as a) for S-wave times.

After adding noise to the data, bootstrapping was performed to select random sets of data ensembles for subsequent L1-L2 fitting on the Wadati diagram. A total of 1,000 bootstrapping realizations were performed to appraise the uncertainty due to randomness in the system. The result of the noise-perturbed pre-injection data is presented in Figure 6.2. This result should be compared to Figure 2.15b. The result of the bootstrapping analysis yielded a Vp/Vs-ratio of 1.78 and an uncertainty of $\sigma = 0.05$ (Figure 6.2). The estimate of the Vp/Vs-ratio and its uncertainty indicates that the result is statistically insignificant to the estimates of the original field data (Vp/Vs = 1.76, $\sigma = 0.04$) that were presented in Figure 2.15b. The results suggest that the Vp/Vs estimates of the pre-injection phase are stable with respect to aleatoric uncertainty in the system.

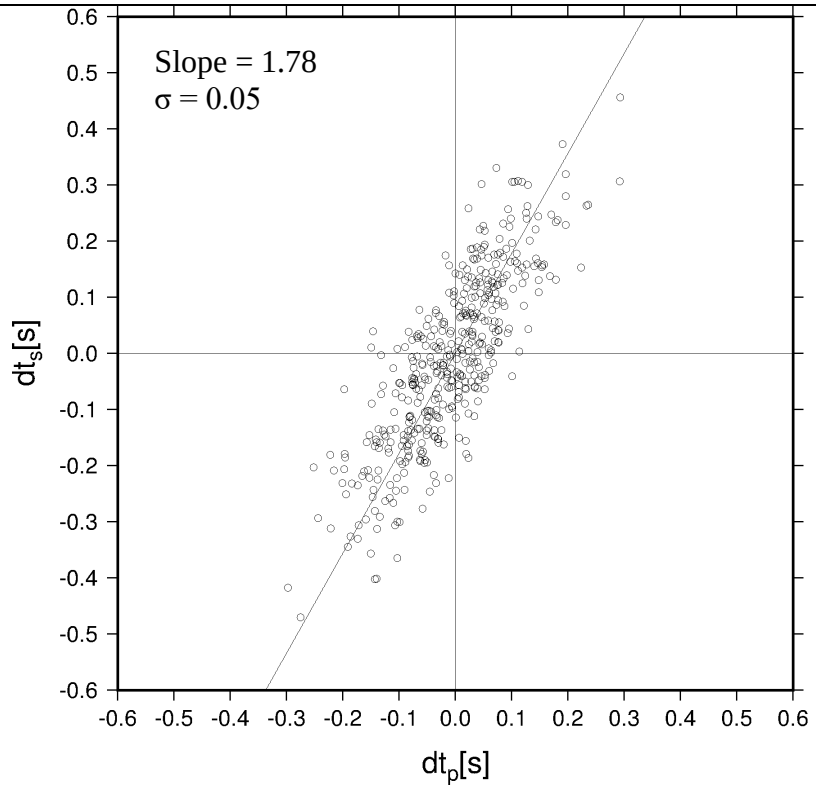

Figure 6.2: Wadati diagram with pre-injection differential P- and S-wave travel time pairs derived by adding Gaussian distributed noise and bootstrapping the data in Figure 2.15b.

The distribution of Gaussian noise for the post-injection data is presented in Figure 6.3. Again, the histogram displays a normal distribution around zero mean with a standard deviation of $\sigma = 0.01$ s. As in the pre-injection case, noise was added to the data and bootstrapping was performed to select random sets of data ensembles for subsequent fitting on the Wadati diagram. The result of the noise-perturbed post-injection data is presented in Figure 6.4 and should be compared to Figure 2.16b. The bootstrapping analysis yielded a Vp/Vs-ratio of 1.70 with an uncertainty of $\sigma = 0.05$ (Figure 6.4). The estimate of the uncertainty indicates that the result of the Vp/Vs-ratio is statistically insignificant to the estimates of the field data (Vp/Vs = 1.67, σ = 0.04) that were presented in Figure 2.16b. As in the pre-injection analysis, the current results suggest that the Vp/Vs estimates of the post-injection phase are also stable with respect to aleatoric uncertainty in the system.

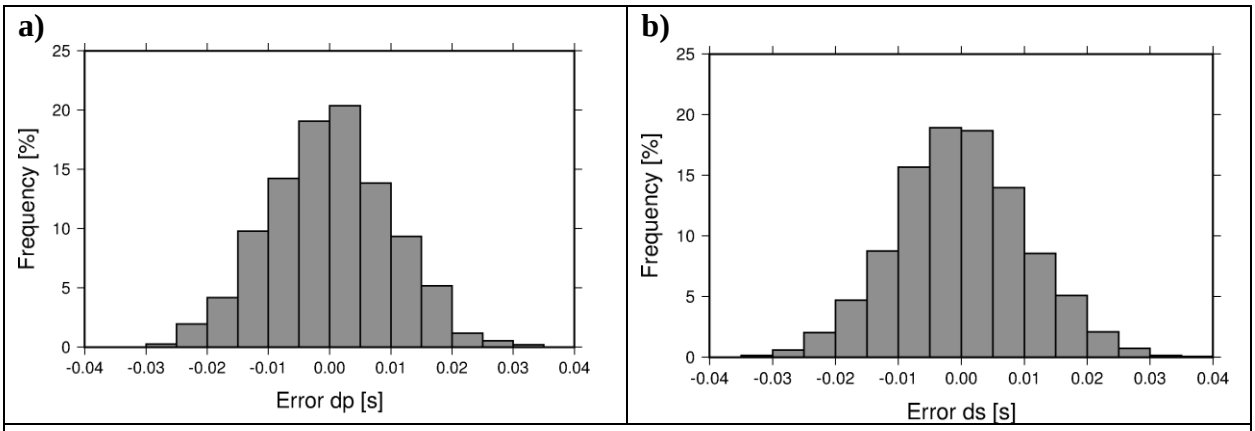

Figure 6.3: a) Histogram of Gaussian distributed errors added to post-injection double difference P-wave times. **b)** Same as a) for S-wave times.

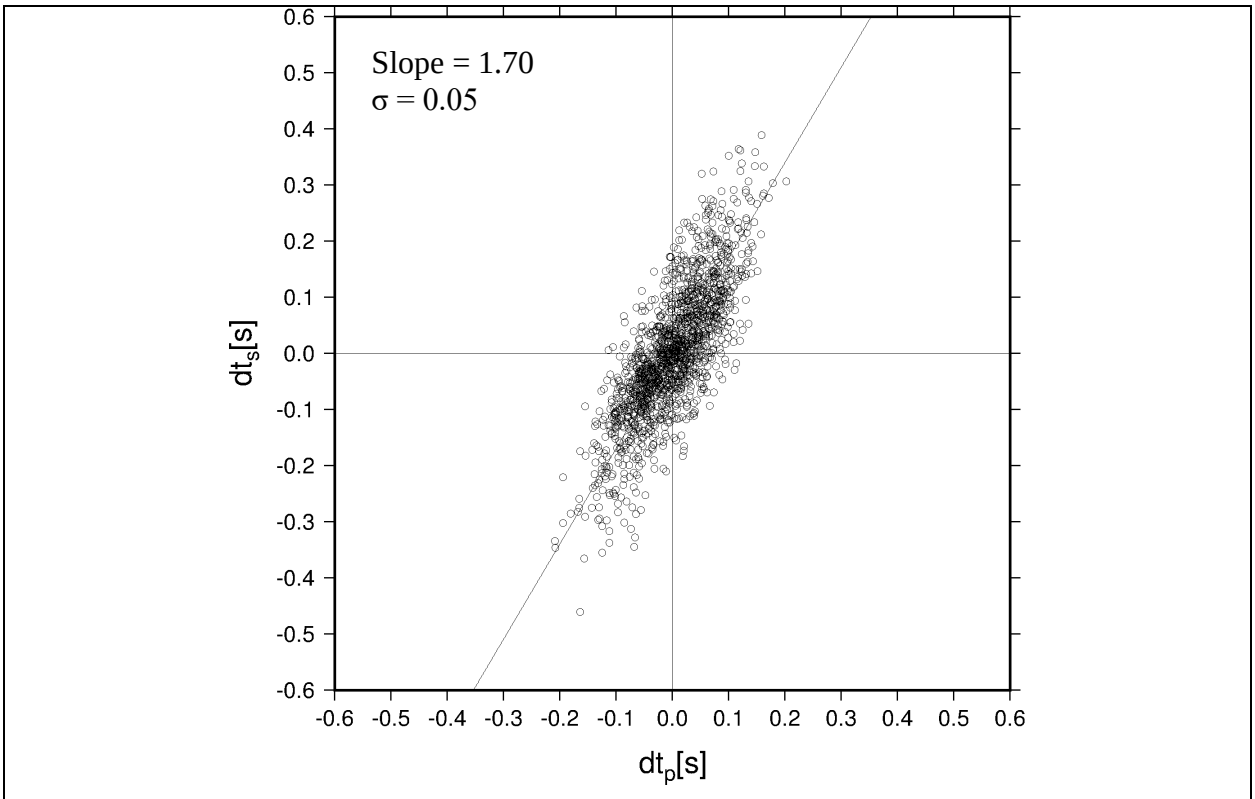

Figure 6.4: Wadati diagram with pre-injection differential P- and S-wave travel time pairs derived by adding Gaussian distributed noise and bootstrapping the data in Figure 2.16b.

6.3 Epistemic Uncertainty of Seismic Geophone Data

The lack of knowledge about a system under investigation is referred to as epistemic uncertainty. Lack of knowledge in the case of analyzing data recorded by a seismic network can be modeled by varying the number of stations and consequently the amount of data of the system under investigation. In the two cases above, the pre- and post-injection analyses were based on data from 18 and 16 stations, respectively. These stations were used as the basis for jackknifing stations using a bootstrapping technique. The uncertainty analysis was based on the restrictions that a minimum of 65% of the original stations needed to be selected for analysis and that their resulting station gap should be less than 150^{o}. With these restrictions 100 realizations were run, where bootstrapping was used to select a subset from the original set of stations. For each subset, L1-L2 fitting on the Wadati diagram was performed to obtain an estimate of the Vp/Vs-ratio in the study area. Finally, the estimates from the 100 single realizations were averaged to obtain an overall estimate and uncertainty for the Vp/Vs-ratio in the study area.

An example of a Wadati diagram with double difference data from bootstrapping realization No. 5 for the pre-injection case is presented in Figure 6.5. The slope of the data from the bootstrapped stations for this realization is 1.72. The associated station distribution, for the same realization is shown in Figure 6.6. The map includes 12 stations that were selected during the bootstrapping realization No. 5, which represent a subset of the network shown in Figure 2.15a. The resulting station gap is 115^{o}.

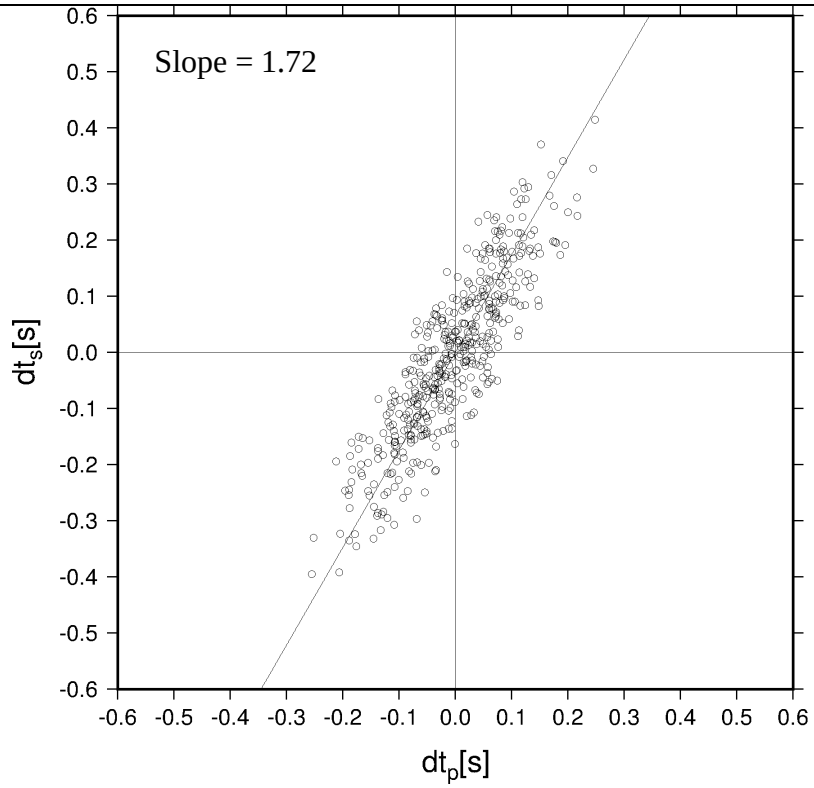

Figure 6.5: Wadati diagram with pre-injection differential P- and S-wave travel time pairs obtained from one realization of bootstrapping stations from the subset shown in Figure 2.15a.

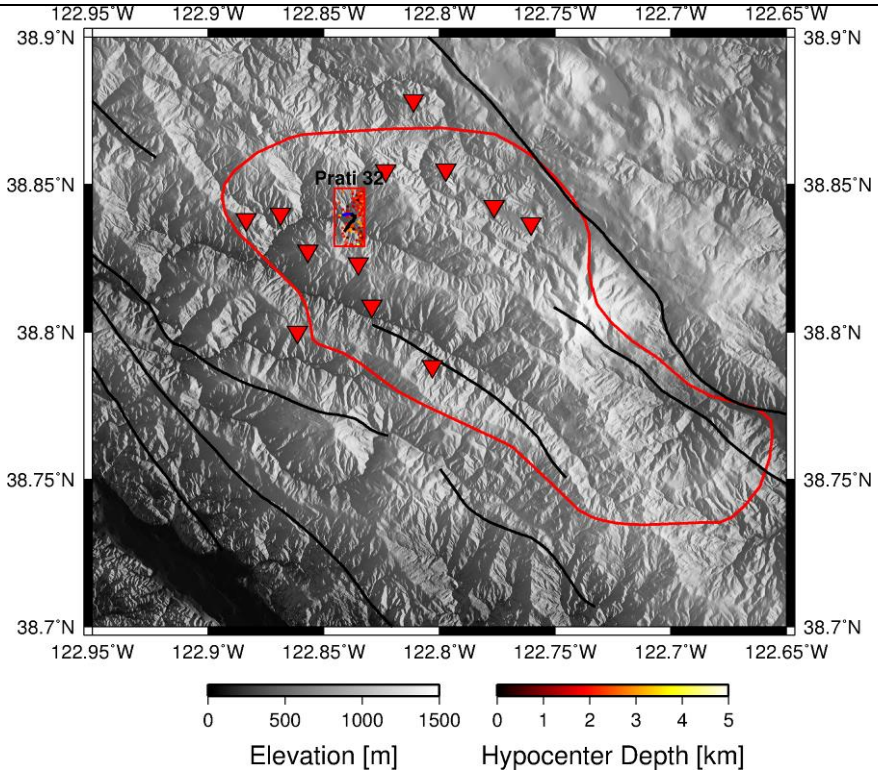

Figure 6.6: Map of the study area of Prati-32 with epicenters of two years pre-injection seismicity. The red triangles denote the 12 seismic stations that were selected in the bootstrapping realization No. 5, which represents a subset of the stations shown in Figure 2.15a. The associated station gap is 115°.

Averaging the slopes of all 100 realization yields a value of 1.74 with an uncertainty of σ = 0.02. This value is statistically insignificant to the estimate derived with the original system of 1.76 with an uncertainty of σ = 0.04 (see Figure 2.15b). Therefore, the statistical analysis of the seismic network topology shown in Figure 2.15a proves that the resulting estimates of Vp/Vs-ratio are independent of aleatoric uncertainty in the system.

In the case of post-injection data (refer to Figure 2.16), a representative Wadati diagram with double difference data from bootstrapping realization No. 5 is presented in Figure 6.7. The slope of the data from the bootstrapped stations for this realization is 1.70. The associated station distribution, for the same realization is shown in Figure 6.8. The map includes 10 stations that were selected during the bootstrapping realization No. 5, which represent a subset of the network shown in Figure 2.16a. The resulting station gap is 127°.

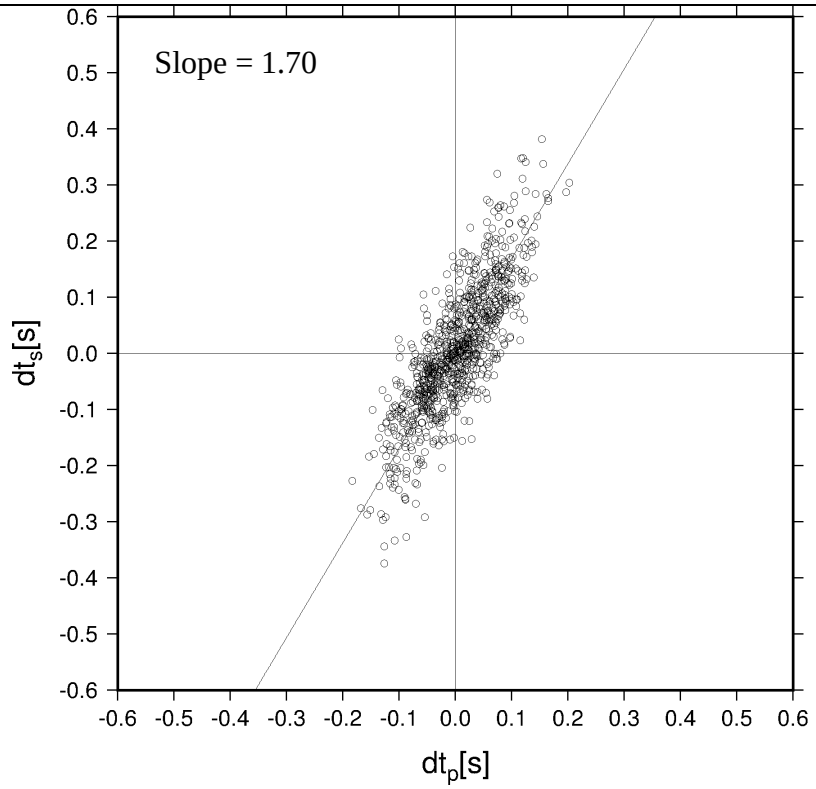

Figure 6.7: Wadati diagram with post-injection differential P- and S-wave travel time pairs obtained from one realization of bootstrapping stations from the subset shown in Figure 2.16a.

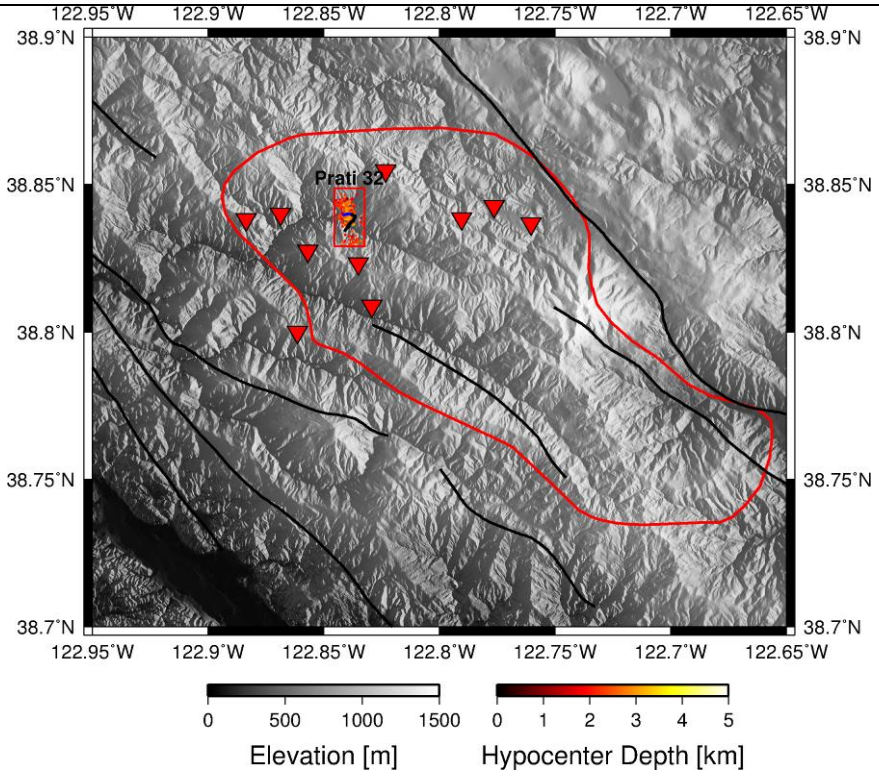

Figure 6.8: Map of the study area of Prati-32 with epicenters of three months post-injection seismicity. The red triangles denote the 10 seismic stations that were selected in the bootstrapping realization No. 5, which represents a subset of the stations shown in Figure 2.16a. The associated station gap is 127°.

Averaging the slopes of all bootstrapping realization results in a value of 1.69 with an uncertainty of $\sigma = 0.05$. This value compares to the estimate of $1.67 \pm \sigma = 0.04$ derived from the original system (see Figure 2.16b). It can be seen that these values are statistically insignificant and therefore, the statistical analysis of the seismic network topology shown in Figure 2.16a proves that the resulting estimates of Vp/Vs-ratio are independent of aleatoric uncertainty in the system.

In summary, it can be stated that the results of the DDW method as related to the data obtained with the geophone network are stable and independent of aleatory and epistemic uncertainties in the system. The result is due to the good station coverage surrounding the study area of Prati-32 and due to the waveform cross correlation method, which yield accurate results for differences in phase arrival times from neighboring events observed at the same seismic station.

6.4 Analysis of Seismic Broadband Data

During the operation of Prati-32 EGS injection activities, a temporary broadband seismic network was operated at The Geysers. A total of 26 broadband stations were operational inside the reservoir perimeter of The Geysers from July 2012 to July 2013, while seven stations were located in a circular pattern at a distance of approximately 50 km surrounding The Geysers. The current project was tasked with processing and analyzing the broadband data including determination of phase arrivals, hypocenter locations and origin times for the whole region of the reservoir. The results of which were already reported in section 4. In the following, we report the results of applying the DDW method to the broadband data recorded in the study area of the Prati-32 demonstration project.

The broadband data were processed in the same way as the geophone data, with the difference that the former were first bandpass filtered between 5-25 Hz. The bandpass filtering was followed by waveform cross correlation to obtain differential P- and S-wave phase arrival times for neighboring events, for which waveforms were recorded by the same station. The differential phase arrival times were then displayed on a Wadati diagram and fitted with the L1-L2 norm, as in the case of geophone data.

We first analyzed the broadband data to obtain an estimate of the Vp/Vs-ratio in the Prati-32 study area from July 2012 to July 2013, followed by a statistical uncertainty analysis as described for the geophone data above. The results of the DDW analysis of the broadband data are presented in Figure 6.9. The number of data points on the Wadati diagram, relative to the data from the three months post-injection period in Figure 2.16b, has increased 10-fold due to the longer recording period of one year. It can also be seen that the slope, representing the Vp/Vs-ratio in the study area of Prati-32, has decreased to 1.65 with an uncertainty of $\sigma = 0.03$. It appears as if the low value of Vp/Vs-ratio that was observed for the three months post-injection period (Figure 1.16b, Vp/Vs = 1.67, $\sigma = 0.04$), relative to the pre-injection result (Figure 2.15b, Vp/Vs = 1.76, $\sigma = 0.04$), has stabilized over the 1.5 years of the injection until at least July 2013. This is in agreement with a steam plume forming in the injection volume below Prati-32. It appears that this plume, once developed, remained stable during the injection phase.

The map with broadband stations that recorded the seismicity from which the data in Figure 6.9 were derived is shown in Figure 6.10. A total of 18 stations recorded the broadband data, which is comparable to the number of geophone stations recording the pre- and post-injection seismicity in Figures 2.15a and 2.16a. The high number of stations results in a small station gap of 95^{o}, which ensures stable estimates from the DDW analysis.

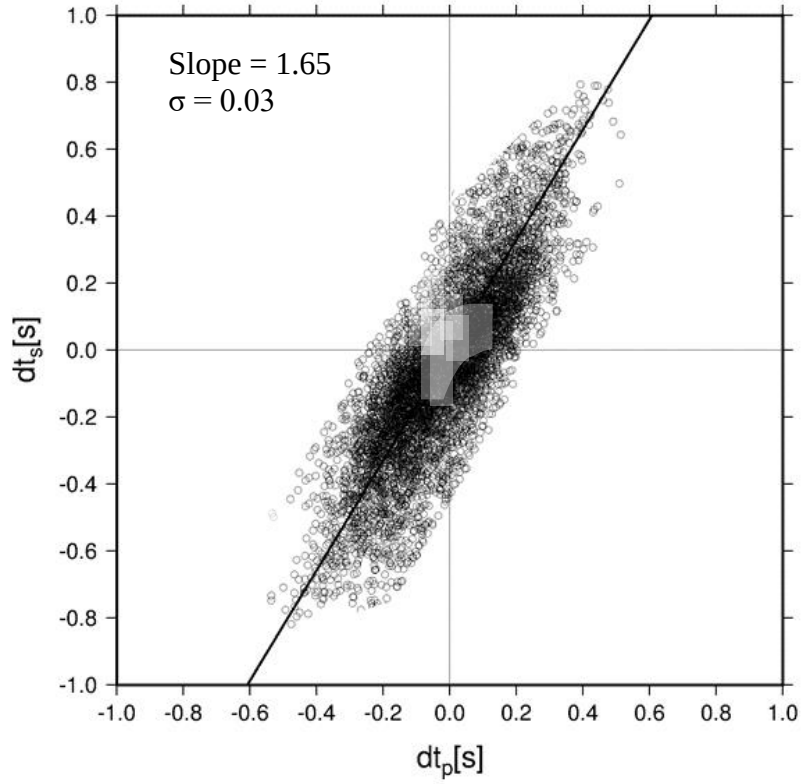

Figure 6.9: Wadati diagram with differential P- and S-wave travel time pairs obtained from one year of broadband data recorded from July 2012 to July 2013.

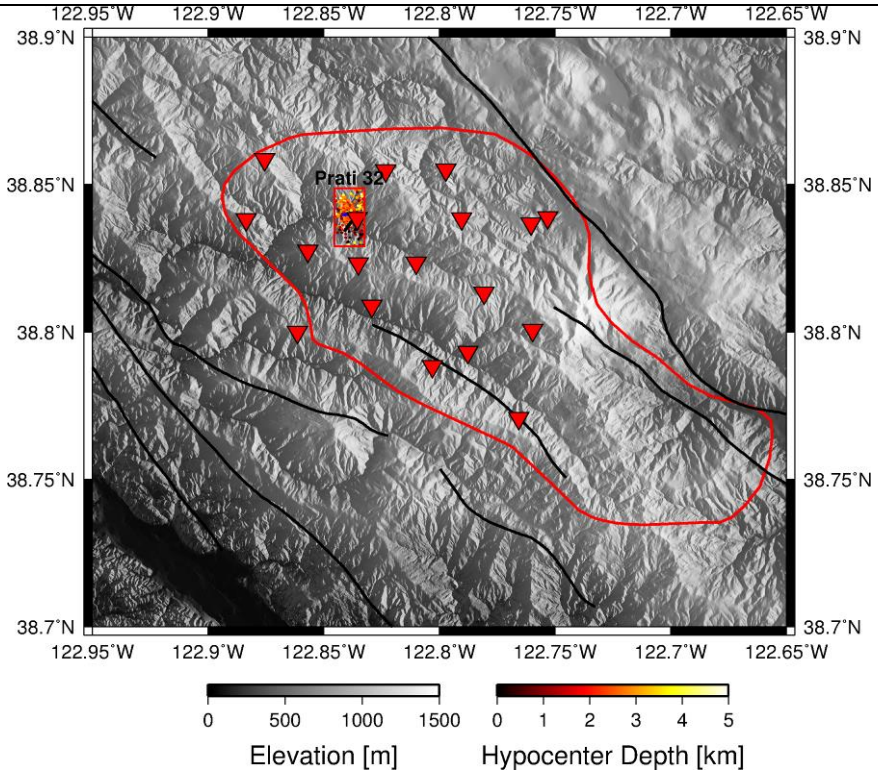

Figure 6.10: Map of the study area of Prati-32 with epicenters of a one-year interval from July 2012 to July 2013. The red triangles denote the 18 seismic broadband stations that recorded the seismicity in the study area. The associated station gap is 95°.

6.5 Aleatory Uncertainty of Seismic Broadband Data

As with the geophone data, we analyze the uncertainty due to randomness in the system by adding Gaussian distributed noise to the original differential phase estimates (Figure 6.9) for each event pair at a recording station. The mean and standard deviation for the Gaussian distribution were the same as for the geophone data at $\mu = 0.0$ s and $\sigma = 0.01$ s, respectively. Considering that the passband of the broadband filter was 5-25 Hz, the standard deviation translates to an error slightly higher than 1/4 wavelength for the waveform cross correlation results. The distribution of noise for the broadband data is presented in Figure 6.11. As expected, the histogram reveals a normal distribution around zero mean with a standard deviation of $\sigma = 0.01$ s.

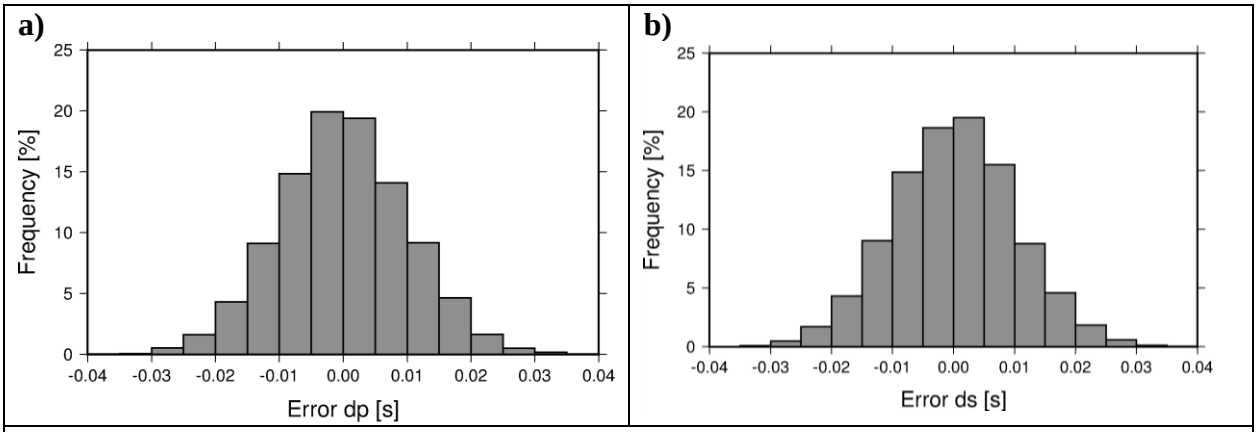

Figure 6.11: a) Histogram of Gaussian distributed errors added to broadband double difference P-wave times. **b)** Same as a) for S-wave times.

After Gaussian noise was added to the data in Figure 6.9, bootstrapping was performed to select random sets of data ensembles for subsequent L1-L2 fitting on the Wadati diagram. In the case of broadband data, 100 bootstrapping realizations were performed to appraise the uncertainty due to randomness in the system. The result of the noise-perturbed broadband data is presented in Figure 6.12 and should be compared to Figure 6.9. The bootstrapping of the broadband data yielded a Vp/Vs-ratio of 1.60 and an uncertainty of $\sigma = 0.02$, which is statistically insignificant to the estimates of the field data (Vp/Vs = 1.65, $\sigma = 0.03$) that were presented in Figure 6.9. The results suggest that the Vp/Vs estimates of the post-injection phase are stable with respect to aleatoric uncertainty in the system.

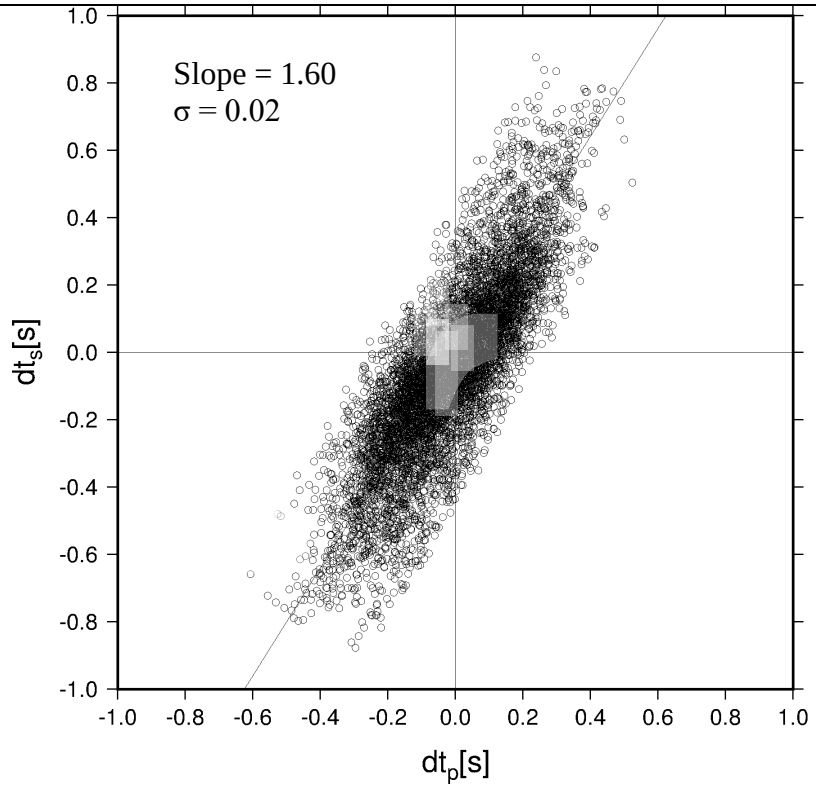

Figure 6.12: Wadati diagram with differential P- and S-wave travel time pairs derived by adding Gaussian distributed noise and bootstrapping the data in Figure 6.9.

6.6 Epistemic Uncertainty of Seismic Broadband Data

For the epistemic uncertainty in the analysis of the broadband data, we revisit the technique we applied to the geophone data above, with the assumption that lack of knowledge in the case of data recorded by a seismic network can be modeled by varying the number of stations and consequently the amount of data in the system under investigation. During the one-year operation of the broadband network, the seismicity in the Prat 32 study area was recorded by 18 stations (Figure 6.10), which formed the basis for the jackknifing and bootstrapping technique. As before, the uncertainty analysis was based on the restrictions that a minimum of 65% of the original stations needed to be selected for analysis and that their resulting station gap should be less than 150°. With these restrictions 100 realizations were run, where bootstrapping was used to select a subset from the original set of stations. For each subset, L1-L2 fitting on the Wadati diagram was performed to obtain an estimate of the Vp/Vs-ratio. In a final step, the resulting estimates from the 100 realizations were averaged to obtain an overall estimate and uncertainty for the Vp/Vs-ratio in the study area.

An example of a Wadati diagram with double difference data from bootstrapping realization No. 5 for the broadband data is presented in Figure 6.13. The slope of the data from

the bootstrapped stations for this realization is 1.67. The station distribution for the same realization is shown in Figure 6.14. The map includes 12 stations that were selected during bootstrapping realization No. 5, which represent a subset of the network shown in Figure 6.10. The resulting station gap is 97º.

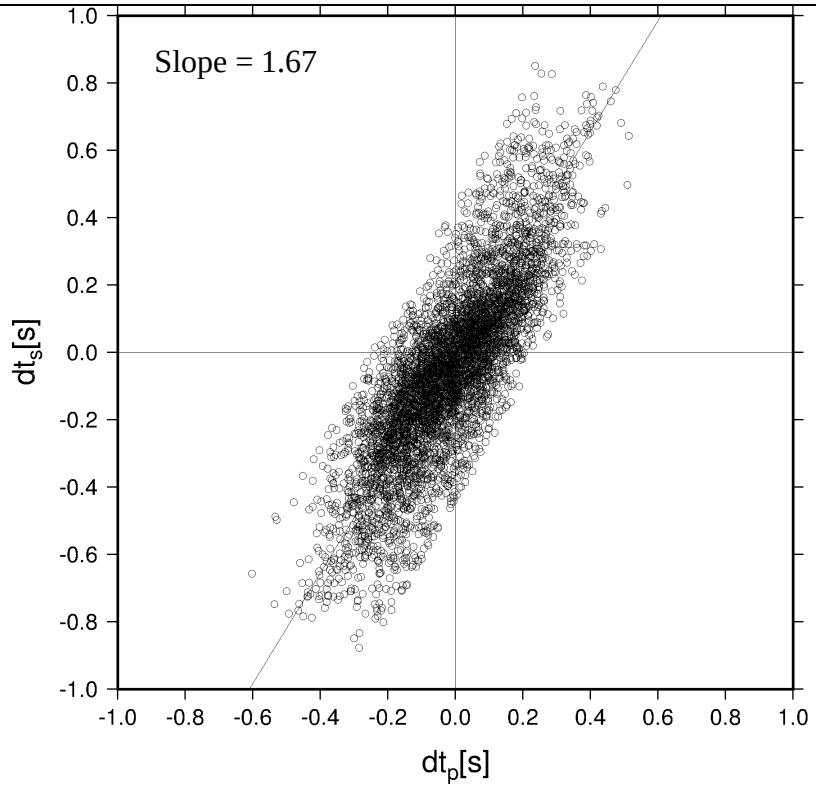

Figure 6.13: Wadati diagram with differential P- and S-wave travel time pairs obtained from one realization of bootstrapping broadband stations from the subset shown in Figure 6.10.

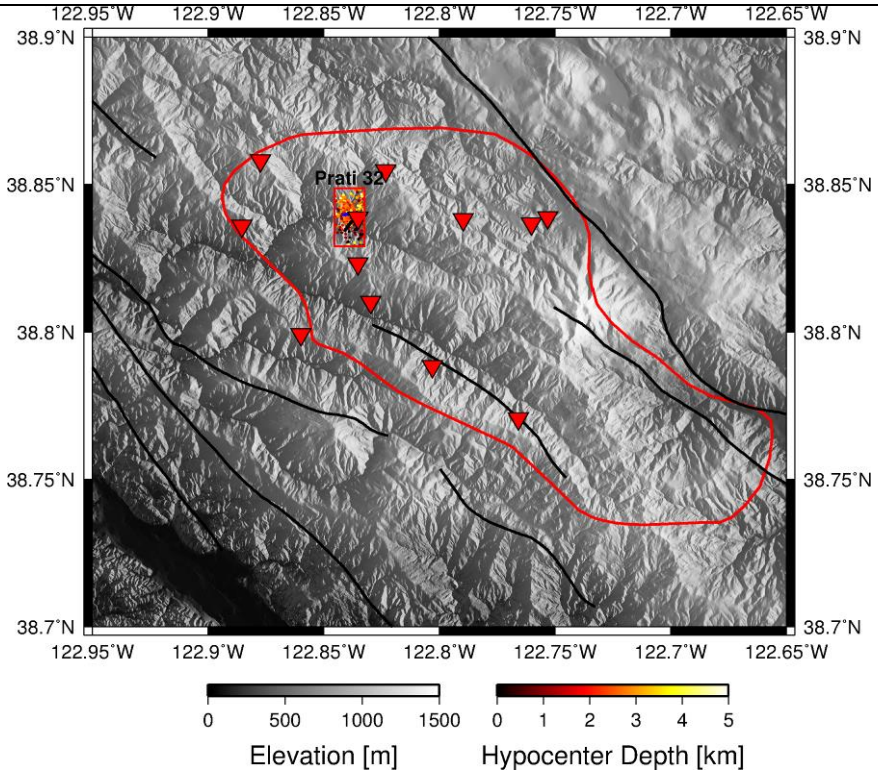

Figure 6.14: Map of the study area of Prati-32 with epicenters of a one-year interval from July 2012 to July 2013. The red triangles denote the 12 seismic broadband stations that were selected in the bootstrapping realization No. 5, which represents a subset of the stations shown in Figure 6.10. The associated station gap is 97°.

Averaging the slopes of all bootstrapping realization results in a value of 1.64 with an uncertainty of $\sigma = 0.02$. This value compares to the estimate of $1.65 \pm \sigma = 0.03$ derived from the original system (see Figure 6.9). It can be seen that these values are statistically insignificant and therefore, the statistical analysis of the seismic network topology shown in Figure 6.10 proves that the resulting estimate of Vp/Vs-ratio is independent of aleatoric uncertainty in the system.

Thus, it can be summarized that the results of the DDW method applied to the data recorded by the broadband network are stable and independent of aleatory and epistemic uncertainties in the system. This is due to the good station coverage and due to the waveform cross correlation method, which yields accurate results for differences in phase arrival times from neighboring events observed at the same seismic station. The theory of the DDW techniques assumes that the take-off angles for P- and S-waves from the source region are the same, which is an approximation and only valid when the station coverage of the recording network is high enough with acceptable station gaps. The results of the uncertainty analysis presented here confirm that the station coverage and data quality is good enough to apply DDW in the study area of Prati-32.

6.7 Summary

We conducted statistical analyses of aleatory and epistemic uncertainty related to the application of DDW to the seismicity recorded by a geophone- and broadband sensor networks at the Prati-32 injection demonstration project. It was found that the Vp/Vs-ratio in the two years prior to injection was close to that for typical crustal rocks, which was interpreted to indicate that the reservoir rocks in the study area are undisturbed due to the absence of injection and production activities.

A drop of Vp/Vs in the three months after the start of injection indicated that a steam plume developed below the injection point of Prati-32. This is in agreement with the assumption of water flashing to steam upon contact with the rock in this high temperature reservoir.

The analysis of broadband data, recorded nine months after the start of injection and for the duration of one year, indicates that the steam plume is still present in the system.

Analysis of aleatory and epistemic uncertainty of the geophone- and broadband seismic networks indicated that the Vp/Vs estimates are stable with respect to randomness and lack of knowledge in the system.

7.0 Spatial Analysis of Fluid Injection

In sections 2 and 5, DDW was applied to high-accuracy P- and S-wave differential travel times derived from waveform cross correlation to image fluid saturation in the injection volume of the Prati-32 study area based on Vp/Vs-ratio. In our initial analysis (section 2.5) we investigated temporal changes in fluid saturation comparing pre- to post-injection seismicity in the study area of Prati-32. We reported a pre-injection Vp/Vs ratio of 1.76 with a standard deviation of 0.04 (Figure 2.15). The value, being close to the typical Vp/Vs of 1.73 for crustal rocks, was interpreted to indicate that the reservoir rocks in the study area were undisturbed due to the absence of injection and production activities. However, our analysis of seismitiy observed after the start of water injection revealed a drop in Vp/Vs to 1.67 with a standard deviation of 0.04 (Figure 2.16). This statistically significant decrease in Vp/Vs was interpreted by the development of a steam plume in the injection volume of Prati-32, due water flashing to steam in this high-temperature region of the reservoir.

7.1 Spatial Variation of Fluid Saturation

In the current section, we analyze the spatial variation of the fluid saturation in the injection volume below Prati-32. In section 5 it was shown that the generated fractures in the study area are not homogeneously distributed. It could be seen that the highest concentration of fractures developed in the northern part of the region below and to the north of the injection well

Prati-32, whereas the southern half of our study area exhibited a lower fracture concentration. For reference, refer to Figures 5.6-5.8. Therefore, it was investigated whether the fluid saturation is spatially correlated to fracture density.

The distribution of epicenters associated with 192 events with high accuracy locations recorded during the first three months of injection activities is presented in Figure 7.1a. The analysis of these events led to the post-injection Vp/Vs ratio of 1.67 ± 0.04, as reported in section 2.5 (Figure 2.16). This sequence was subsequently divided into a northern and a southern cluster, which are shown in Figures 7.1b and 7.1c, respectively. The seismicity in the two clusters was analyzed using the DDW technique with L1-L2 norm fitting to determine the Vp/Vs ration and associated fluid saturation.

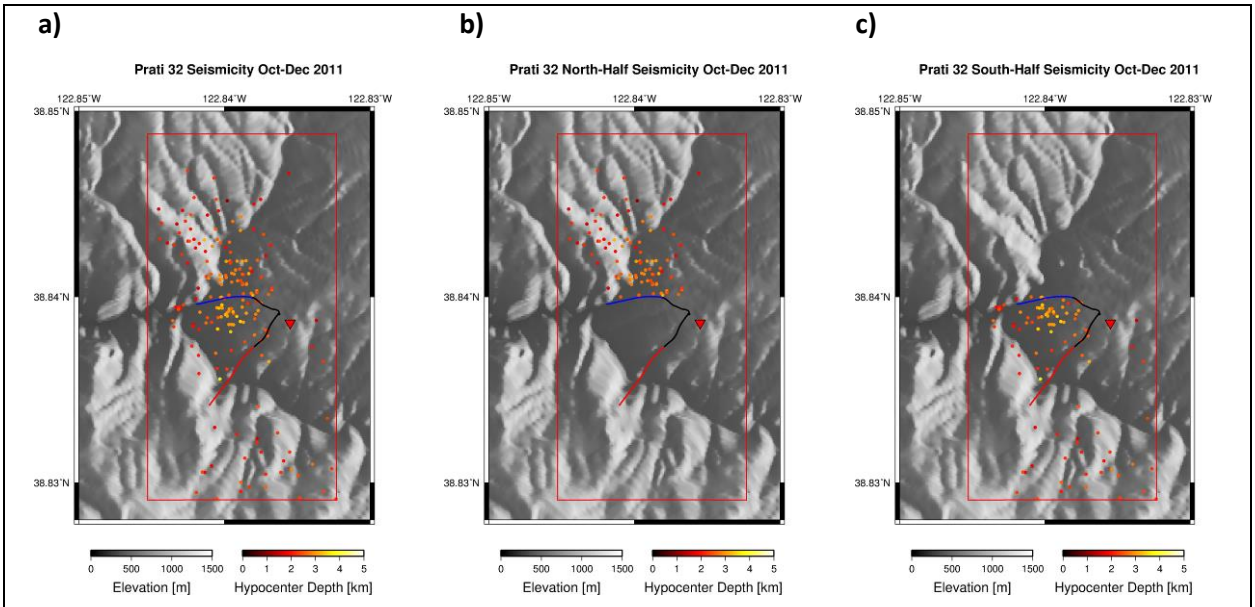

Figure 7.1: a) Map view of 192 earthquake locations recorded in the first three months of injection activities at Prati-32. **b)** Map view of a subset of 92 events located in the northern half of the study area. **c)** Map view of a subset of 100 events located in the southern half of the study area.

The results of our DDW analysis of the travel times associated with events in the northern half of the area are presented in Figure 7.2. The relatively small magnitudes (Mw=0.5-1.6) of these earthquakes resulted in a subset of 15 of the 34-station network to record these events, with a maximum station gap of 128^{o} (see Figure 7.2a). A small station gap assures that the source region of the events is well sampled by the P-and S-wave rays, which is an important prerequisite for the assumptions made during DDW analysis (Lin and Shearer, 2007). Stations gaps of less than 150^{o} are reasonable for DDW analysis. The conditions at The Geysers are well suited for this analysis, because the seismicity is shallow and occurs within the extent of the seismic network. The result of the L1-L2 norm fitting of the differential travel times based on waveform cross correlation is presented in Figure 7.2b. The linear fit yields a slope of 1.59 with

a standard deviation of 0.04. This low Vp/Vs ratio is indicative of a gaseous fluid saturation likely indicating the presence of the previously mentioned steam plume in the highly fractured area to the north of Prati-32. The low Vp/Vs ratio is similar to Vp/Vs = 1.54 ± 0.05, which was presented in section 2.4 (Figures 2.13 and 2.14) and reported by Gritto et al. (2016) for the Fumarole Area of The Geysers, where surface steam vents indicate the presence of gaseous fluids in the subsurface.

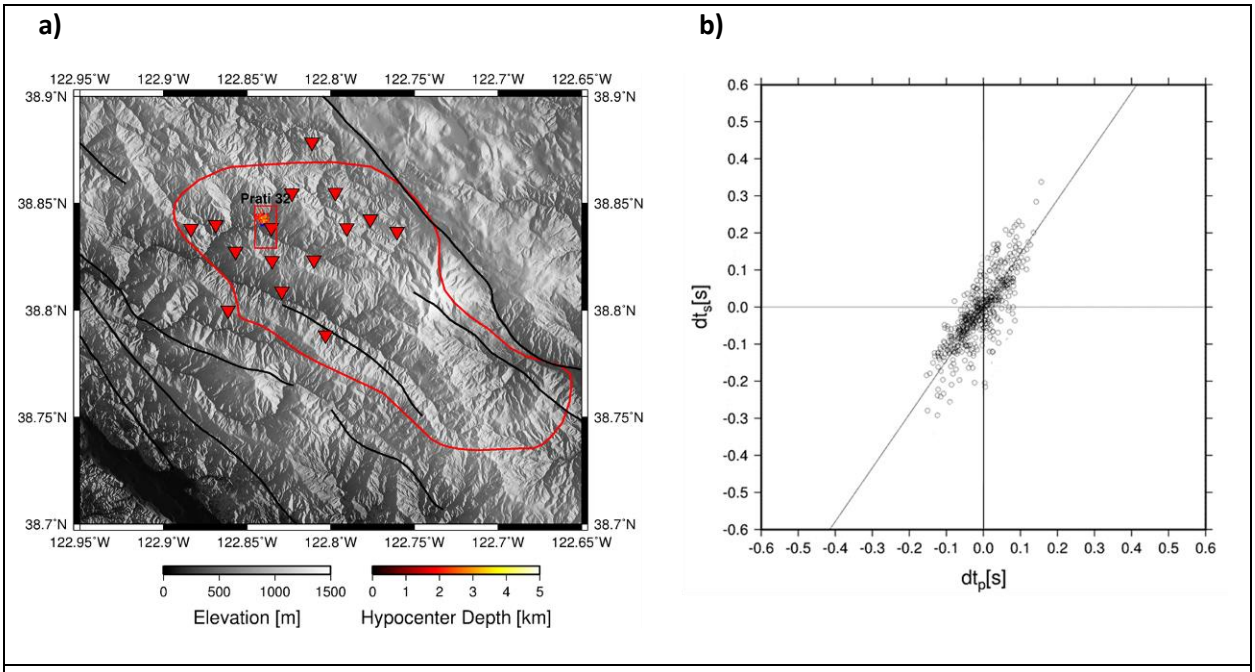

Figure 7.2: WDD analysis of earthquake data in the northern half of the Prati-32 study area (red rectangle). **a)** Map view of the seismic stations that recorded the seismicity in the northern half of the Prati-32 study area. Maximum station gap: 128°. **b)** Wadati diagram with P- and S-wave double difference travel times and linear fit based on the L1-L2 norm. Linear fit: 1.59 ± 0.04.

In contrast, the results for the southern half of the area are presented in Figure 7.3. Like the northern region, the low-magnitude seismicity (Mw 0.3-1.7) was recorded by 15 stations with a gap of 108° (Figure 7.3a). The results of the DDW analysis using L1-L2 norm fitting are presented in Figure 7.3b. The slope yielded a Vp/Vs ratio of 1.78 with a standard deviation of 0.03. This value is statistically insignificant from the pre-injection value (1.76 ± 0.04) for the total study region, which suggests that the area south of Prati-32 may not have experienced an increase in the volume of gaseous fluids. However, it is possible that the southern area contains liquid fluids that flash to steam during production. The Vp/Vs results suggest a steam plume that is concentrated in the northern half of the study area below Prati-32 spatially correlated to the high degree of fracturing.

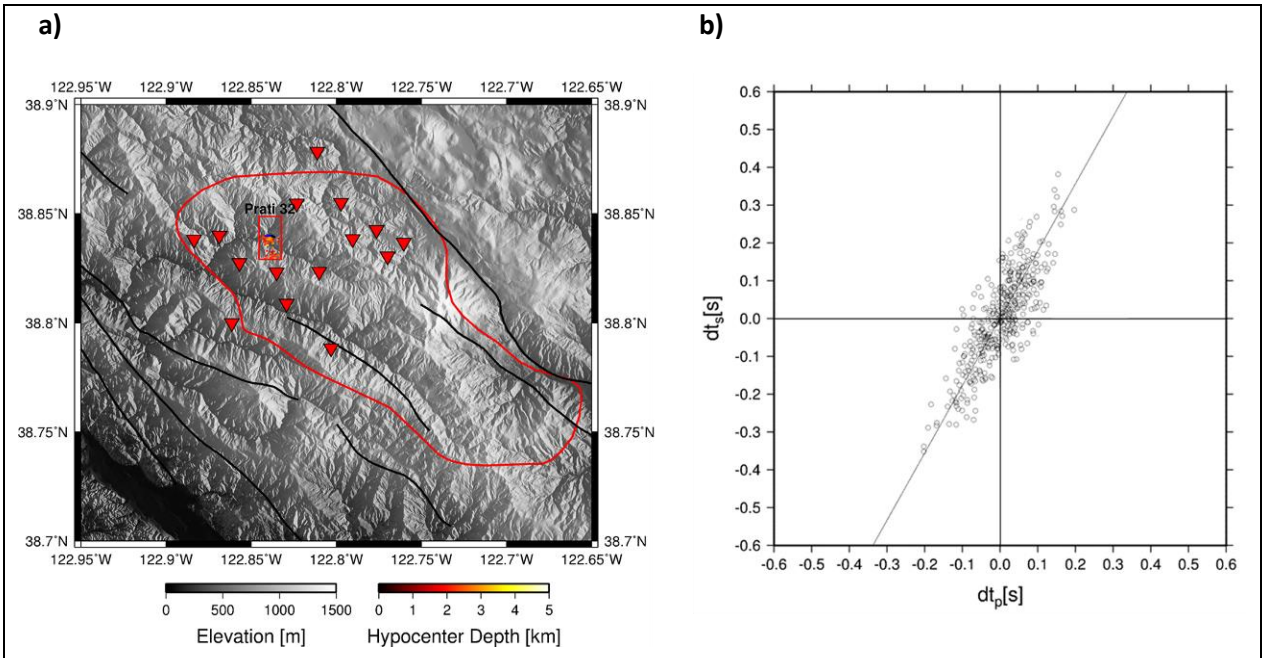

Figure 7.3: WDD analysis of earthquake data in the southern half of the Prati-32 study area (red rectangle). **a)** Map view of the seismic stations that recorded the seismicity in the southern half of the Prati-32 study area. Maximum station gap: 108°. **b)** Wadati diagram with P- and S-wave double difference travel times and linear fit based on the L1-L2 norm. Linear fit: 1.78 ± 0.03.

7.2 Summary

We developed a statistical representation of the 3D fracture network that was generated during the EGS demonstration project at Prati-32. It was found that that the highest concentration of fractures is located approximately 300 m to the north and 400 m below the bottom of the injection and production wells. Given the uneven distribution of fractures in the study area, the double-difference Wadati (DDW) technique was applied to investigate spatial variations in the fluid saturations. Previous results (section 2.5) had indicated that during the first three months of injection a steam plume developed in the study region below Prat-32. In present task it was shown that the steam plume is not symmetrically distributed within the 1x2 km study area but appears to be more concentrated in the northern half of the study area, which spatially agrees with the location of the high fracture concentration. The analyses show that DDW can be applied to EGS systems to estimate spatio-temporal changes in subsurface fluid saturation during all phases of EGS operations to aid in the assessment of the fluid content in the subsurface.

8.0 In-Situ Stress Estimation

8.1 Stress Inversion

The goal of EGS hydraulic stimulations is to artificially induce shear slip and dilatation along pre-existing fractures by injecting fluids at low pressures to enhance formation permeability in hot but impermeable rocks. For these stimulations to be successful, the targeted formations should contain slightly permeable natural fractures that are well oriented and highly stressed for shear failure and have the appropriate mechanical properties for the generation and maintenance of shear-enhanced fracture dilatation (Hickmann and Davatzes, 2010). Therefore, the characterization of fracturing and the orientation of principal stresses and changes in stress orientation are critical factors for the planning and the development of EGS resources and for the operations of EGS systems.

The determination of in-situ stress from earthquake focal mechanisms (Gephart and Forsythe, 1984; Michael, 1984) has been shown to provide stable and robust estimates of the orientation of the principal components of the stress ellipsoid at depth (Michael, 1987), to enable regional characterization of tectonic stress (Hardebeck and Michael, 2006), to document changes in stress state following large earthquakes (Hardebeck and Hauksson, 2001), and to delineate ambient stress in applications of hydraulic fracturing (Baig and Urbancic, 2010).

In the current project, the solutions of the moment tensor catalog (section 3) were used to invert for the in-situ state of stress within the study region utilizing both the MSATSI software developed by Martinez-Garzon et al. (2014), which is based on the method of Hardebeck and Michael (2004, 2006), and the STRESSINVERSE software package developed by Vavrycuk (2014). Because it is not known which of the two possible nodal planes of the moment tensor solution is the actual earthquake rupture plane, a random sampling of the nodal planes is bootstrapped to assess the uncertainty in the estimated stress tensors in the MSATSI approach, while the STRESSINVERSE code uses an iterative method to find the nodal planes most consistent with the stress field given fault frictional properties. In the following we present the results of our inversion with the STRESINVERSE code inverting the strike, rake and dip from our moment tensor catalog for the in-situ state of stress. This is done by applying 15 overlapping time windows containing 30 events for each period of the stress inversion with a 10-event overlap between time windows.

The MT solutions for the time windows (A-O) that were shown in Figure 3.8 are presented in Figure 8.1. The figure contains location maps of focal mechanisms shaded by hypocenter depth. Two-thirds of the focal mechanisms repeat in adjacent maps due to the 20-event overlap in the sliding time windows. Despite the repetition of overlapping events in adjacent maps, spatial-temporal patterns in seismicity are evident. Before injection begins, the eastern portion of the study area appears to be seismically active with shallow strike-slip faulting mechanisms throughout the study area. With elapsing time, the hypocenter locations concentrate in the center of the study area at increasing depth, while the events reveal more normal-faulting mechanisms.

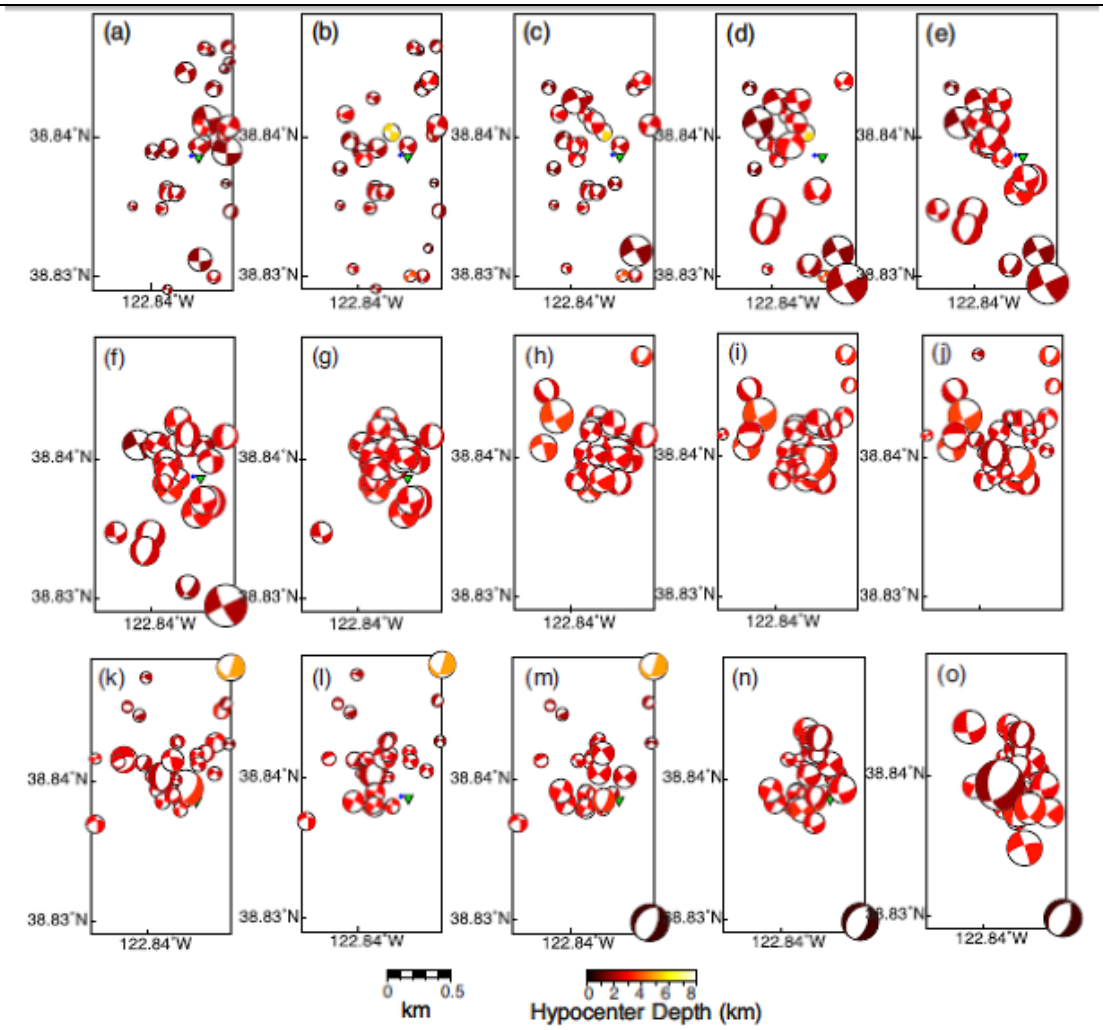

Figure 8.1: Location maps each with 30 focal mechanisms shaded by hypocenter depth during corresponding overlapping time windows A—O. Two-thirds of the focal mechanisms repeat in adjacent maps due to the 20-event overlap of the sliding time windows. From Boyd et al. (2018).

The stress inversion results show an interesting change in the orientation of the principal stress axes during injection operations. The results in Figure 8.2 are presented in form of stereonet plots of the orientation of principal stress axes σ_1 (red), σ_2 (green) and σ_3 (blue) for each time window shown in Figure 8.1 (Boyd et al., 2018). The colored regions show the 95% confidence region from applying 100 random noise realizations assuming a mean source mechanism uncertainty of 5° and rerunning the inversion for each set of perturbed data. Initially, there is an east–southeast orientation of the minimum compressive stress σ_3 and south–southwest maximum compressive stress σ_1 in a predominantly strike-slip faulting environment. Gradually with time during injection there is an approximately 15-degree counter-clockwise rotation of σ_3 until time window J ending 2012 September 20. This is followed, beginning in July 2012, by a marked rotation of σ_1 towards a more vertical orientation (time window K). This time window corresponds to a period when injection operations temporarily cease at Prati-32 for a period of approximately 160 days. Subsequent time windows L and M show a similar rotation in

orientation that corresponds to further changes in injection operations. From February to March 2013, injection shifts to Prati State 31 resulting in a migration of seismicity to the south, until injection resumes in Prati-32 in April 2013 (Garcia et al., 2016). During this period the magnitude of σ_1 and σ_2 begin to equalize (Figure 8.2) indicating that the system is evolving to a more transtensional environment in which the mechanisms are comprised of both strike-slip and normal types (Boyd et al., 2018). STRESSINVERSE (Vavrycuk 2014) iteratively solves for an optimal friction parameter in evaluating the fault instability to find optimal fault planes. Vavrycuk (2014) states that numerical tests show that inversion results are insensitive to the friction parameter, and it is sufficient to assign a reasonable value for all inversions. We elected to allow the friction parameter to change and found it to not substantially change with values of 0.7 ± 0.2, which is consistent with laboratory estimates for graywacke and other rocks at the confining pressures of the studied earthquakes (i.e., Byerlee 1978; Lockner *et al.* 1982).

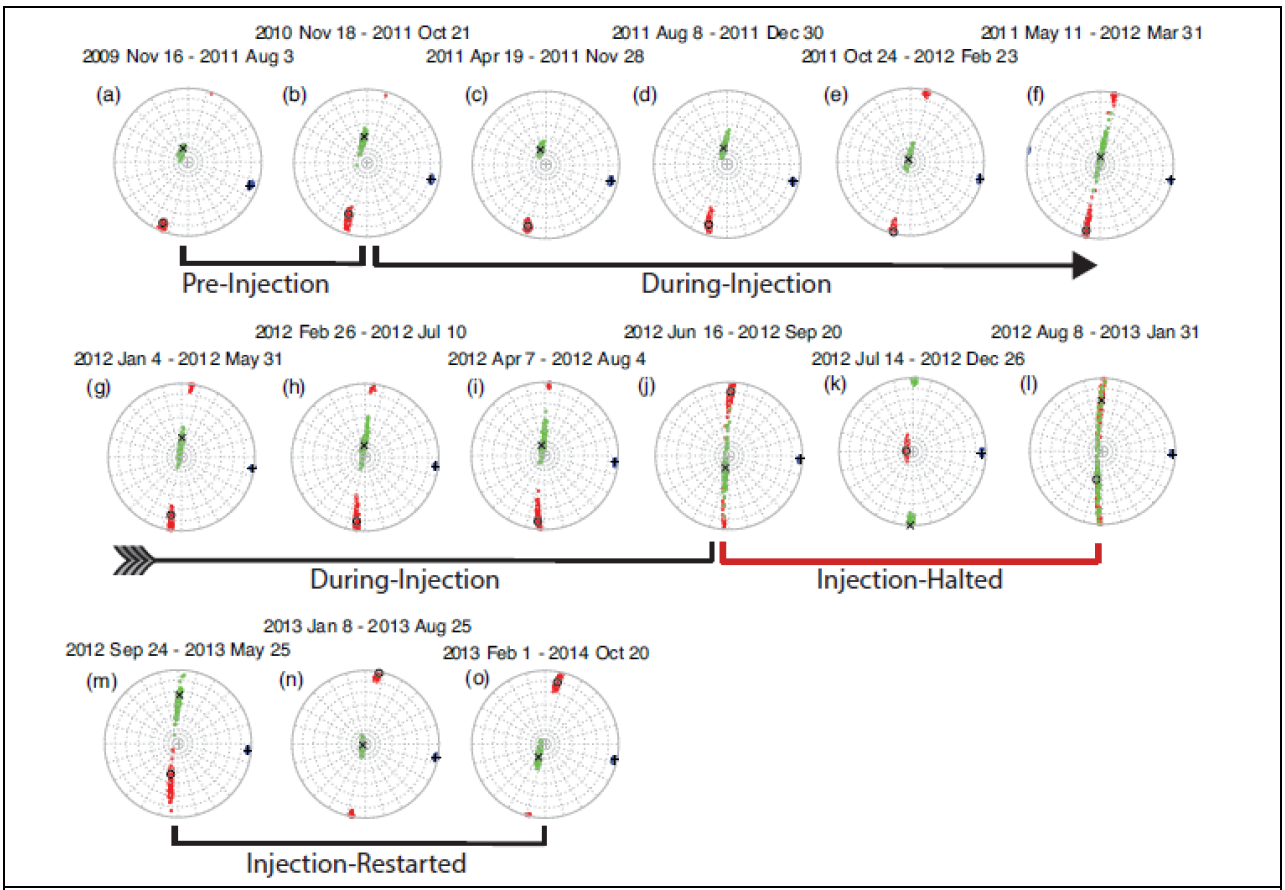

Figure 8.2: Stereonet plots (a)-(o) of principal stress orientations obtained by inverting strike, rake and dip from the moment tensor solutions in Figure 8.1 using STRESSINVERSE (Vavrycuk, 2014). The orientations of the maximum compressive stress σ_1 (red), intermediate stress σ_2 (green) and minimum compressive stress σ_3 (blue) are well constrained. The colored regions show the 95% confidence region from applying 100 random noise realizations assuming a mean mechanism uncertainty of 5°. Within each 95% confidence region the best orientation of the principal stress axis is marked with a circle for σ_1, a cross for σ_2, and a plus symbol for σ_3. From Boyd et al. (2018).

8.2 Stress Shape Factor

Examining the relative magnitude of the stress components, it is seen that as the orientation of the stress tensor is changing so too is the stress shape factor, R (Gephart & Forsyth 1984). R is defined as

$$R = \frac{\sigma_1 - \sigma_2}{\sigma_1 - \sigma_3} \quad (8.1),$$

where σ_1 is the maximum compressive stress and σ_3 is the least compressive stress. As can be seen in Figure 8.3, R decreases systematically as injection rate and total volume of injected water increases. The reduction in R is due to both a decrease in the relative magnitude of σ_3 and an increase in the relative magnitude of σ_2 indicating that the stress is evolving to a more transtensional environment, which can also be seen directly from examination of the focal mechanisms (Figure 8.1). We find in fitting a line to the R data that the negative slope is statistically significant considering the 95% confidence in the estimate of the slope up to time window J (R^2 = 0.5 and p-value = 0.02). At later times the large oscillations still lead to a negative slope, but the uncertainty indicates that it cannot be considered statistically significant at the 95% confidence level (Boyd et al., 2018).

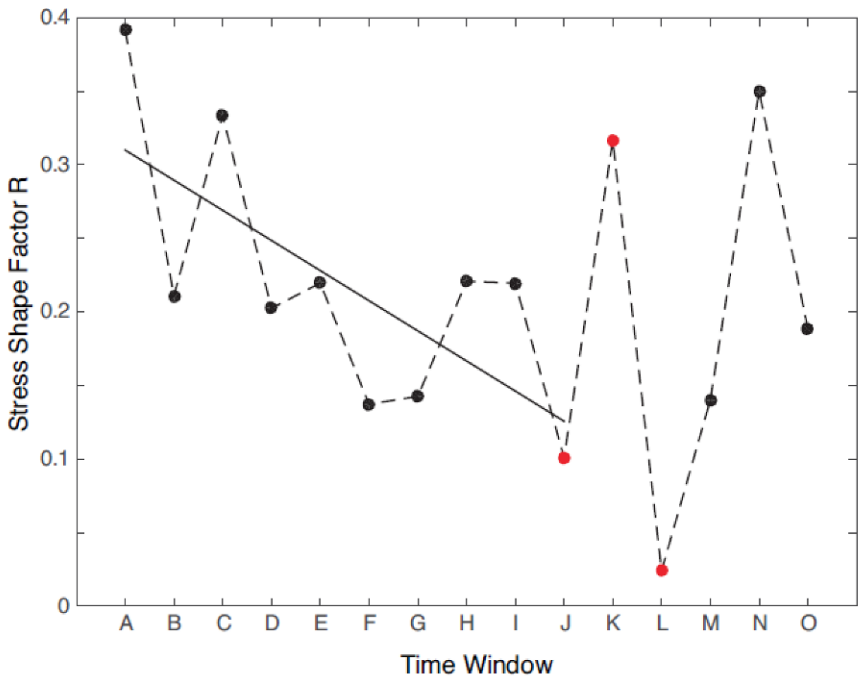

Figure 8.3: Plot of stress shape factor R for each moving time window. The solid line fitted to the R data has a negative slope that is statistically significant considering the 95% confidence in the estimate of the slope up to time window J (R^2 = 0.5 and p-value = 0.02). Data points shaded red occur during windows J, K and L that sample periods of time when injection halted. From Boyd et al. (2018).

The Geysers and Clear Lake area are in a transtensional tectonic regime (Oppenheimer, 1986; Donnelly-Nolan et al., 1993; Allis and Shook 1999; Boyle and Zoback, 2014). The regional stress field based on the World Stress Map database release 2008 (Heidbach et al., 2010) shows a mean orientation of the maximum horizontal stress SHmax of 33° ± 28° based on 20 data records. Within The Geysers the mean SHmax orientation is 27° ± 20° based on 37 earthquake focal mechanism solutions from the period 1992 to 2011 (Gritto et al., 2014). This observation is consistent with results of Boyle and Zoback (2014). From their stress inversion of more than 6,100 well-constrained earthquake focal mechanism solutions of events with M > 1.5 from 2005 to 2012, they obtained a mean SHmax orientation of 26°. SHmax inferred from our analysis for the localized study area indicates that it trends 10–15°. It is noted that the northwest Geysers represents an area with complex fault-bounded regions (i.e., Figure 1.1) in which each could have slightly different stress orientation. The results of our stress analyses indicate a 15° counter-clockwise rotation of σ_3 during the study period. During the period of time when injection temporarily ceased (windows K, L and M; Figure 8.2) there is a marked rotation of σ_1 towards a more vertical orientation, which subsequently recovers when injection operations recommenced. This demonstrates that fluid injection operations have a substantial impact on the state of stress and the fractures that become activated. The magnitude of the stress rotations we observed is consistent with other nearby empirical observations (Martinez-Garzon et al., 2013) and thermo-hydromechanical simulation results (Jeanne et al., 2015; Ziegler et al., 2017).

Studies by Kwiatek et al. (2015) for injection in the northwest Geysers show a long-term temporal decrease in the shape factor R in an observed normal stress regime, assuming $\sigma_V = \sigma_1$ is constant. As pore pressure increases over time, a reduction in all effective stresses and an increase in horizontal stresses is assumed due to poroelastic effects (Schoenball et al., 2010; Altmann et al. 2014) such that the increase in σ_2 leads to decrease in R. As presented in Figure 8.3, we find that there is a systematic reduction in the stress shape factor, R, as injected volume increases, indicating an evolution towards a more transtensional stress state, however after the cessation and resumption of injection the estimated shape factor becomes oscillatory indicating a significant change in the response of the system due to the interruption and restart of the injection operations. Such a reduction in R with increasing injection and pore pressure has been observed NE of the study area (Kwiatek et al., 2015; Martinez-Garzon et al., 2016), while Kwiatek et al. (2015) also note that the reduction of R slows as injection is ceased.

9.0 References

Allis, R. and Shook, G.M., 1999, An alternative mechanism for the formation of The Geysers vapor-dominated reservoir, *Proceedings of the 24th Workshop on Geothermal Reservoir Engineering*, Stanford, SGP-TR-162.

Baig, A., and T. Urbancic, 2010, Microseismic moment tensors: A path to understanding frac growth, *The Leading Edge*, 29 320-324.

Bowers, D., and J. A. Hudson, 1999, Defining the scalar moment of a seismic source with a general moment tensor, *Bull. Seism. Soc. Am.*, 89 1390-1394.

Boyd, O. S., D. S. Dreger, V. H. Lai, and R. Gritto, 2015, A Systematic Analysis of Seismic Moment Tensor at The Geysers Geothermal Field, California, *Bull. Seism. Soc. Am.*, 105, No. 6, doi:10.1785/0120140285.

Boyle, K. and M. Zoback, 2014, The Stress State of the Northwest Geysers, California Geothermal Field, and Implications for Fault-Controlled Fluid Flow, *Bull. Seis. Soc. Am.*, 104, doi: 10.1785/0120130284.

Byerlee, J.D., 1978. Friction of rock, *Pure appl. Geophys.*, 116, 615–626.

California geologic map data. *http://mrdata.usgs.gov/geology/state/state.php?state=CA*.

Donnelly-Nolan, J.M., M.G. Burns, F.E. Goff, E.K. Peters and J.M. Thompson, 1993, The Geysers-Clear Lake area, California; thermal waters, mineralization, volcanism, and geothermal potential, *Economic Geology*, 88, 301-316.

Dreger, D.S., 1997, The Large Aftershocks of the Northridge Earthquake and their Relationship to Mainshock Slip and Fault Zone Complexity, *Bull. Seism. Soc. Am.*, 87, 1259-1266.

Dreger, D.S., R. Nadeau and A. Chung, 2007, Repeating Earthquake Finite-Source Models: Strong Asperities Revealed on the San Andreas Fault, *Geophys. Res. Lett*., 34, L23302, doi:10.1029/2007GL031353.

Dreger, D.S., O.S. Boyd, R. Gritto, 2017, Estimating In-Situ Stress, Fracture Properties and Fluid Saturation During The Geysers EGS Demonstration Project, *Geothermal Resources Council Transactions*, Vol. 41, 2017, pp. 1-16.

Ford, S., D. Dreger, and W. Walter, 2008, Source Characterization of the August 6, 2007 Crandall Canyon Mine Seismic Event in Central Utah, *Seismol. Res. Lett*., 79, 637-644.

Ford, S. R., D. S. Dreger, and W. R. Walter, 2009, Identifying isotropic events using a regional moment tensor inversion, *J. Geophys. Res*, 114, no. B01306, doi:10.1029/2008JB005743.

Ford, S. R., D. S. Dreger, and W. R. Walter, 2010, Network sensitivity solutions for regional moment tensor inversions, *Bull. Seism. Soc. Am.*, 100, 1962-1970.

Ford, S. R., W. R. Walter, and D. S. Dreger, 2012, Event discrimination using regional moment tensors with teleseismic-P constraints, *Bull. Seism. Soc. Am.*, 102, 867-872.

Garcia, J., Hartline, C., Walters, M., Wright, M., Rutqvist, J., Dobson, P.F. and Jeanne, P., 2016, The northwest geysers EGS demonstration project, California Part 1: characterization and reservoir response to injection, *Geothermics*, 63, 97–119.

Gritto, R.; Daley, T. M.; Myer, L. R., (2004a), "Joint Cross Well and Single Well Seismic Studies of CO2 Injection in an Oil Reservoir.", Geophysical Prospecting, 52, pp. 323-339.

Gritto, R.; Romero, A. E., Daley, T. M., (2004b), "Results of a VSP Experiment at the Resurgent Dome, Long Valley Caldera, California." Geophys. Res. Lett., 31, No. 6, L06603, (2004b), 10.1029/2004GL019451.

Gritto, R., S.H. Yoo, S.P. Jarpe, 2013, Three-Dimensional Reservoir Structure of The Geysers Geothermal Reservoir Derived from Seismic Tomographic Vp/Vs Imaging, *GEISER Final Conference*, Naples, May 29 – June 1, 2013.

Gritto, R. and S.P. Jarpe, 2014, Temporal variations of Vp/Vs-ratio at The Geysers geothermal field, USA, *Geothermics*, http://dx.doi.org/10.1016/j.geothermics.2014.01.012.

Gritto, R., D.S. Dreger, O.S. Boyd, and T. Taira, 2016, Fluid Imaging, Moment Tensors and Finite Source Models During the EGS Demonstration Project at The Geysers, CA, *41st Workshop on Geothermal Reservoir Engineering*, February 22-24, 2016, Stanford University, Stanford, CA,

Guilhem, A., L. Hutchings, D. S. Dreger, and L. R. Johnson, 2014, Moment tensor inversions of M~ 3 earthquakes in the Geysers geothermal fields, California, *J. Geophys. Res.*, 119, doi:10.1002/2013JB010271.

Heidbach, O., M. Tingay, A. Barth, J. Reinecker, D. Kurfeß and B. Müller, 2010, Global crustal stress pattern based on the World Stress Map database release 2008, *Tectonophys*., 482, 3-15, doi:10.1016/j.tecto.2009.07.023.

Hickman, S. and N. Davatzes, 2010, In-situ stress and fracture characterization for planning of an EGS stimulation in the Desert Peak geothermal field, Nevada, *Proceedings*, *Thirty-Fifth Workshop on Geothermal Reservoir Engineering*, Stanford University, Stanford, California, February 1-3, 2010, SGP-TR-188

Hudson, J. A., R. G. Pearce, and R. M. Rogers, 1989, Source type plot for inversion of the moment tensor, *J. Geophys. Res*., 94, 765-774.

Johnson, L. R., 2014a, Source Mechanisms of Induced Earthquakes at The Geysers Geothermal Reservoir, *Pure Appl. Geophys*., doi 10.1007/s00024-014-0795-x.

Johnson, L. R., 2014b, A Source Model for Induced Earthquakes at The Geysers Geothermal Reservoir, *Pure Appl. Geophys*., doi 10.1007/s00024-014-0798-7.

Kwiatek, G., P. Martinez-Garzon, G. Dresen, M. Bohnhoff, H. Sone, and C. Hartline, C., 2015, Effects of long-term fluid injection on induced seismicity parameters and maximum magnitude in northwestern part of The Geysers geothermal field, *J. Geophys. Res.*, 120, 7085–7101.

Julian B.R., A. Ross, G.R. Foulger, and J.R. Evans, 1996, Three-dimensional seismic image of a geothermal reservoir: The Geysers, California, *Geophys. Res. Lett.*, 23, doi:10.1029/96GL03321.

Leonard, M., 2010, Earthquake Fault Scaling: Self-Consistent Relating of Rupture Length, Width, Average, Displacement, and Moment Release, *Bull. Seism. Soc. Am*., doi: 10.1785/0120090189, 1971-1988.

Leptokaropoulos, K., Staszek, M., Lasocki, S., Martiınez-Garzon, P. and Kwiatek, G., 2018, Evolution of seismicity in relation to fluid injection in the North-Western part of The Geysers geothermal field, *Geophys. J. Int*., 212, 1157–1166.

Lockner, D., R. Summers, D. Moore and J. Byerlee, 1982, Laboratory measurements of reservoir rock from the Geysers geothermal field, California, *International Journal of Rock Mechanics and Mining Sciences & Geomechanics Abstr*acts, 19, 65-80.

Lutz, S.J., Walters, M., Pistone, S. & Moore, J.N., 2012, New insights into the high-temperature reservoir, Northwest Geysers, *Trans. Geoth. Resour. Counc.*, 36, 907–916.

Majer, E. and J.E. Peterson, 2007, The impact of injection on seismicity at The Geysers, California geothermal field, *Int. J. Rock Mech. Min. Sci*. 44, doi: 10.1016/j.ijrmms.2007-07.023, 1079-1090.

Martinez-Garzon, P., M. Bonhoff, G. Kwiatek, and G. Dresen, 2013, Stress tensor changes related to fluid injection at The Geysers geothermal field, California, *Geophys. Res. Lett*., 40, 2596-2601, doi:10.1002/grl.50438.

Martinez-Garzon, P., Kwiatek, G., Ickrath, M., and Bohnhoff, M., 2014, "MSATSI: A MATLAB Package for Stress Inversion Combining Solid Classic Methodology, A New Simplified User-Handling, and a Visualization Tool." *Seism. Res. Lett.*, 85(4), 896-904, doi: 10.1785/0220130189.

Martinez-Garzon, P., V. Vavrycuk, G. Kwiatek, and M. Bohnhoff, 2016, Sensitivity of stress inversion of focal mechanisms to pore pressure changes, *Geophys. Res. Lett.*, 43, 8441–8450.

Minson, S., D. Dreger, R. Burgmann, H. Kanamori, and K. Larsen, 2007, Seismically and Geodetically Determined Non-Double-Couple Source Mechanisms From the 2000 Miyakejima Volcanic Earthquake Swarm, *J. Geophys. Res*., 112, B10308, doi:10.1029/2006JB004847.

Minson, S., and D. Dreger, 2008, Stable Inversions for Complete Moment Tensors, *Geophys. J. Int*., 174, 585-592.

Moos D. and M. Zoback, 1983, In-situ Studies of Velocity in Fractured Crystalline Rocks, *J. Geophys. Res.*, 88, B3, doi:10.1029/JB088iB03p02345.

Mori, J. J., 1993, Fault plane determinations for three small earthquakes along the San Jacinto Fault, California: search for cross faults, *J. Geophys. Res*., 98, 17711-17722.

Mori, J. and S. Hartzell, 1990, Source inversion of the 1988 Upland earthquake: determination of a fault plane for a small event, *Bull. Seism. Soc. Am*., 80, 507-518.

Nayak, A., and D. S. Dreger, 2014, Moment Tensor Inversion of Seismic Events Associated with the Sinkhole at Napoleonville Salt Done, Louisiana, *Bull. Seism. Soc. Am*., 104, 1763-1776, doi: 10.1785/0120130260.

Nayak, A., and D. S. Dreger, 2015, Source-Type-Specific Inversion of Moment Tensors, *Bull. Seism. Soc. Am*., 105(6):2987-3000, doi: 10.1785/0120140334

Nielson, D., Walters, M. & Hulen, J., 1991, Fracturing in the Northwest Geysers, Sonoma County, California, *Trans. Geoth. Resour. Counc*., 15, 27–33.

O'Connell D.R.H. and L.R. Johnson, 1991, Progressive inversion for hypocenters d P wave and S wave velocity structure: applications to The Geysers, California, geothermal field, *J. Geophys. Res.*, 96, 6223-6236.

Oppenheimer D.H., 1986, Extensional tectonics at The Geysers geothermal area, California, *J. Geophys. Res.*, 91, B11, 11463-11476.

Ross, A., G. R. Foulger, and B. R. Julian, 1996, Non-double-couple earthquake mechanisms at The Geysers geothermal area, California, *Geophys. Res. Lett*., 23, 877-880.

Ross, A., G. R. Foulger, and B. R. Julian, 1999, Source processes of industrially-induced earthquakes at The Geysers geothermal area, California, *Geophysics*, 64, 1877-1889.

Saikia, C.K., 1994, Modified Frequency-Wavenumber Algorithm for Regional Seismograms using Filon's Quadrature: Modeling of Lg Waves in Eastern North America. *Geophys. J. Int.*, 118, 142-158.

Schoenball, M., Mueller, T.M., Mueller, B.I.R. and Heidbach, O., 2010. Fluid induced microseismicity in pre-stressed rock masses, *Geophys. J. Int.*, 180, 813–819.

Vavrycuk, V., 2014. Iterative joint inversion for stress and fault orientations from focal mechanisms, *Geophys. J. Int.*, 199, 69–77.

Wang, C. Y. and R. B. Hermann, 1980, A comparison of synthetic Seismograms. *Bull. Seism. Soc. Am.*, 75, p. 41-56.

Wells, D.L. and K.J. Coppersmith, 1994, New empirical relationship among magnitude, rupture length, rupture width, rupture area, and surface displacement, *Bull. Seism. Soc. Am.*, 84, 974-1002.

Wessel, P., and W. H. F. Smith, 1998, New, improved version of Generic Mapping Tools released, *EOS Trans. AGU*, 79, 579.